ELECTRICAL SURFACE MODIFICATION AND CHARACTERIZATION OF METALLIC THIN FILMS USING SCANNING PROBE MICROSCOPE (SPM) NANOLITHOGRAPHY METHOD

A Thesis submitted to
The Graduate School of Engineering and Science of
İzmir Institute of Technology
in Partial Fulfillment of the Requirements for the Degree of

MASTER OF SCIENCE

in Physics

by

Serkan BÜYÜKKÖSE

June 2009
İZMİR

We approve the thesis of **Serkan BÜYÜKKÖSE**

_____

Assoc. Prof. Salih OKUR
Supervisor

_____

Assist. Prof. Süleyman TARI
Committee Member

_____

Assoc. Prof. Metin TANOĞLU
Committee Member

15 June 2009

_____

Prof. Dr. Durmuş Ali DEMİR
Head of the Physics Department

_____

Prof. Hasan BÖKE
Dean of the Graduate School of
Engineering and Sciences

ACKNOWLEDGEMENTS

Firstly, I would like to thank my supervisor, Dr. Salih Okur. His encouragement and support made this project possible. I also would like to thank Dr. Süleyman Tarı and Dr. Gülnur Aygün for their contribution to this thesis. All my friends made department of physics a wonderful working environment. Moreover, my special thanks go to H. Yusuf Günel, Barış Pekerten and Derya Ataç because of their friendship and support whenever I need. Of course, Barış deserves a special recognition because he always endured our endless questions with his deep knowledge of science and behaved us like a brother.

Erdoğan Özdemir is another person I would like to thank. He is one of my best friends with whom we shared bitter sweet days together since undergrad education, and Izmir was more enjoyable with him.

Last but not least, I want to thank to my family; my father, Mehmet Ali Büyükköse, my brother, Ali Osman Büyükköse, and my late mother, Ayten Büyükköse. I feel very lucky to have such a nice family. Although she is not aware of those yet, I also thank my little and sweet niece Ayten for the things she made me feel.

ABSTRACT

ELECTRICAL SURFACE MODIFICATION AND CHARACTERIZATION OF METALLIC THIN FILMS USING SCANNING PROBE MICROSCOPE (SPM) NANOLITHOGRAPHY METHOD

This thesis focuses on local oxidation of metallic thin films using atomic force microscopy (AFM). The primary aim of this thesis is to investigate the growth kinetics of oxide forms of these metallic materials and characterize the resulted oxide structures. In this study, tantalum, hafnium and zirconium thin films were used to be oxidized via AFM. During this work, metallic thin films were grown on Si and SiO_x substrates with DC magnetron sputtering method. Thin films were characterized via x-ray diffraction, scanning electron microscopy and atomic force microscopy. Oxidation experiments were performed under different environmental conditions to explore the effect of influential parameters; such as bias voltage, oxidation time and relative humidity, and line shape oxide structures were created on metallic films. Dimensional analysis of created oxide structures was carried out measuring height and line-width of oxide lines as a function of applied voltage, oxidation time and relative humidity. In addition to the dimensional analysis, electrical characterization of metal-oxides was performed via AFM electrical characterization methods which are two terminal I-V measurements, electric force microscopy and spreading resistance measurements. At the end of the thesis, the capability of this method to create lateral metal-oxide-metal junction was shown oxidizing a tantalum stripe and performing in-situ resistance measurement. Patterning of tantalum stripes was accomplished by standard photolithography process and lift-off technique.

ÖZET

TARAMALI UÇ MİKROSKOBU NANOLİTOGRAFİ YÖNTEMİYLE METALİK İNCE FİLMLERİN ELEKTRİKSEL YÜZEY ŞEKİLLENDİRMESİ VE KARAKTERİZASYONU

Bu tez, metalik ince filmlerin atomik kuvvet mikroskobu (AKM) yöntemi ile bölgesel olarak oksitlenmesi üzerine odaklanmıştır. Tezde, AKM ile oksitlenmek üzere tantalum, hafniyum ve zirkonyum ince filmleri kullanılmıştır. Tezin ana amacı bu metalik malzemelerin oksit formlarının büyüme kinetiklerinin araştırılması ve oluşan oksit yapıların karakterize edilmesidir. Çalışma sırasında ince filmler Si ve SiO_x alt taşlar üzerine DC mıknatıssal sıçratma yöntemi ile büyütülmüştür. Bu ince filmler x-ışını kırınımı metodu, taramalı elektron mikroskobu ve atomik kuvvet mikroskobu kullanılarak karakterize edilmiştir. Oksitleme deneyleri uygulanan voltaj, oksitleme zamanı ve bağıl nem gibi değişkenlerin etkilerini araştırabilmek için farklı çevresel şartlar altında gerçekleştirilmiş ve metalik yüzeyler üzerine çizgi şekline sahip nanometre boyutunda oksit yapılar oluşturulmuştur. Oluşturulan oksit yapıların yükseklik ve çizgi genişlikleri farklı oksitleme voltajı, oksitleme zamanı ve bağıl nem değerlerinde ölçülerek boyutsal analizleri yapılmıştır. Boyutsal analize ek olarak, metal-oksitlerin elektriksel özelliklerinin incelenmesi, AKM elektriksel karakterizasyon yöntemlerinden olan iki terminal I-V ölçümü, elektrik kuvvet mikroskopisi ve direnç dağılımı ölçümleri aracılığı ile gerçekleştirilmiştir. Tezin son aşamasında, tantalum şeritlerin eşzamanlı direnç ölçümü yapılarak oksitlenmesi ve bu yöntemin yanal metal-oksit-metal eklemler oluşturabilme yeteneği gösterilmeye çalışılmıştır. Tantalum şeritlerin oluşturulması ise standart fotolitografi işlemi ve kaldırma yöntemleri ile yapılmıştır.

To my Family

TABLE OF CONTENTS

LIST OF FIGURES

LIST OF TABLES

CHAPTER 1

INTRODUCTION

Today's microelectronics is based on silicon technology; and microelectronic and mechanic devices continue to shrink in size. On the other hand, this miniaturization requires new metrology and fabrication tools. While the dimensions are decreased traditional lithography methods, which use ultraviolet light, suffer from limitation of the wavelength of light. To find a solution to this problem some other techniques, such as, electron beam lithography (EBL), x-ray lithography (XRL) and scanning probe lithography (SPL) have been employed. Among them SPL is one the potential applicable technique to create devices in sub 100 nm scale. SPL technique includes both scanning tunneling microscopy (STM) and atomic force microscopy (AFM). SPL has advantages such as, high resolution, alignment accuracy, high reliability, absence of radiation damage and low cost.

Among the SPL techniques, the tip-induced anodic surface oxidation is one of the most studied methods. In this method, AFM or STM tip is negatively biased to locally oxidize a semiconductor or metal surface. AFM is more proper than STM for this operation to prevent further oxidation of surface. The resulting oxide dimension depends on tip bias, oxidation time and relative humidity. Although height of the oxide has been proposed as a function of time in different forms; such as inverse-log, direct-log or power law, there is no model completely explaining this phenomenon. Moreover, there is not any model attempting to explain line-width as a function of effective parameters. Up to now, to improve the performance of this lithography technique, a lot of research groups have performed experiments. Perez-Murano and Legrand have applied voltage pulses instead of continuous voltage by reducing the space charge accumulation in the oxide during oxidization (Perez-Murano, et al. 1999, Legrand, et al. 1999). Fontaine has showed that pulsed tapping mode operation yields more desirable results in comparison with STM and contact mode AFM (Fontaine, et al. 1998). Also,

minimizing the water bridge between tip and sample surface noncontact mode AFM has been used to obtain high aspect ratio oxide nanostructures (Tello, et al. 2001, Calleja, et al. 2000, Garcia, et al. 1999). As a new approach, the attachment of nanotubes to the conductive AFM tip has been used to obtain 10nm resolution by Dai (Dai, et al. 1998). Anodic oxidation has been also applied to create oxide regions on several materials such as, amorphous silicon (Minne, et al. 1995, Kramer, et al. 1995), metals (Sugimura, et al. 1994, Cooper, et al. 1999, Held, et al. 1997, Snow, et al. 1995, Snow, et al. 1996, Abadal, et al. 1999, Song, et al. 1994), silicon nitride (Chien, et al. 2000), GaAs (Dagata, et al. 1991, Okada, et al. 1998) and carbon (Avramescu, et al. 2000) Sugimura first used anodization with STM to oxidize a Ti film (Sugimura, et al. 1994). Snow applied this technique to produce lateral metal-oxide-metal junctions by measuring the film resistance in real time (Snow, et al. 1995).

There are some successful applications of nanoelectronic devices fabricated using SPL technique in the literature, such as field effect transistors (FET's), Josephson junctions and superconducting interference devices (SQUID's), and single electron devices. Minnie et al. produced a metal oxide semiconductor field effect transistor (MOSFET) on Si with an effective channel length of 100nm (Minne, et al. 1995). They defined the gate by AFM oxidation of an amorphous Si. Similarly, Campbell et al. fabricated a side-gated Si field effect transistor (FET) with critical features as small as 30nm (Campbell, et al. 1998, Campbell, et al. 1995). Matsumoto et al. also used STM oxidation of Ti to fabricate single electron transistor (SET) which is a device based on coulomb blockade effect (Matsumoto, et al. 1996). Then, they applied the same method to fabricate Ti tunnel junction and fabricate 5nm wide Ti oxide line enable to observe coulomb oscillations at room temperature using nanotube attached AFM tip (Gotoh, et al. 2000). Bouchiat et al. produced micro bridge junctions and SQUID loops by partial or total oxidation of the niobium layer under the voltage-biased tip of an atomic force microscope (Bouchiat, et al. 2001).

These attempts of miniaturization bring a new problem together. This problem is directly related with the quantum mechanical tunneling. Silicon dioxide has limitations in term of electrical properties because of the actual physical scaling of microelectronic devices. According to quantum mechanics, when the thickness of material, which has a high energy barrier, sufficiently low, there is a still probability for particles to transfer to the other side of the barrier. The leakage current due to direct

tunneling degrades the circuit performance significantly, especially as the thickness of the silicon oxide layer becomes less than 3nm (Suh 2003). This phenomenon does not allow SiO_2 to be used as an electrical barrier in further miniaturization applications. However, there are some candidate materials with high dielectric constant to be replaced with SiO_2, such as Ta_2O_5, HfO_2, ZrO_2, Y_2O_3, TiO_2, etc. (Sayan, et al. 2002, Manchanda, et al. 2001). Among these materials, TiO_2 is the most studied material to be created via SPM oxidation-lithography. In the literature, there are a lot of detailed studies on Ti thin films modified via AFM and STM (Vullers, et al. 1999, Huh and Park 2000, Lemeshko, et al. 2001; Unal, et al. 2002, Fang, et al. 2008). On the other hand the studies on Ta, Hf and Zr are not studied in details (Kim, et al. 2003, Farkas, et al. 2004, Fang and Chang 2004, S. Lee and H. Lee 2006). In our study, Ta, Hf and Zr metals have been chosen to oxidize via SPM oxidation-lithography technique. Our aim is to investigate the growth kinetics of oxide formation on these metallic materials using tip induced electrochemical process and to characterize the resulted oxide structures. It should be noted that reaching to the lithography limits is not the primary goal of this study.

1.1. Lithography

Lithography is a technique used for transfer of pattern on to surfaces. This technique was invented in 1978. Originally, the name of lithography comes from Greek words (litho (stone) + graphein (to write)). In these days, lithography describes various pattern transfer processes used in microelectronics to fabricate integrated circuits (ICs) on a silicon wafer. There are several lithography methods. The dimension of fabricated features varies depending on fabrication method employed. The process can be called as nanolithography when one of the dimensions of transferred pattern is less than the 100nm.

1.1.1. Overview of lithography techniques

In this chapter, some standard lithography techniques and Scanning Probe Lithography (SPL) techniques will be mentioned with their limitations before local oxidation with AFM which will be presented in chapter 2.

1.1.1.1 Optical Lithography

Nowadays, the optical method, called as photolithography, is one of the most used method in microelectronic device fabrication. Steps in the lithography process can be listed as: resist coating, soft bake, alignment and exposure, development, hard bake.

In lithography process the pattern to be transferred is created on a film of specialized materials called as resist (also called as photoresist). Resist is a photo sensitive material. Spincoating method is used to obtain a thin photoresist film on a substrate. It is firstly dispensed on a wafer and wafer is rotated about its axis at a high rate by a spin coater. By this way quality of thickness and uniformity of photoresist are achieved. Typical thickness of photoresist is 0.1-2μm.

After the spin coating, soft baking is applied as a second step in order to improve photoresist-sample surface adhesion. Soft baking step promotes resist uniformity and drives off most of solvent in photoresist.

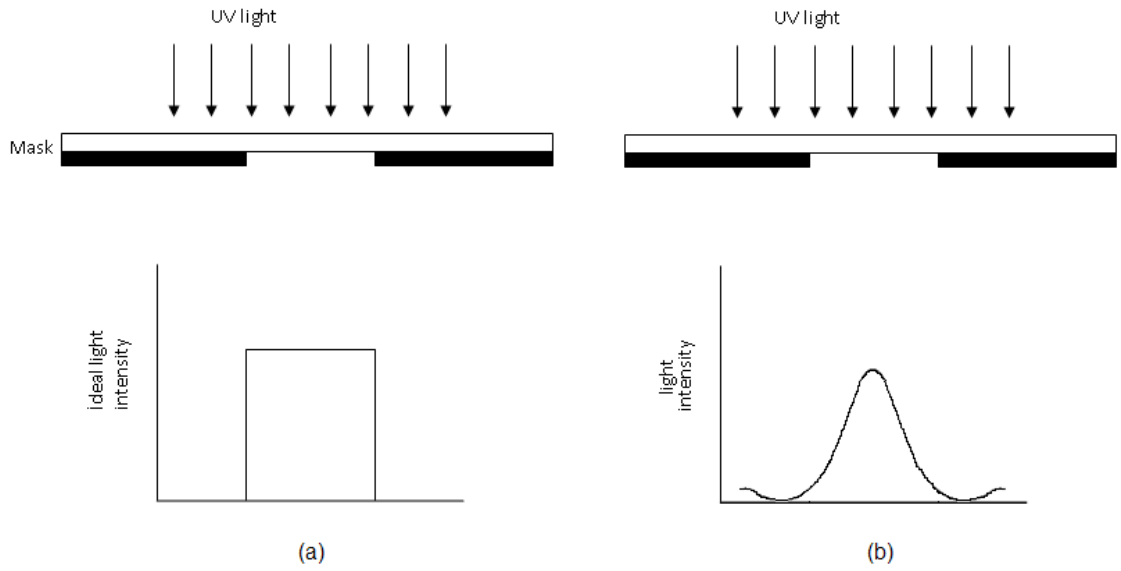

Figure 1.1. (a) Ideal light intensity distribution and (b) degradation from ideal case.

Fabrication of integrated circuits requires a series of patterning step. Therefore, alignment of a mask on another patterned substrate is critical, and is performed by using special equipment, called as “mask aligner”. After the alignment, exposure of photoresist is performed. To illuminate the intended region, a mask is used. The light can pass through only certain open regions on the mask, while it cannot pass through the patterned regions as seen in Figure 1.

To remove photoresist from desired regions photoresist development is performed. In this step, during dipping the sample into a special solvent, called as developer, and rinsing it, the photoresist in the exposed areas is removed because the exposed resist softens and it becomes soluable in aqueous developer. End of the step, visible patterns appeared on sample surface and sample was inspected to verify the quality of pattern by using optical microscope.

Hardbaking is the final step in the photolithographic process and it is an optional step. The temperature required for this step is usually so high. This step makes harden the photoresist and improve adhesion of the photoresist to the wafer surface.

One of the basic problems of optical lithography is light intensity distribution. Figure 1.1.a shows an ideal light intensity. For a given set of optics, intensity profile degrades from ideal case (Figure 1.1.b). This degradation prevents to obtain well

defined edge profile. According to Rayleigh criterion (Levinson 2005) the minimum resolved distance is limited by diffraction effect, which is inherent to the wave nature of light. And it is given as;

$$\delta = 0.61\frac{\lambda}{n\sin\theta} \tag{1.1}$$

where n is the index of refraction of the lens medium, λ is wave length of the light and θ is the incident angle of the light to the exposed area. $nsin\theta$ can be called as numerical aperture (NA) of the lens. δ is known as Rayleigh resolution.

In real processes, minimum resolution does not only depend on diffraction effect, but also depends on printing process (imaging system and photoresist properties). By taking account these effects, Equation 1.1 can be rewritten as

$$\text{smallest feature} = k_1 \frac{\lambda}{NA} \tag{1.2}$$

where the k_1 is known as k-factor for a given process and it can change by different design and resist process. According to Rayleigh resolution formula to achieve smaller features, the wavelength has to be reduced. For example, to achieve feature sizes order of micrometer, UV light of g-line (λ = 436nm), h-line (λ = 405nm) and i-line (λ = 365 nm) can be used. But, if further resolution is needed Deep UV sources will be required such as KrF laser (λ = 248nm), ArF laser (λ = 193nm) or F_2 laser (λ = 157nm). However, changing of wavelength requires the use of new resist and a new lens system design. Also environmental effects such as dust have influences on resolution, therefore a well control working conditions are necessary. All of these effects increase the cost of the process per chip.

The aim of researches related to alternative lithography techniques is to reduce the cost of process or to push the resolution limits further. We will refer to alternative methods in this chapter.

1.1.1.2 Electron Beam Lithography

In contrast to the optical lithography, electron beam lithography (EBL) uses high energetic electrons (>20keV) instead of photons to expose the resist and the electron beam can be focused down to 1 nm. Since beam moves on the wafer, it is not necessary to use a mask in process. Nevertheless, EBL suffers from electron-electron interaction at the substrate-resist interface and slow movement of the beam to scan completely wafer surface. Also, working conditions, which requires vacuum atmosphere, make it costly production process. Secondary electrons created in the substrate interact with incoming electrons and the effective spot size of beam is enlarged resulting in exposure a large area of the resist layer. This is known as proximity effect and it is has an importance when the features to be created are very close each other. It is reported that sub-10nm resolution was achieved by using this method (Chen and Ahmed 1993, Cumming, et al. 1996).

To overcome the proximity effect, low energetic electrons (<1keV) can be used. But, in this case, new problems encountered is difficulty of focusing of electrons and low penetration depth which is require a new resist to exhibit a thinner layer profile.

1.1.1.3 Ion Beam Lithography

In ion beam lithography (IBL) an accelerated ion beam is employed to expose the resist layer. The penetration of ion species into resist is involved. When the beam hits the resist with an angle, reflections of an ion beam and proximity effect are insignificant any more. However, large atomic mass of ions when compared to electrons is a drawback of this method because of the fact that large mass reduces the resolution capability. By using this process, resolution less than 65nm is reported in the literature (Lee, et al. 1998)

1.1.1.4 X-Ray Lithography

X-ray lithography is accomplished like other exposing methods by changing the radiation source and resist material on the wafer. X-ray lithography uses the photons by taking advantage of the wavelength between 0.1 and 4nm. In standard IC industry processing, pattern with 75-125nm feature size can be fabricated. It is still the most prominent candidates for creation of patterns in order of 50nm (Silverman 1998).

1.1.1.5 Atomic Force Microscope Lithography Techniques

Scanning probe microscopy, which includes scanning tunneling microscopy (STM), atomic force microscopy (AFM) and scanning near-field optical microscopy (SNOM) was originally developed to analyze surface characteristics by means of interactions between tip and surface. In SPM family the most used techniques are STM and AFM. With the development of STM, researches were enabled to manipulate single atoms (Tseng, et al. 2005). While STM offers new approaches, at the same time, it has a significant restriction on sample selection. Because STM is based on tunneling current detection between tip and sample; therefore, samples should be conductive materials. Development of AFM has overcome this problem with ability of examine both conductive and nonconductive specimens, because in AFM operation forces between tip and sample were detected instead of tunneling current. Moreover, AFM operation can be performed in normal atmospheric conditions. Besides using of AFM as a characterization instrument, it has also drawn attention as a fabrication tool for nanoscale lithography (Avouris, et al. 1998).

In this part, AFM based nanolithography techniques are discussed. These techniques can be divided into 4 different titles; *Resist exposure by AFM, Mechanical modification, Thermally induced modification, Dip-pen lithography and Oxidation using SPM.*

Resist exposure by AFM uses a conductive tip as a localized electron source to expose a thin PMMA resist layer. This method is very similar to conventional EBL

except energy of electrons (10-100keV). The high electric field between conductive tip and sample surface enables the field emission of electrons from the tip. The electron radiation is absorbed by resist with chemical changing in its structure. One of the advantages of this method is that proximity effect is significantly reduced because of much lower acceleration voltage. STM electron exposure was first demonstrated by McCorn and Pease (McCord 1987). This method has been also demonstrated by Majumdar et al. (Majumdar, et al. 1992). And they obtained a line pattern with a width of 35 nm and periodicity of 68 nm. Wilder (Wilder, et al. 1998) has been found field emission current from the tip depends on tip sample distance and multiple-tip arrays were used with noncontact mode to eliminate tip wear effect. By using field emission current as a feedback signal, Ishibashi et al. applied the method on negative photo resist, RD2100N, and showed that resolution depends on resist thickness and amount of exposure determines the cross sectional shape of developed resist (Ishibashi, et al. 1998). Park et al. used siloxene as a positive resist to obtain higher writing speed, in other words, to reduce the resist exposure time (Park, et al. 1995). For voltage of 70 V and current of 1 nA, 1 mm/s writing speed and 40 nm line-width were reached by them.

Mechanical modification can be performed by pressing tip down on the surface. Features with dimension of 20 nm can be created using sharp tip and thin films (Hu, et al. 1998). This method first was demonstrated by Loenen at al. for Si (Van Loenen, et al. 1989). A similar process can be used for thin photo resist layers. Patterns created on the resist then transferred on a substrate by etching or lift-off process. However, in this method, resolution is limited by tip size and film thickness.

Thermally induced modification transfers features to the surface by heat-induced deformation using heated cantilever to pattern the surface. Heated cantilever softens the photo resist and pits on the contact area are formed. IBM applied this method for data storage applications. Data density of 1 TB/in^2 has been achieved by this method (Vettiger, et al. 2002).

Dip-pen lithography was introduced as a new direct-write SPM based lithographic method by Piner et al. (Piner, et al. 1999). This method is based on transporting molecular substances to a surface, like macroscopic transfer of an ink to paper, with the resolution of AFM. In the process, material on the tip is transferred to the substrate by capillary forces. In that work, they suggested that molecular transport occurs between tip and surface through a water bridge, when an AFM tip coated with

octadecanethiol (ODT) come to contact with surface. Line widths are dependent on the writing speed and temperature (Schwartz, et al. 2002). By this method, 15 nm resolution with sharp tips on single crystal surfaces was demonstrated (Pena, et al. 2003).

Oxidation using SPM was firstly demonstrated by Dagata et al. (Dagata, et al. 1990). He used STM to oxidize locally a Si surface. Created oxide features can play a role of mask for next lithography step. In addition, for thin metallic or semiconductor films, the oxide can form an insulating barrier by reaching to the insulating substrate. The benefits of this method, such as, high resolution, simplicity, low cost, make it attractive for sub 100 nm fabrication. Figure 1.2.a and Figure 1.2.b show some examples of this method. This study focuses on local oxidation and more detailed explanations about this method will be presented in chapter 2.

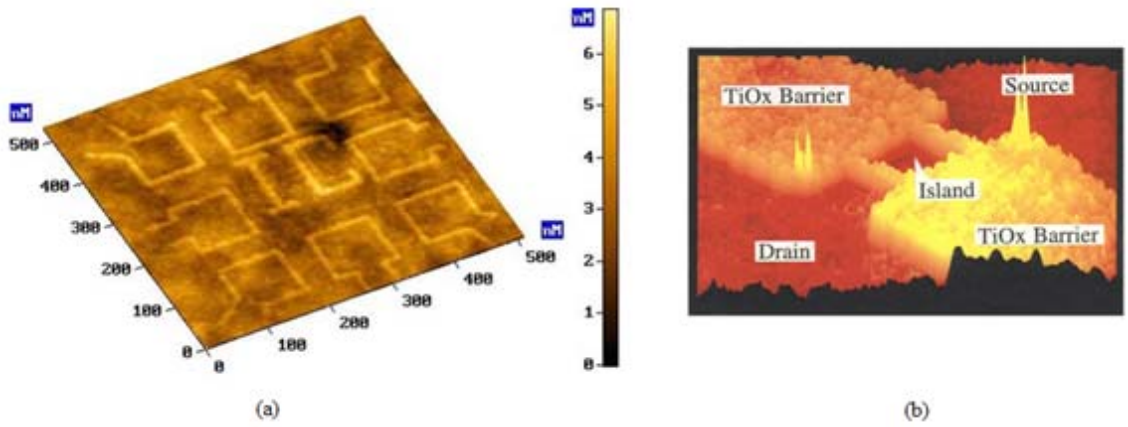

Figure 1.2. (a) AFM image of oxide line with minimum line width of 8 nm formed under 0.5 ms impulse at 8 V bias (Source: Lemeshko, et al. 2001). (b) Three-dimensional AFM image of fabricated back gate SET with one island structure (Source: Matsumoto 1998).

CHAPTER 2

OXIDATION OF METALLIC THIN FILMS WITH ATOMIC FORCE MICROSCOPE (AFM)

2.1. Principle of Atomic Force Microscope

The history of scanning probe microscopy (SPM) starts with the development of Scanning Tunneling Microscope (STM). After the invention of STM in 1982 (Binnig and Rohrer 1982), Atomic Force Microscope was developed by Binnig, Quate, and Gerber in 1985 as a surface characterization instrument (Binnig, at al. 1986). AFM is based on the analysis of long range Van der Waals forces and repulsive forces. Maybe the most important element of the system is a sharp tip, which moves over the surface interacting with the sample by means of atomic forces. Determining the deflection and torsion of the tip, information about the sample surface is obtained with a spatial resolution of a few nanometers, especially for z-direction provides sensitivity in angstrom scale. Some other devices with similar working principles, such as magnetic force microscope (MFM), electric force microscope (EFM) and scanning near-field optical microscope (SNOM), have been developed within a short period of time after the invention of AFM.

The main idea underlying the AFM working principle is to trace the movement of tip under the interactive forces with sample. The interactive forces can be explained by considering the van der Walls forces (Barash 1988): By considering two identical inert gas atoms, we can explain these forces. If they are far from each other; in other words, the distance (R) between these two atoms is large in comparison with the radii of the atoms, the interaction force between atoms would be zero. Nevertheless, if the atoms include dipole moments in each other, induced moments cause an attractive interaction between atoms. In this case, the total energy of the system would be,

$$\Delta U = -\frac{A}{R^6} \tag{2.1}$$

As can be seen from the Equation (2.1) this attractive interaction varies as the minus sixth power of the separation of the two atoms. This is called as van der Walls interaction or London interaction (Kittel 1976).

When the two atoms are brought together their charge distributions gradually overlap by changing the electrostatic energy of the system. At sufficiently close separations, the overlap energy becomes repulsive due to the Pauli Exclusion Principle. The most basic statement of this principle is that two electrons cannot have equal quantum numbers.

The Pauli principle prevents more than one electron from occupying the same energy state. Electron distribution of atoms with closed shell can overlap only if the electrons in an occupied state promote to unoccupied high energy states of the atoms. Thus the electron overlap increases the total energy of the system and gives a repulsive contribution to the interaction.

When used together with a long-range attractive potential of the form of Equation 2.1 experimental data on the inert gases can be fitted well by an empirical repulsive potential of the form of B/R^{12}, where B is a positive constant. The constant A and B are empirical parameters. The total potential energy of two atoms at separation R can be written as follows;

$$U(R) = 4\varepsilon\left[\left(\frac{\sigma}{R}\right)^{12} - \left(\frac{\sigma}{R}\right)^{6}\right] \tag{2.2}$$

where ε and σ are the new parameters and they come from experimental measurement on argon gases, $4\varepsilon\sigma^6 \equiv A$ and $4\varepsilon\sigma^{12} \equiv B$. The potential (2.2) is known as Lennard-Jones potential, Figure 2.1.

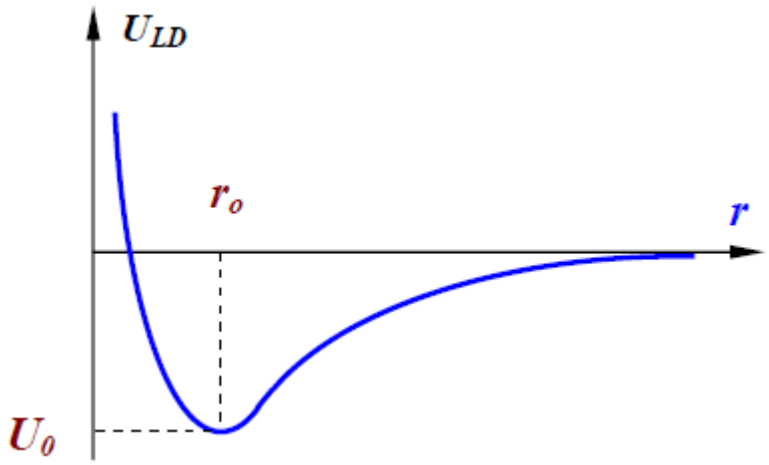

Figure 2.1. Lennard-Jones potential

(Source: Mironov 2004).

The force between the two atoms is given by –dU/dR. By using this relation, the force between two atoms at separation R can be derived from Equation (2.2), yielding

$$\vec{F}(r) = 24\frac{U_0}{\sigma}\left[2\left(\frac{\sigma}{r}\right)^{13} - \left(\frac{\sigma}{r}\right)^{7}\right]\hat{r} \qquad (2.3)$$

Equation (2.3) represents the force between two atoms.

As mentioned before, the data acquisition in AFM operation is done by detection of tip movement (deflection and torsion). The most popular method used for this purpose is "optical detection". An optical detection system includes a laser source and a four-quadrant photodiode. Initially, a laser beam emitted from the source is focused on the cantilever and reflected towards to the photo diode. As the beam hits to the diode, photocurrents are created by each section of diode and these can be used to determine the tip bending (due to the attractive or repulsive forces) or torsion (due to the lateral component of tip-sample interaction). If the individual currents created by each section are called as I_i (i = 1, 2, 3, 4), deflection and torsion of cantilever can be characterized with $\Delta I_Z = [(I_1+I_2)-(I_3+I_4)]$ and $\Delta I_Z = [(I_1+I_4)-(I_2+I_3)]$, respectively (Figure 2.2).

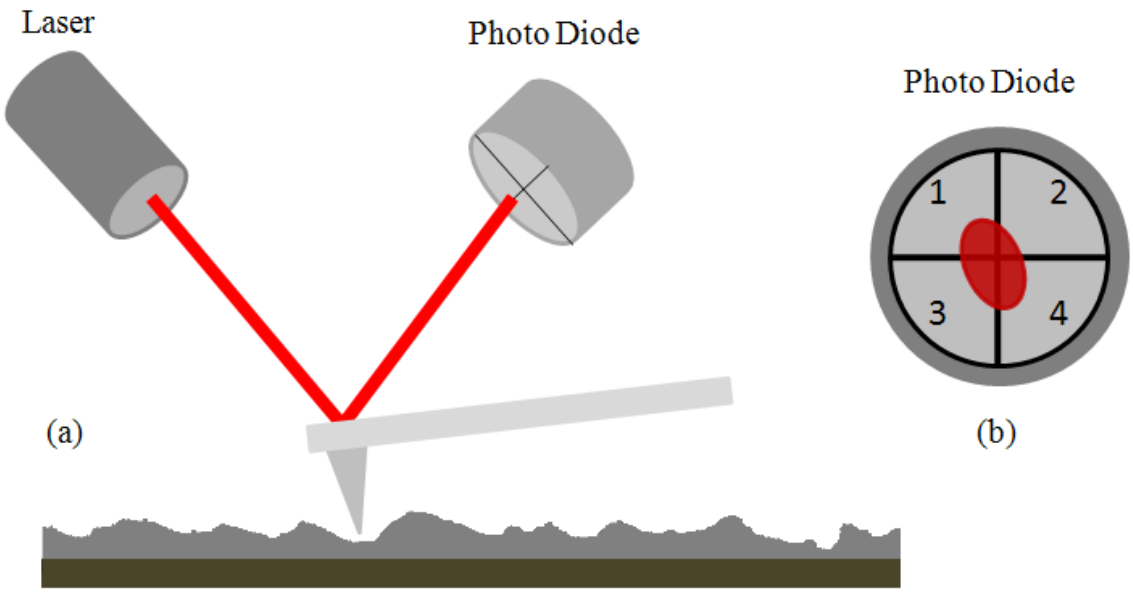

Figure 2.2. (a) Schematic description of optical detection system, (b) photodiode sections.

AFM uses a feedback system to keep the tip-sample separation constant, and current difference (ΔI_Z) is used as input signal of feedback system to control the ΔZ (tip bending). To adjust the value of ΔZ to the ΔZ_0 = constant (which is determined before the operation by the operator) a voltage is applied to the scanner. The scanner is made of a piezoelectric material and it generates a mechanical stress as a response to applied voltage; therefore, when voltage is applied to the Z electrode of the scanner, tip-sample separation (ΔZ) changes proportionally to value of applied voltage. To obtain topographical image of the sample surface, voltages applied to the scanner on each point of the surface are recorded in computer memory and a three dimensional f(x,y) graphic is created.

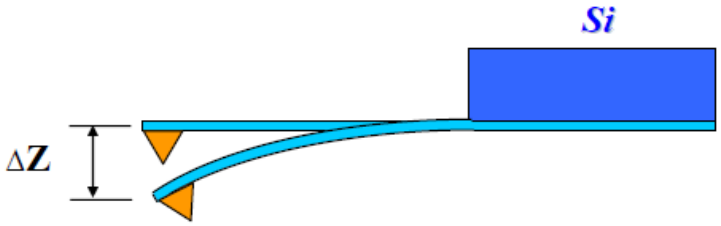

Figure 2.3. A schematic of a typical AFM tip and cantilever

(Source: Mironov 2004).

AFM uses special tips mounted at the end of a cantilever to be able to detect the interaction forces, and elastic cantilevers provide sensitivity to the measurement. A schematic of a typical AFM tip and cantilever can be seen in Figure 2.3. AFM cantilevers can be made of Si, SiO_2 or Si_3N_4 by using conventional photolithography and etching methods. According to the Hooke's Law, deflection of the cantilever can be written as;

$$F = k\Delta Z \tag{2.4}$$

where the deflection of cantilever ΔZ is determined by the acting force F and spring constant k. Another important parameter for cantilever is its harmonic frequencies; it is given by following formula (Birger, et al. 1979):

$$\omega_{ri} = \frac{\lambda_i}{l^2}\sqrt{\frac{EJ}{\rho S}} \tag{2.5}$$

where l is the cantilever length; E is the Young's modulus; J is the inertia moment of the cantilever cross-section; ρ is the material density; S is the cross section; λ_i is the numerical coefficient depending on the oscillation mode.

2.2. Oxidation Theory of Metals

Nearly all of the metals are covered by an insulator oxide layer when they are exposed to atmosphere because of presence of oxygen. This natural layer with a thickness of a few nanometers plays a role of protective layer against further oxidation of metal.

Oxidation is initially occurs very rapidly; however, after a few minutes or hours rate of oxidation drops to negligible values and stable film is formed on the surface. This behavior is very similar for all metals.

It is well known that the thickness of oxide increases proportional to the square root of time.

$$h(t) \propto t^{1/2} \tag{2.6}$$

This equation is known as parabolic law and it was confirmed theoretically by **Tammann, Pilling and Bedworth** (Tamman 1920, Pilling and Bedworth 1923). They used following assumptions;

- Oxidation growth occurs by uncharged particles
- The diffusion coefficient D is independent of concentration C
- The concentration in metal-oxide interface C(0) and the concentration in oxide-gas interface C(L) are independent of film thickness L

Fick's law, which relates flux to the concentration field with magnitude that is proportional to the concentration gradient, says that the particle current J is

$$J = -D\frac{\partial C}{\partial x} \tag{2.7}$$

If the concentration doesn't change with time we can write

$$\frac{\partial C}{\partial t} = 0 \tag{2.8}$$

and using Fick's second law and considering film growth is steady state phenomenon, in other words the concentration doesn't change by time, we found that

$$\frac{\partial J}{\partial x} = -\frac{\partial C}{\partial t} \tag{2.9}$$

As can be seen J is independent of the x in the film. Therefore Fick's first law takes a form of

$$\frac{\partial C(x)}{\partial x} = -\frac{J}{D} = const. \tag{2.10}$$

By integrating equation 2.10 for interface we get

$$J = D\left[C(0) - C(L)\right]/L \tag{2.11}$$

If we describe R as volume of oxide formed per particle which diffuses from one interface of the oxide to the opposite interface, we can get the following equation for the rate of oxidation:

$$RJ = \frac{dL(t)}{dt} = \frac{RD\left[C(0) - C(L)\right]}{L(t)} \tag{2.12}$$

By using separation of variables method and fixed boundary conditions and a constant diffusion coefficient we can yield a parabolic growth law:

$$L(t)^2 - L(0)^2 = 2kt \tag{2.13}$$

where $k = RD[C(0)\text{-}C(L)]$.

In contrast to Tammann and Pilling-Bedworth theory, **Wagner's theory** assumes that metal oxidation occurs by means of diffusion of charged particles (Wagner 1933). His starting point was the differential equation for linear diffusion of charged particles.

$$J = -D\frac{dC(x)}{dx} + \mu E(x)C(x) \tag{2.14}$$

where, E is the electric field and μ is the mobility and C is the concentration of the diffusing charged defects instead of the ionic concentration of the lattice.

Wagner supposed that during the growth, neutral oxide is formed. This assumption requires that the number of positively charged ions (cations) moving through the oxide in unit time should be equal to the number of negatively charged ions (anions) and electrons moving through the oxide in unit time. In this case, total charge transported through the oxide at each point in time will be the sum of all particle contributions and it will be zero:

$$\sum_{s=1}^{r} Z_s e J_z = 0 \tag{2.15}$$

This equation is referred to as the coupled-current condition.

Wagner solved the coupled diffusion equations. But, it should be noted that Wagner used important assumptions to get this equations which can be stated as "Local chemical reactions occurs between charged and neutral species in the oxide layer. These chemical reactions are close enough to equilibrium in each volume element. Therefore equilibrium conditions can be employed."

Wagner's theory cannot help us to understand the mechanism of oxidation, but it is important for taking account the diffusion of charged particles. This feature of theory led the well organized theories of metal oxidation.

N. Mott and N. Cabrera developed the theory of oxidation, based on assumption of the influence of a potential built up across the growing oxide film (Cabrera and Mott 1949). Here, we will mention about the theory of the rate of thin films. In other words, the effect of any space charge set up by the dissolved ions is negligible, so that the movement of ions and of electrons can be considered independently.

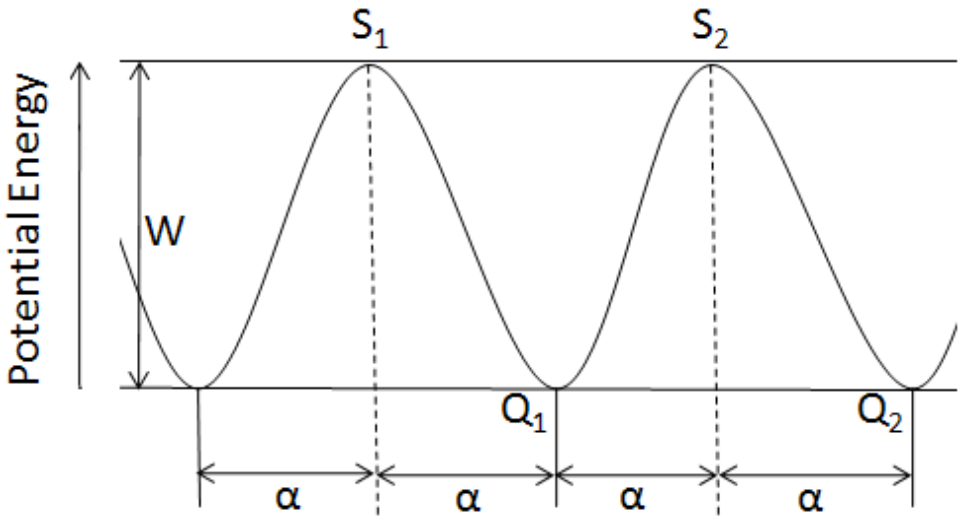

Figure 2.4. Potential energy of an interstitial of ions.

Now, we consider a metal-oxide-oxygen system. According to model, electrons can pass through oxide layer either by thermo ionic emission and quantum mechanical tunneling and this process is much faster than the diffusion of ions. At the end of the electron diffusion some of the absorbed oxygen ions will be converted to the O^- ions by setting up an electric field across the oxide film. In this case, the electrostatic potential is given by the difference in the metal Fermi level and the oxygen O^- energy level. This electrostatic potential is also called as Mott potential or contact potential. The electronic levels in the metal-oxide-oxygen system are shown in Figure 2.5.

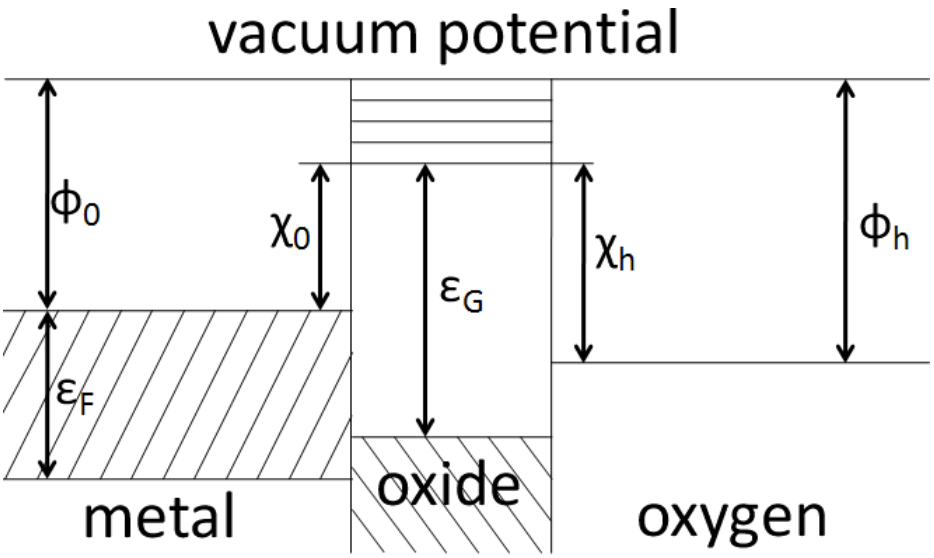

Figure 2.5. Idealized energy band diagram for the metal-oxide-oxygen system.

If the space charge can be neglected in the oxide film, an homogenous electric field will be equal to V_m / h. In consideration of very thin oxide film, the electric field will be so strong that the diffusion velocity of the ionic species is no longer proportional to the field. In this case, one ion has to go over a potential barrier W for ionic motion (Figure 2.4). The presence of the field depresses the barrier between Q_1 and Q_2. Then the chance per unit time that the atom will escape over the barrier to Q_1 ($vexp(-W/kT)$) will change as follows;

$$\nu \exp(-W/kT)\exp\left(\frac{q\alpha E}{kT}\right) \tag{2.16}$$

where ν is the atomic frequency of vibration. In this case the rate of growth of the oxide film is

$$\frac{dX}{dt} = N\Omega\nu \exp(-W/kT)\exp\left(\frac{q\alpha E}{kT}\right) \tag{2.46}$$

where N is the number of ions per unit area, Ω is the volume of the oxide formed by the transversal of a single ion and E is the electric field in the film.

Formula 2.46 can explain both the growth of oxide film in oxygen and anodic formation of oxide film in an electrolyte containing oxide ions. In either case the equation 2.46 can be written as

$$\frac{dX}{dt} = u\exp(X_1/X) \tag{2.47}$$

where $X_1 = q\alpha V_m/kT$, $u = u_0\exp(-W/kT)$, $u_0 = N\Omega\nu$.

2.3. Local Oxidation via Atomic Force Microscope

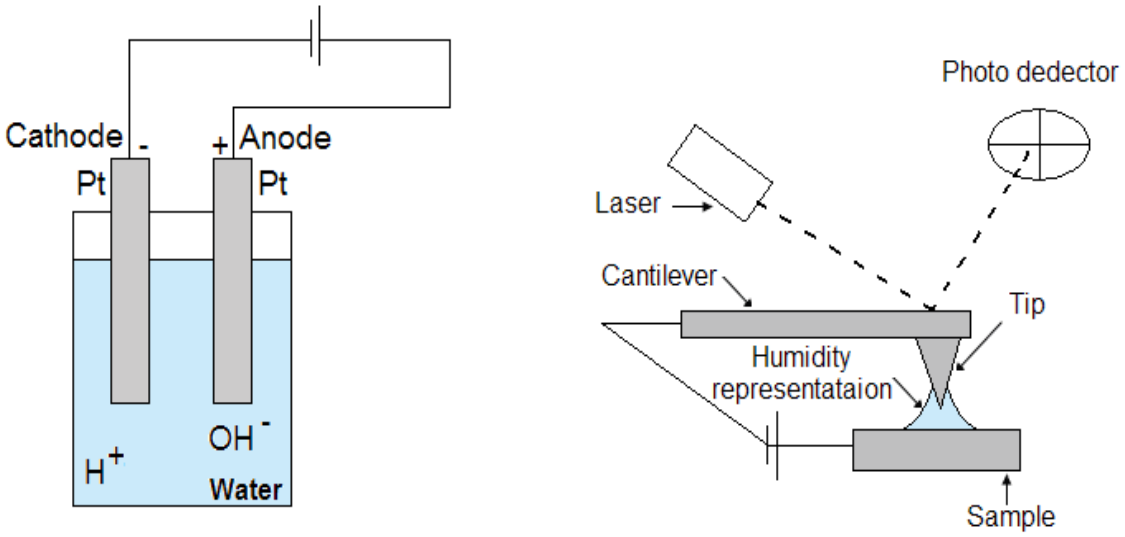

Figure 2.6. An example of conventional electrolytic system and AFM system.

In local oxidation via an SPM, a negative bias voltage is applied to the conductive AFM tip, and this voltage generates an intense electric field (10^9V/m) at the

apex of an AFM tip. Also, there is always a water layer on the sample surface because of humidity in the environment (Shindo, et al. 1996). In these aspects, we can say that oxidation using AFM is similar to the conventional anodic oxidation process. Therefore, oxidation via AFM is considered as an electrochemical process and is also called as local anodic oxidation. An example of conventional electrolytic system and AFM system can be seen from Figure 2.6. There are two electrodes which are composed of platinum in water based electrolyte medium. When compared to AFM system, the electric field generated between electrodes is much less.

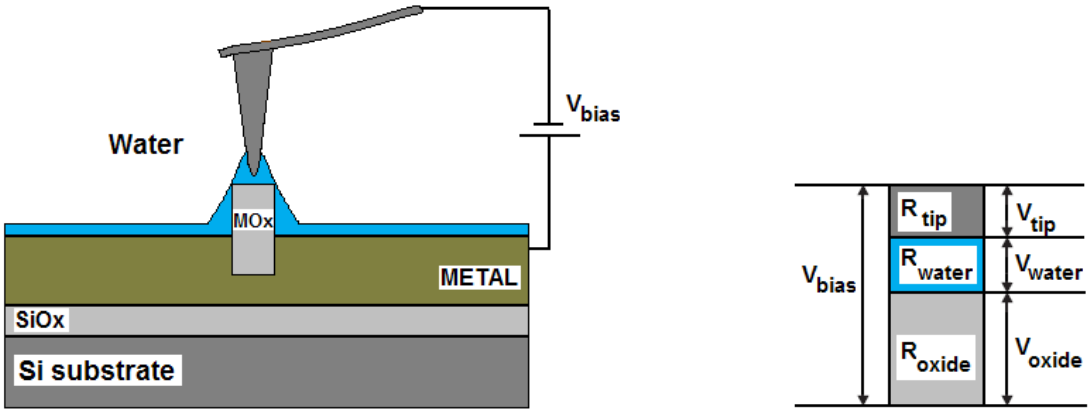

Figure 2.7. A schematic of the oxidation via AFM.

A schematic of the oxidation via AFM can be seen from Figure 2.7. Actually, voltage across the oxide layer will not be equal to the applied voltage. There is always a loss of voltage due to the water layer, even due to the tip. This means that $\boldsymbol{V=V_{tip}+V_{water}+V_{oxide}}$. V_{tip} may be ignored if it is considered that the tip is well conductive.

Water layer plays a role in local oxidation process as an electrolyte in a similar way in standard macroscopic electrolytic process. When an AFM tip comes sufficiently close to the surface, a water bridge formation occurs between the tip and sample surface because of the capillary force. This water bridge behaves as a source of oxyanions. To start an electrochemical reaction, a minimum voltage should be applied between the conductive AFM tip and sample surface. The applied voltage creates an electric field

with strength of ~$10^{9}Vm^{-1}$ between the tip and the sample surface. That strength has sufficient energy to decompose water molecules into hydrogen (H^{+}) and hydroxide (OH^{-}) ions between the tip and sample surface (Lo, et al. 2006, Hu, et al. 2003, Nishimura, et al. 2007, Hsu, et al. 2008). The negatively charged hydroxide ions are accelerated by the field to the surface of the metal film establishing the electrochemical oxidation process on the film (see Figure 2.8.). If we consider that an initial oxide layer exist on the surface (native oxide), migration of hydroxide ions through the oxide layer also enhanced by the intense electric field. The oxidation time, the magnitude of bias voltage and relative humidity control the height and the protrusion width of the metal oxide nanopatterns.

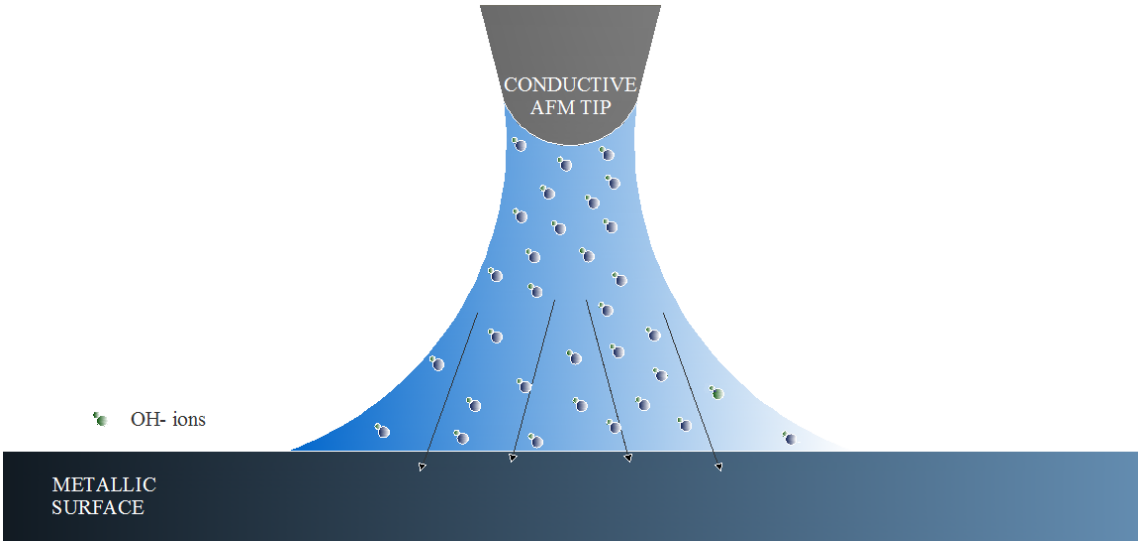

Figure 2.8. Acceleration of OH^{-} ions to the surface.

CHAPTER 3

EXPERIMENTAL DETAILS

This chapter consists of three main parts. In the first part, both preparation of thin films and fabrication of oxide structures on these thin films were explained. In the second part, some techniques we have used in this study to characterize our samples were introduced. Finally, in the last part, photolithography technique and oxidation of lithographically created Ta lines were represented.

3.1. Sample Preparation

Our sample preparation procedure includes thin film deposition, thermal oxidation of silicon substrates and fabrication of oxide structures on metallic surfaces.

3.1.1. Thin Film Deposition

To investigate the growth kinetics and to perform characterization of oxide structures, our metallic thin films were prepared by DC magnetron sputtering system. Films were deposited on n-type Si (100), SiO_2 on n-type Si (100), and thermally oxidized SiO_x on p-type Si substrates. Table 3.1 summarizes the growth parameters of our thin films.

In this study we used two different sputter systems available in the Department of Physics at Izmir Institute of Technology. Our tantalum (Ta) thin films were prepared

in chamber of ATC Orion 5 UHV Sputtering System (AJA International). However, hafnium (Hf) and zirconium (Zr) thin films were deposited in chamber of a home-made sputtering system.

Table 3.1. Sputtering parameters of thin films.

Material	**Substrate**	**Pressure (Torr)**	**Power (W)**	**Time**	**Argon flow rate**
Ta	n-type Si/SO_2	$\sim 10^{-7}$	20W	17 min	10sccm
	Si/SiO_x			6 min	
Hf	n-type Si	$\sim 10^{-6}$	30W	25 min	30sccm
	Si/SiOx				
Zr	n-type Si	$\sim 10^{-6}$	20 W	25 min	30sccm
	Si/SiOx				

3.1.2. Thermal Oxidation of Silicon Substrates

To perform electrical characterization, we deposited our materials on thermally grown SiO_x films. Oxidation of p-type Si substrates took place in a tube furnace (see Figure 3.1) with an oxygen flow parallel to the sample. This process is called as dry oxidation of Si.

Figure 3.1. Tube furnace used for dry oxidation.

In this process, temperature of the furnace was kept constant at 1200^0Cfor 3 hours. Resulting oxide thickness was measured with an ellipsometer. Figure 3.2 shows an oxide growth chart for dry oxidation of Si.

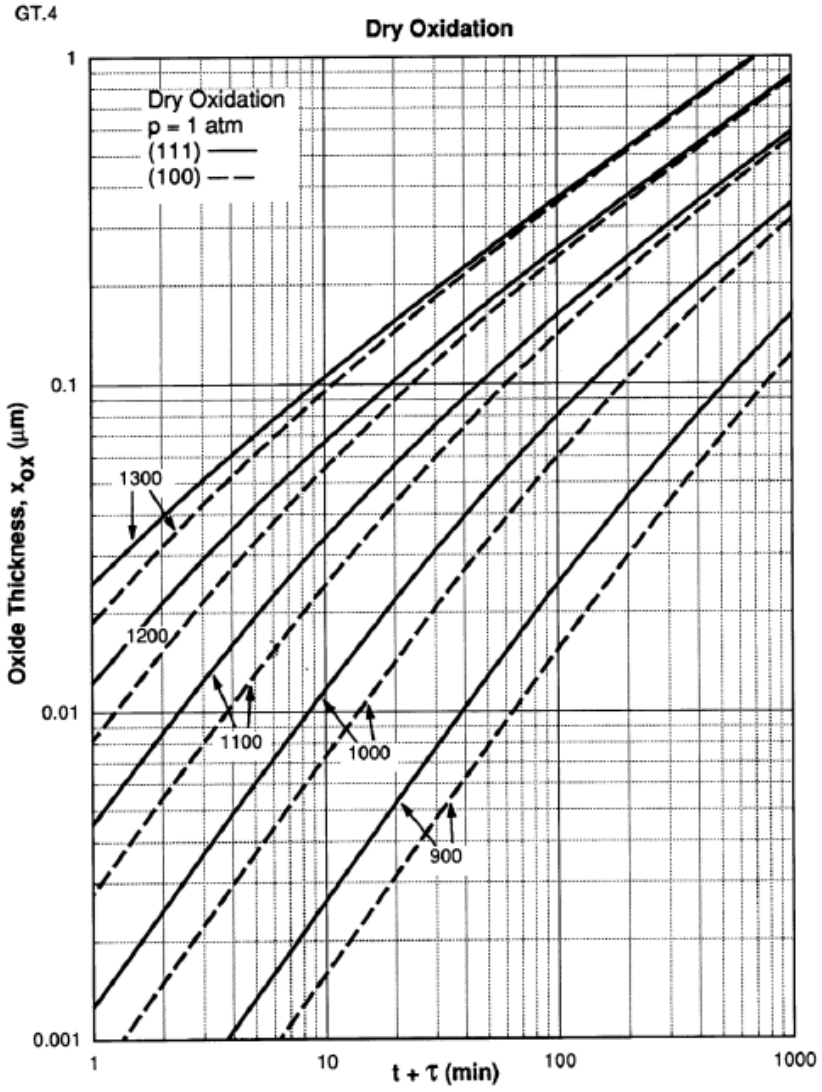

Figure 3.2. Dry oxidation growth chart for Si

(Source: University of Illinois at Urbana-Champaign-ECE 2009)

3.1.3. Fabrication of Oxide Structures on Metallic Surfaces

In our study, Semi-Contact Scanning Probe Lithography (SC-SPL) or local anodic oxidation via AFM was performed to investigate a few parameters affective on the oxide growth. These parameters investigated in our study are applied voltage, voltage duration and relative humidity in the environment. Our experimental setup is shown in Figure 3.3. The AFM system stands on a vibration isolation table to prevent

the mechanical vibrations from the environment. Optic camera integrated into the system sends the image to the computer screen and helps to determine the tip position on the sample. In the Figure 3.3, position of the sample and humidity sensor can be seen as well. Also, the laser source and photodiode which are essential parts of the AFM system can be seen from the same figure. The sample holder designed for electrical operations is also seen in Figure 3.3.

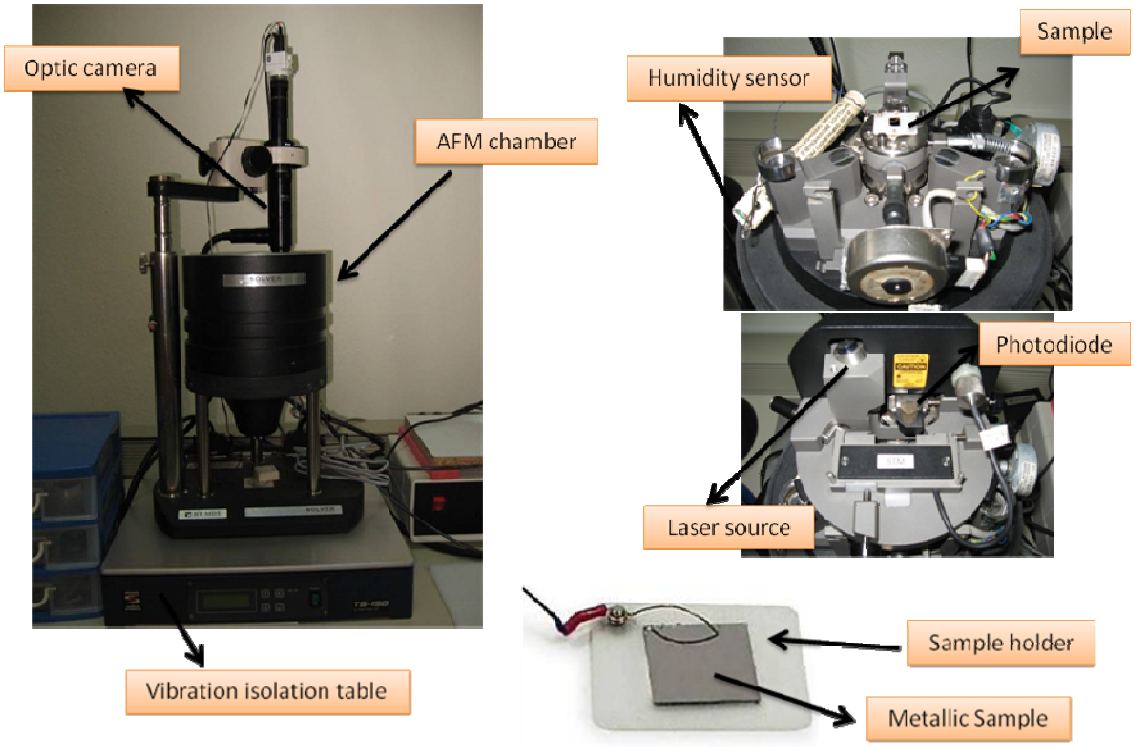

Figure 3.3 AFM local oxidation setup.

In SC-SPL operation, conductive AFM tip was kept a negative potential with respect to the sample surface. As mentioned before in chapter 2, when the AFM tip comes sufficiently close to the surface, a water bridge is formed between AFM tip and surface. After the formation of the water bridge, if a potential difference is applied between tip and sample, decomposition of water will exist and OH^- and H^+ ions will be created. Negatively charged hydroxyl ions will be accelerated to the surface under the applied voltage and finally oxide formation occurs (see Figure 2.8). In our study, the

distance between tip and surface was kept at approximately 10 nm. This distance was adjusted obtaining set-point vs. height curve. Figure 3.4 shows an example of set-point vs. height curve. During the experiments, the maximum applied voltage difference between AFM tip and surface was 10 V. Giving increments to the applied voltage, changes in dimension were analyzed.

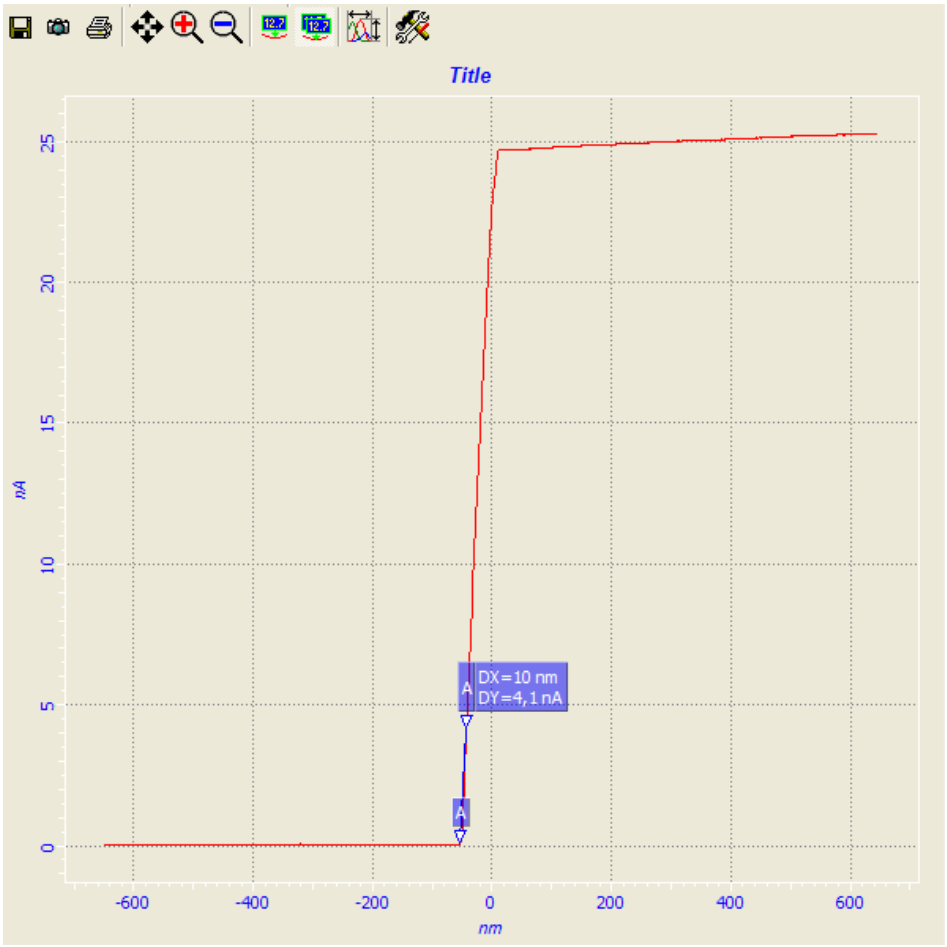

Figure 3.4. Set point vs. height curve.

In addition to the applied voltage, effect of voltage duration was investigated. Standard software of our AFM system is able to move the tip along any predefined two-dimensional path at the desired speed and it also controls the voltage difference between tip and sample. To investigate the voltage duration, fabrication of oxide lines on metallic surfaces was performed with different velocities. In each process, we created

oxide lines-with length of 4 μm. The oxidation time; in other words, the time the tip spends above a certain position on the predetermined trajectory was calculated as follows: length of the oxide line was divided by the diameter of the tip, and then total oxidation time (the time spent during the oxide line formation) is divided by the result obtained from first calculation.

The third parameter, relative humidity, was studied under different environmental conditions. As shown in the Figure 3.3, our AFM system has a chamber to prevent the acoustic noise. This chamber also provided an opportunity to be able to control relative humidity in the AFM environment. A humidity sensor was placed into the chamber to monitor the variation in the relative humidity. To adjust the relative humidity, inner wall of the chamber was wetted with DI water. Pure nitrogen gas was introduced into the chamber and the relative humidity was monitored on a computer screen by humidity sensor. By adjusting the gas flow rate by hand, we kept the relative humidity at a certain value. To obtain a sufficient stability in relative humidity, we waited until a variation in relative humidity of less than 2% was appeared. This stability of the relative humidity was sufficient to perform oxidation procedure at the adjusted level.

3.2. Characterization

Both dimensional and electrical characterization of created oxide structures were performed via atomic force microscopy techniques. For dimensional characterization, surface topography images were obtained in semi-contact (tapping) mode. Electric force microscopy was also performed in semi-contact mode by using second pass technique. Finally, spreading resistance images were achieved in contact mode by detecting current passing between conductive AFM tip and sample surface.

3.2.1. AFM Surface Characterization

AFM surface characterization was performed in semi-contact (tapping) mode operation using commercial Scanning Probe Microscopy instrument (Solver Pro 7 from MNT-MDT, Russia). During all scans a conductive diamond like carbon coated tip (DLC tip from same company) with a curvature of 75 nm was employed (see properties of the tip from Figure 3.5), and the closed loop feedback system was kept active. SEM image of conductive tip can be seen from Figure 3.5. The root mean square (RMS) roughness was gained for 25μm^2 surface area. Surface topography measurements were performed just before and after the surface oxidation process. AFM topography images of created oxide structures were obtained after the local oxidation process of thin films.

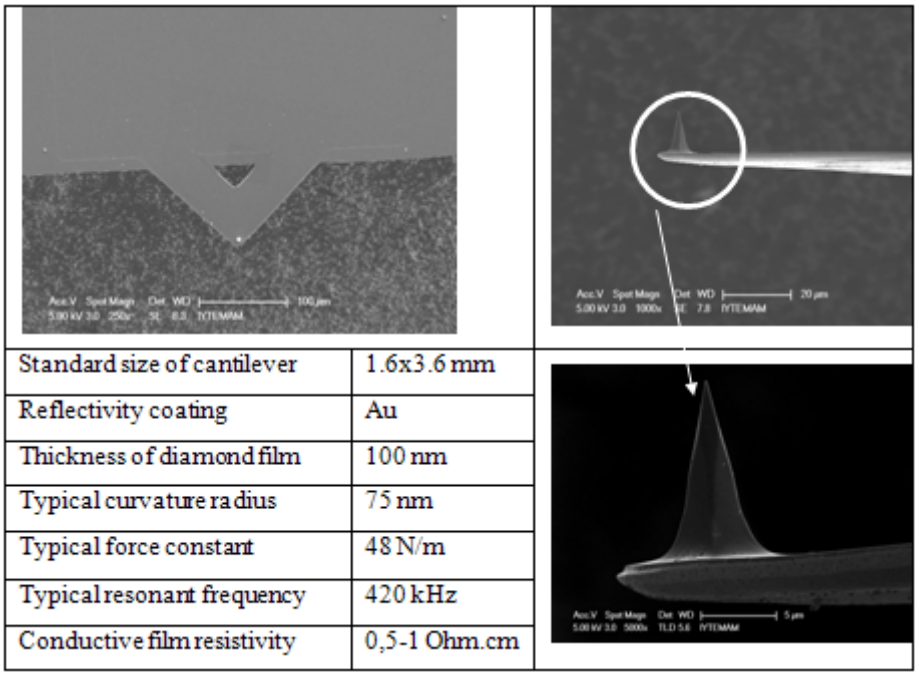

Standard size of cantilever	1.6x3.6 mm
Reflectivity coating	Au
Thickness of diamond film	100 nm
Typical curvature radius	75 nm
Typical force constant	48 N/m
Typical resonant frequency	420 kHz
Conductive film resistivity	0,5-1 Ohm.cm

Figure 3.5. SEM images and specifications of conductive AFM tip.

3.2.2. AFM Electrical Characterization (I-V, EFM, SRM)

To investigate the electrical characteristics of created oxide structures on the metallic films I-V curves were obtained. Our AFM instrument allows us to make two-terminal electrical measurement. In this setup, DLC coated conducting AFM tip used as an electrode. To be able to apply potential difference between the AFM tip and sample surface, we used a sample holder which has a special design including contact electrode as a part of holder. Figure 3.3 shows the special sample holder design. During all electrical characterizations and oxide fabrication procedure, this sample holder was used. Figure 3.6 demonstrates the I-V measurement setup. Two terminal electrical measurements were done in contact mode operation allowing the AFM tip to touch the oxide layer or metallic surface. The distance between the conductive tip and counter electrode was kept at ~5 mm. I-V curves were obtained applying a voltage between -10 V and +10 V.

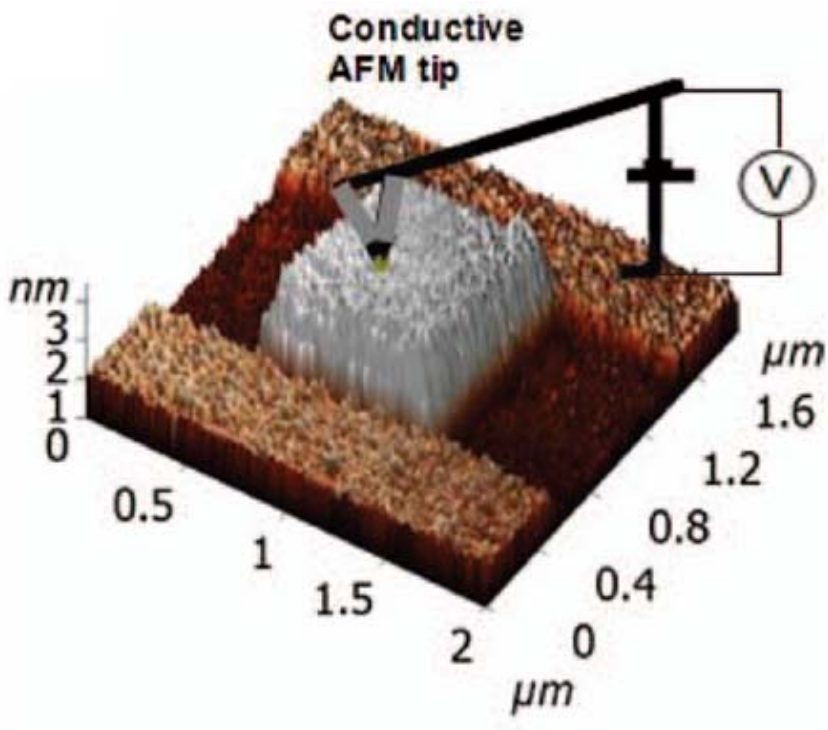

Figure 3.6. I-V measurement setup for oxide structure on a thin film.

Our electrical characterization techniques also include electrical force microscopy (EFM) and spreading resistance measurements (SRM). EFM is a technique for imaging electric field and electric charge distribution on the sample surface with high spatial resolution. In this technique, spatial distribution of the Z-component of the electric field gradient is used to obtain an EFM image. This technique is required a standard conductive AFM tip. To minimize the effect of topography, two-pass technique is used during EFM operation.

Basics of the EFM measurement can be understood from Figure 3.7.

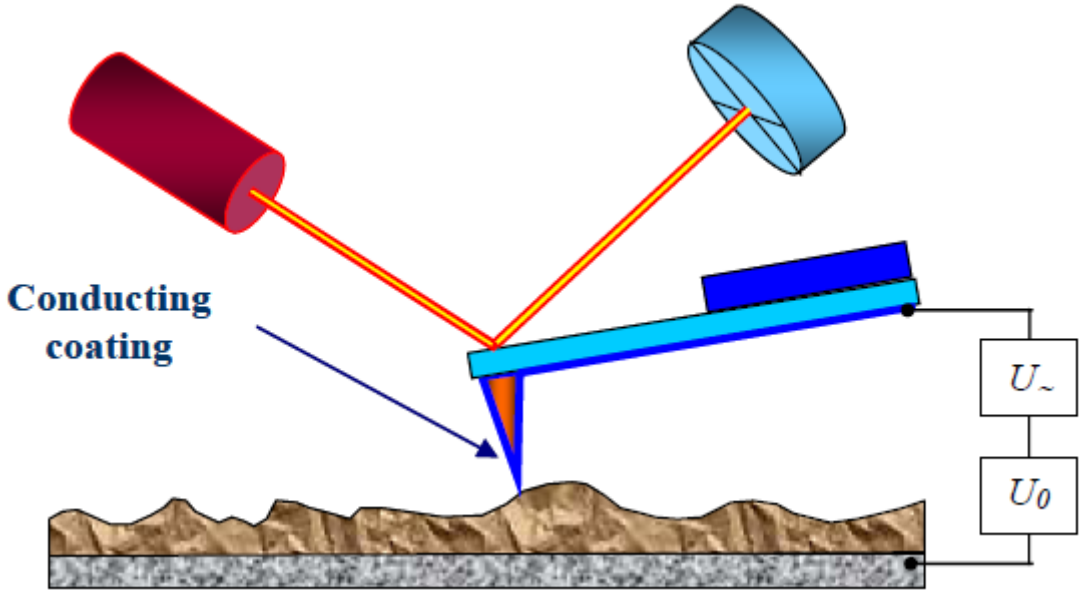

Figure 3.7. EFM measurement schematic.

(Source: Mironov 2004)

During operation a constant voltage U_0 and a variable voltage $U_{\sim}=U_1\sin(\omega t)$ are applied to the sample. In this case, the voltage between AFM tip and surface will be

$$U = U_0 + U_1 \sin(\omega t) \qquad (3.1)$$

and stored energy in this system will be

$$E = \frac{CU^2}{2} \tag{3.2}$$

and electric force between tip and sample surface can be written as

$$\vec{F} = -grad(E) \tag{3.3}$$

Z-component of the electric force between tip and surface is

$$F_z = -\frac{\partial E}{\partial z} = -\frac{1}{2}U^2\frac{\partial C}{\partial z} = -\frac{1}{2}\left[U_0 + U_1\sin(\omega t)\right]^2\frac{\partial C}{\partial z} \tag{3.4}$$

By using identity of $\sin^2(\omega t) = [1-\cos(2\,\omega t)] / 2$, Equation 3.4 can be written as

$$F_z = -\frac{1}{2}\left\{{U_0}^2 + 2U_0U_1\sin(\omega t) + \frac{1}{2}{U_1}^2\left[1-\cos(2\omega t)\right]\right\}\frac{\partial C}{\partial z} \tag{3.5}$$

According to the last expression F_z is the sum of three components which are:

$$F_{z(\omega=0)} = -\frac{1}{2}\left\{{U_0}^2 + \frac{1}{2}{U_1}^2\right\}\frac{\partial C}{\partial z}\ constant\ component; \tag{3.6}$$

$$F_{z(\omega)} = -\{U_0 U_1 \sin(\omega t)\}\frac{\partial C}{\partial z} \; component \; at \; frequency \; \omega; \tag{3.7}$$

$$F_{z(2\omega)} = \left\{\frac{1}{4}U_1^{\,2}\cos(2\omega t)\right\}\frac{\partial C}{\partial z} \; component \; at \; frequency \; 2\omega \tag{3.8}$$

The detection of the cantilever oscillation amplitude at frequency 2ω allows to obtaining of the derivative of the capacity with respect to the z-coordinate. This technique is named as Scanning Capacitance Microscopy (SCM). Also, detection of cantilever oscillation amplitude at frequency ω allows to obtaining of surface potential distribution in case of that the sample is a semiconductor or a dielectric, and this technique is known as Kelvin Probe Microscopy (KPM).

Achievement of high resolution EFM image is required that the electric force must be essentially based on the interaction between the AFM tip and the sample surface. Using a rough approximation, electric force between cantilever and sample F_{cs} is written as:

$$F_{cs} = -\frac{1}{2}U^2\frac{\partial C}{\partial z} \cong -\frac{1}{2}\alpha U^2\frac{LW}{H^2} \tag{3.9}$$

where α is a constant, L and W are the cantilever length and width, respectively. H is the distance between cantilever and sample surface. To obtain high resolution EFM image, the force between cantilever and sample surface should be eliminated. To solve the problem based on interaction force between cantilever and surface, two-pass technique is used. Figure 3.8 describes the technique. During the first scan, the tip oscillates with a frequency close to its resonance frequency ω_0 and the surface topography of the sample is recorded. After this; in second pass, the tip is lifted above the surface at a constant distance, and a variable voltage with a frequency $\omega = \omega_0$ is applied to the AFM tip. The tip follows the trajectory obtained during the first scan. Since the h is constant during second-scan, changes of oscillation amplitude of the tip

must be due to the changes of capacity of the system, in other words due to the local dielectric properties of the surface.

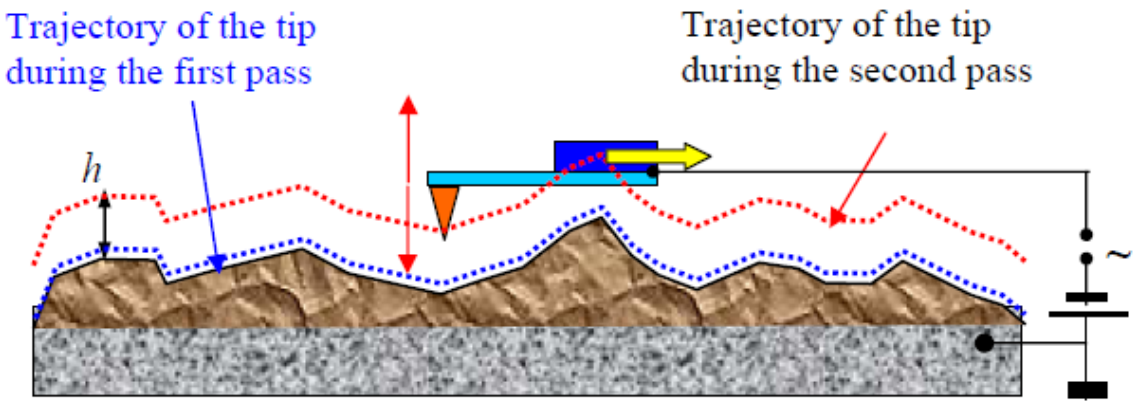

Figure 3.8. Two-pass technique schematic.

(Source: Mironov 2004)

In SRM, a voltage difference is applied between a conducting AFM tip and sample surface while the tip scan on the sample surface in contact mode operation. In this technique, an atomic force microscope is used to measure the local resistance of a sample. During scan, the current passing through the tip is saved for each x-y coordinate. Finally, a three dimensional spreading resistance map is created. In our study, we applied a voltage difference of 3V between tip and sample surface during the tip moves on locally oxidized surface and obtain a distinct contrast between modified and unmodified surface.

3.3. Fabrication of Tantalum Electrode and Ta/TaO_x/Ta Structure

To fabricate metal/oxide/metal structure, photolithography and SPM nanolithography methods were combined. Fabrication of Ta/TaO_x/Ta structure consists of two main steps. First, tantalum stripe was created on SiO_x substrate using

photolithography technique. After, Ta stripe formation, SPM nanolithography method was employed to create insulator region in tantalum stripe.

3.3.1. Photolithography and Liftoff Process

Fabrication of Ta/TaO_x/Ta structures stars with cleaning procedure. Because of all types of lithography process need well cleaned substrates in order to get fine structures, prior to film growth, following cleaning procedure was performed. To get rid of some defects stem from dust or some other types of particles, ultrasonic cleaning was utilized for cleaning process. Thermally oxidized SiO_x substrate was rinsed in acetone in ultrasonic cleaner with 20 minutes and then rinsed into iso-propyl alcohol and dipped into pure water bath, respectively. Finally, nitrogen was used for drying the substrate as final step of cleaning. This cleaning procedure made the substrate acceptable for lithography process.

After sample cleaning, we continued with the photolithography procedure including following steps; spin coating, soft (pre) baking, alignment and exposure, developing and hard baking.

There are two types of photoresist which are used in micro fabrication; positive and negative photoresist. Both of the resist consist of organic molecules. When a positive resist is exposed, the polymers break up in smaller parts. Breaking of chains makes the exposed material more easily dissolvable. When the resist-coated substrate immersed into a special solvent, only the resist in exposed parts will be washed away. For the negative photoresist, the process will be reversed. When a negative photoresist is exposed, the monomers will cross link and forms polymer which is no longer dissolvable. Only the photo resist in exposed areas will remain on the surface after the development. In spin coating step, we used spin coat Ge-8 (from Speciality Coating System, Inc.) as a spin coater (see Figure 3.11.b). In our work, AZ 5214 reversable photoresist was used. Spin coating was performed at 4000 rpm for 45 second. According to the AFM topography measurement, 400 nm thick photoresist was coated on the thermally oxidized SiO_x substrate.

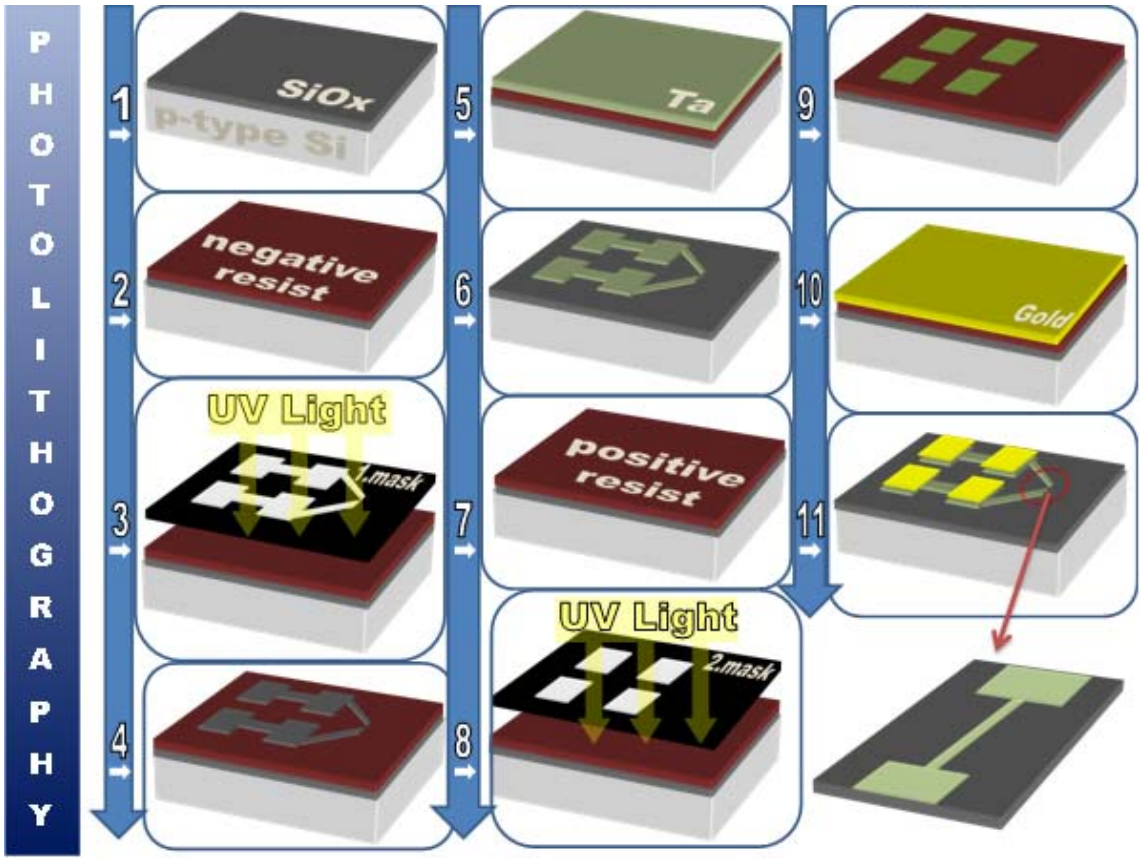

Figure 3.9. Photolithography steps. (1) cleaning, (2) negative resist coating, (3) UV light exposure, (4) development, (5) Ta growth, (6) resist liftoff, (7) positive resist coating, (8) UV light exposure, (9) development, (10) gold layer growth, (11) resist lift-off.

After the spin coating soft baking was applied as a second step in order to improve photoresist-sample surface adhesion. Soft baking step promotes resist uniformity and drives off most of solvent in photoresist. In our experiments, baking temperature and time were determined as 110^0C and 50 second on a hotplate (see Figure 3.11.c) by taking account the photoresist characteristics.

Transfer of the mask image (see Figure 3.10) to the resist-coated sample occurred in alignment and exposure step by activating photosensitive components of photoresist. A mask aligner system (from OAI) was used in this step (see Figure 3.11.a). After a lot of training, the appropriate exposure time was determined as 1 second for our work. This exposure time corresponds to an exposure of 28,6mJ/cm^2.

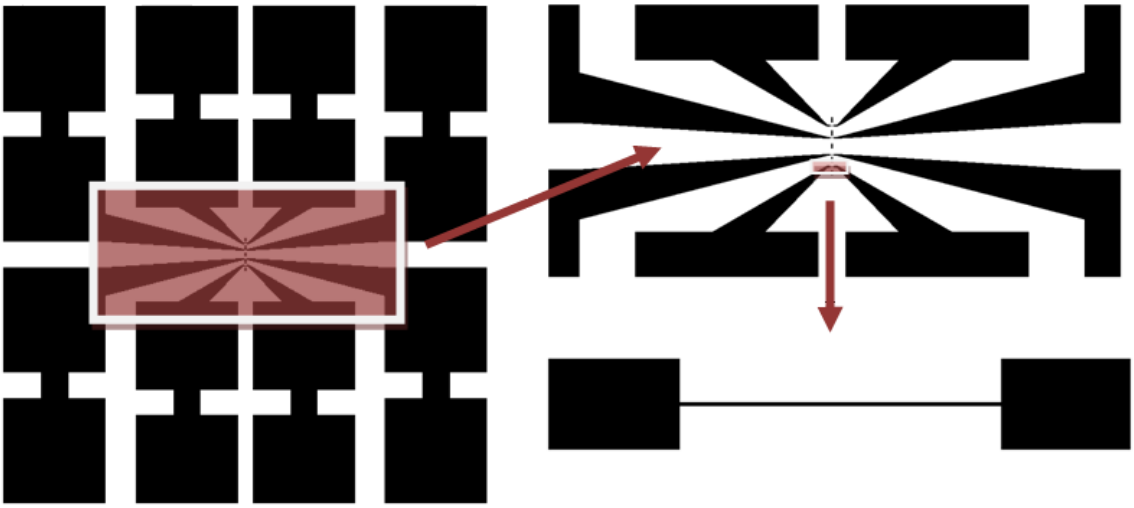

Figure 3.10. Mask design used for exposure the negative photoresist.

For our photoresist, the image reversal capability is obtained by a special crosslinking agent in the resist formulation which becomes active at temperature above 110^0C. The crosslinking agent is almost insoluble in developer while the unexposed areas still behave like a normal unexposed positive photoresist. In reversal bake step, resist-coated sample was placed on a hotplate with temperature of 120^0C for 2 minutes. After a flood exposure this areas are dissolved in standard developer for positive photoresist and the crosslinked areas remain. As a result, negative image of mask pattern was obtained on the sample surface.

After the reversal bake step was achieved, photoresist development was performed. In this step, as a developer AZ 726 MIF was used to develop our photoresist. Dipping the sample into the developer and waiting for 60 second, the photoresist in the unexposed area was removed. Then developer remaining on the sample surface was removed in pure water bath. End of the step, visible patterns appeared on the sample surface and sample was inspected to verify the quality of pattern by using the optical microscope.

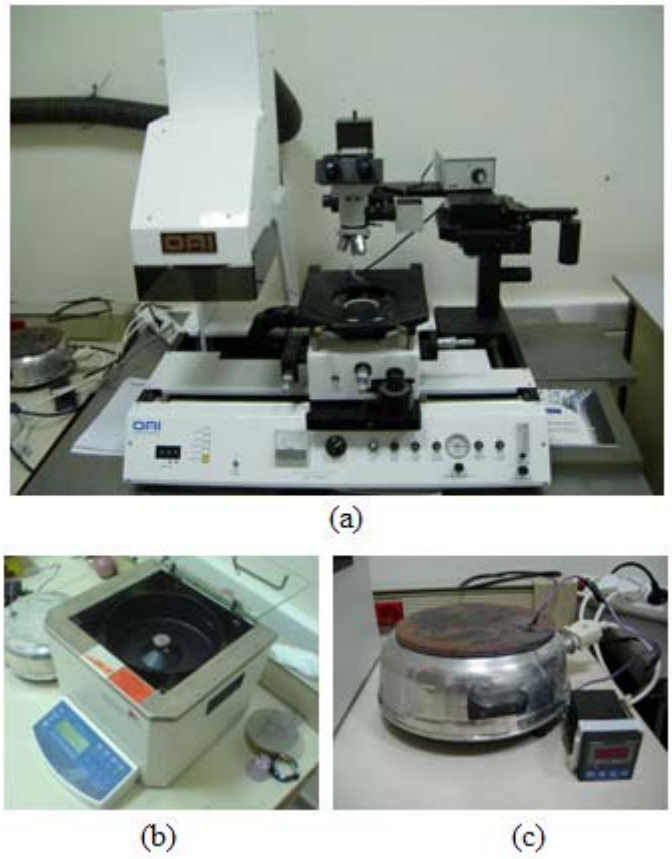

Figure 3.11. (a) Mask aligner system, (b) spin coater and (c) hot plate.

Next step was post baking; we used a hotplate at 120^0C for 50 second. Post baking was performed to evaporate remaining solvent of photoresist and improve the resist-sample adhesion. This step was optional for our work because our sample had been already heated to 120^0C for 2 minutes in reversal baking step.

Up to now, photolithography process is determined. This pattern transfer process was performed to create a photoresist pattern on SiO_x substrate. Sputtering of tantalum on patterned substrate enables us to obtain a desired pattern of Ta. After the photolithography, there would be regions without resist on the sample surface. If the substrate is placed in to the sputtering chamber and Ta is grown on substrate, Ta directly grows on SiO_x only in the regions without resist. In other regions on the substrate, Ta grows on photoresist. To fabricate metal-insulator-metal junctions via AFM oxidation lithography, sputtered metal layer, which is tantalum for our work, should be very thin, approximately between 3-10nm. AFM tip induced oxide can

reaches to the substrate as long as the metallic film thickness is about 3-10nm. For this reason, Ta thin film was sputtered with thickness of ~7 nm on thermally oxidized SiO_x (360nm) substrate in this step.

After the sputtering of tantalum, liftoff process was performed. In this step, the sample was dipped into a stripper (AZ 100 remover from microchemicals) in ultrasonic cleaner for 10 minutes and remaining photoresist was removed from surface. After the sample removed from stripper, it was dipped isopropanol and finally nitrogen was used for drying the sample.

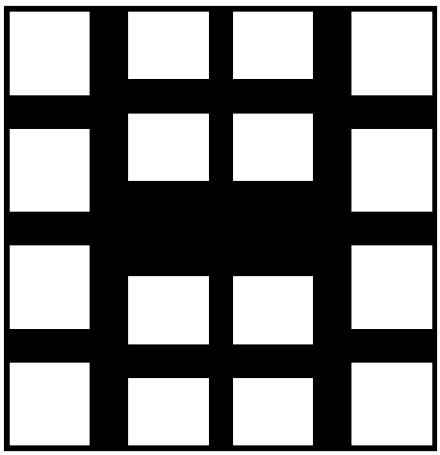

Figure3.12. Mask design used for exposure the positive photoresist.

Just after the patterning of surface, we need a second lithography process to coat a gold layer on contact pads. For this purpose we used a second mask design (see Figure 3.12). In this second process, we used a positive photoresist (AZ 1505). Spin coating was performed at 4000 rpm for 45 second. Soft baking was performed at 90^0C and 50 seconds on a hotplate. After the alignment, the sample was exposed for 3 seconds, development of photoresist was performed with AZ 726 MIF. Dipping the sample into the developer and waiting for ~5 seconds, the photoresist in the exposed area was removed. Then developer remaining on the sample surface was removed in pure water bath. We didn't need a hardbake step for our work because we wanted photoresist to be easily removed from surface after gold coating step. Therefore, after the development step, gold layer with thickness of ~100nm was immediately deposited by thermal

evaporation technique on fresh tantalum surface in order to not lose fresh surface in the course of time. The gold material is not only a good conductor but also protects the tantalum surface from oxidation.

The vacuum thermal evaporation technique seen in Figure 3.13 includes evaporation of the material in filament boat heated by high current source and recondensation of the material with vapor state onto cooler substrate. Deposition and thickness of film on the substrate are controlled by shutter and it also provides good quality thin films which have not contamination coming from other materials in the boat at the starting of evaporation. For the good quality thin film, evaporation was done in vacuum around 10^{-6} Torr. It is not only necessary to avoid reaction between the vapor and atmosphere but also to increase the mean free path of vapor atoms.

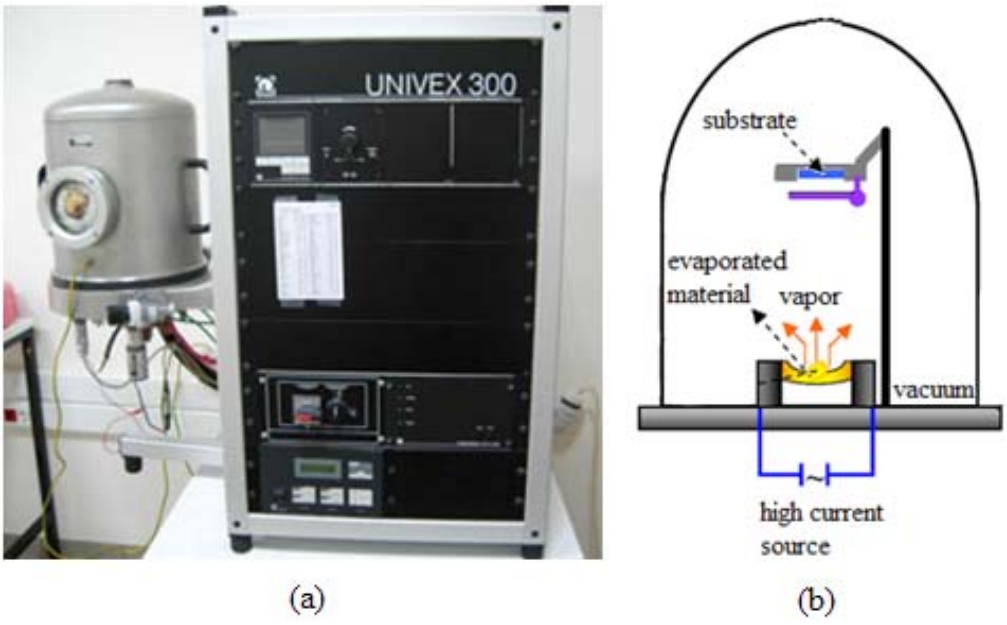

Figure 3.13. (a) Evaporation system and (b) schematic of evaporation.

As a last step, lift-off process was performed. In this step, unexposed photoresist was removed from surface with the gold layer coated on it.

At the end of the processes, desired pattern was created on the SiO_x substrate (see Figure 3.9). Table 3.2 summarizes all parameters used in lithography process.

Table 3.2. Values of parameters used in photolithography process

	Photoresist Type	**Spin speed**	**Softbake time and temperature**	**Exposure time**	**Hardbake time and temperature**	**Development time**	**Removal in ultrasonic cleaner**
1st litho.	Negative	4600 rpm	50 sec 110 ^{0}C	1 sec	2 min 120 ^{0}C	1 min	10 min
2nd litho.	Positive	4600 rpm	50 sec 100 ^{0}C	3 sec	–	~5 sec	5 min

3.3.2. Tantalum Oxide Barrier Formation

In our study, we also demonstrate the capability of AFM to fabricate Metal-Oxide-Metal junctions by oxidizing a thin Ta strip grown on SiO_x substrate. In this method, we performed in-situ electrical measurements during oxide fabrication. Figure 3.14 shows schematic of our experimental setup. After a rather large Ta stripes had been formed by conventional photolithography method, an additional single oxide line was written by sequentially moving the conductive AFM tip across the stripe under a bias voltage. By this way, we can observe the effect of each oxidation step individually.

After the photolithography process, we obtain a desirable configuration of sample. This configuration made us enables to apply voltage to the sample and make a 4 terminal measurement of the resistance of the central line. The resistance of the structure was measured by applying a current I and measuring the voltage V. During the

oxidation, current between tip and sample is much smaller than I; therefore, the resistance of Ta line can be measured during oxidation process.

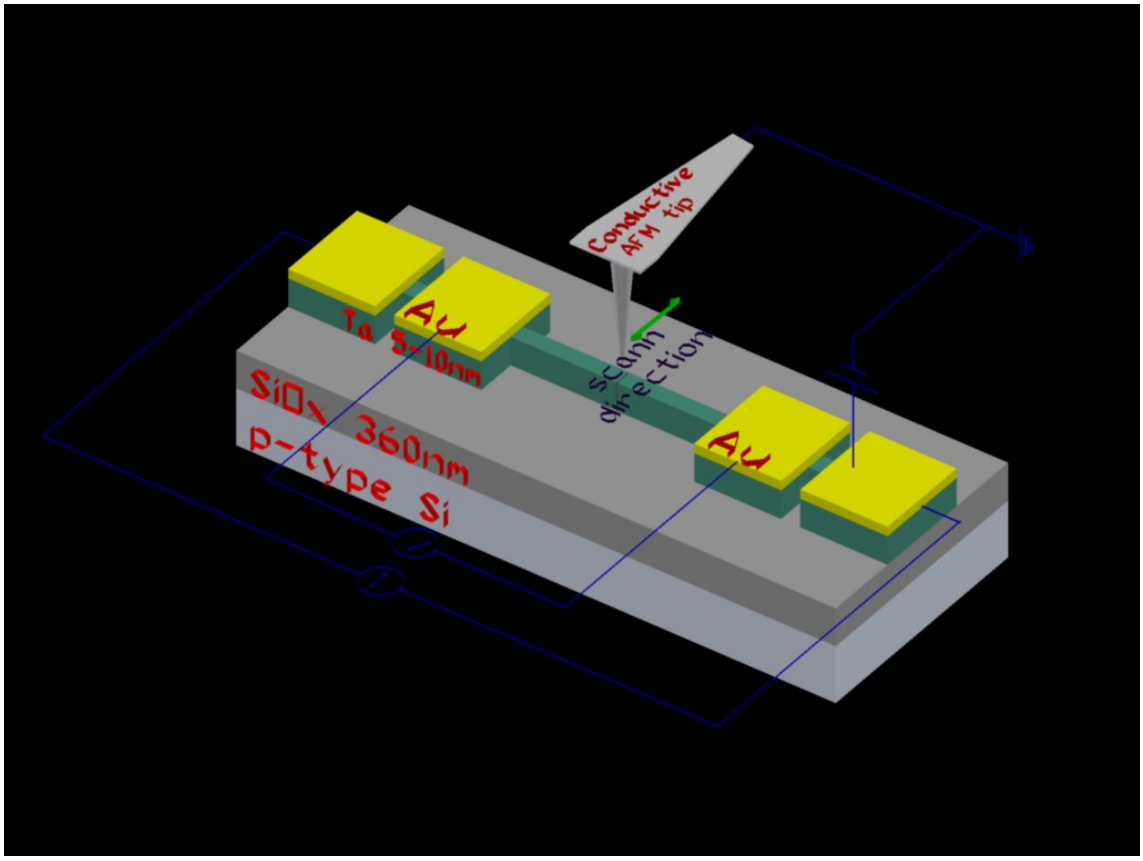

Figure 3.14. Schematic of barrier formation setup.

In order to make electrical characterization, we had modified our sample holder by adding four connectors to the edge of the sample holder. After the wires had been attached to the contact pads of Ta sample, the sample holder mounted on AFM sample holder stage. Wires were sent to the terminals of Keithley 2420 source-meter with a connector. This measuring instrument can sweep a constant current through two terminals while it measures the voltage between two other terminals, or vice versa. Change in resistance during the oxidation was monitored on computer screen via electrical characterization program created with LabView^{TM} software. User interface of software can be seen in Figure 3.15 and Figure 3.16.

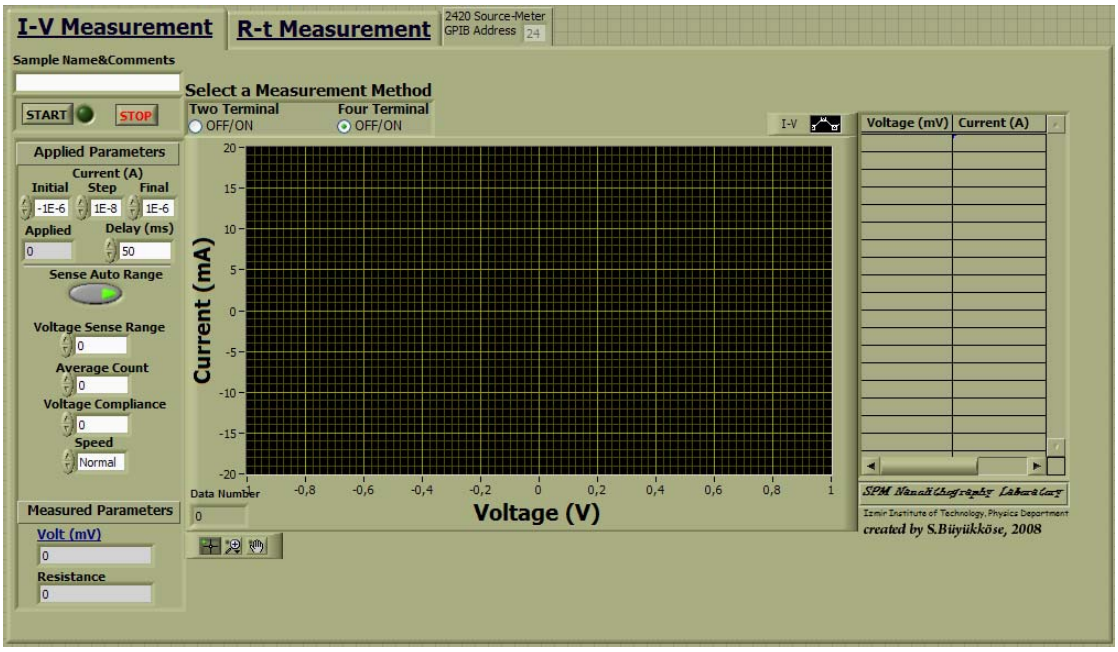

Figure 3.15. Interface of I-V program created with LabView™.

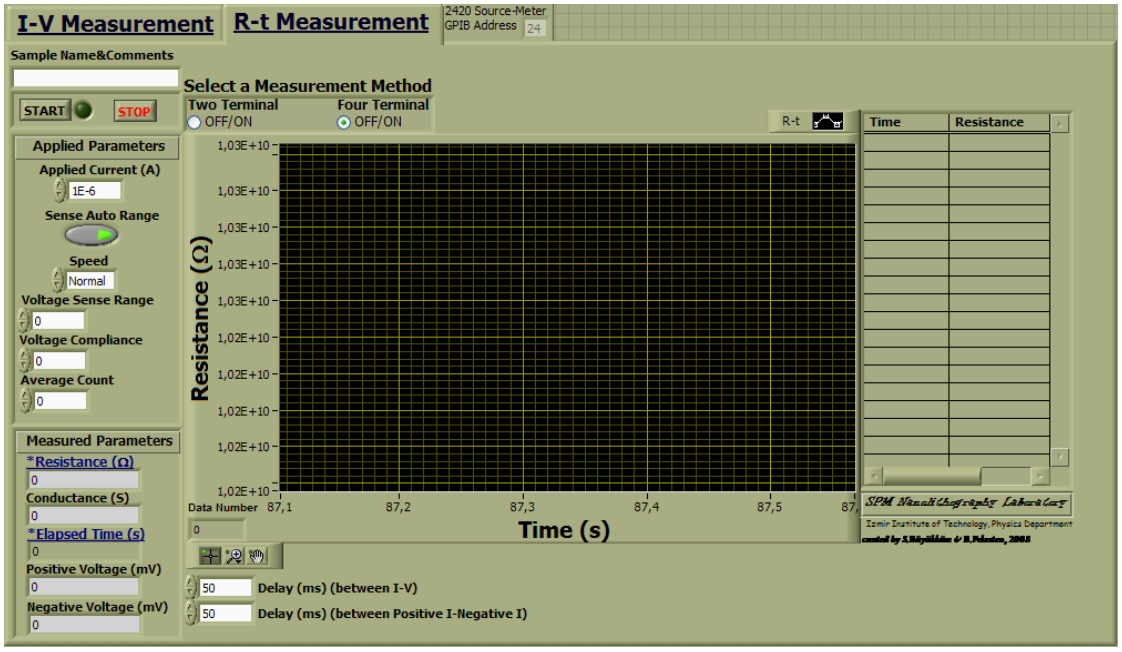

Figure 3.16. Interface of R-t program created with LabView™.

CHAPTER 4

RESULTS AND DISCUSSION

This chapter consists of 5 main parts as structural characterization, dimensional characterization, electrical characterization, comparison of oxidation results and results of junction formation. The first part consists of x-ray diffraction, scanning electron microscopy and atomic force microscopy analyses of metallic thin films. In the second part, the effect of parameters on oxide growth kinetics, such as applied voltage, oxidation time and relative humidity, were discussed in detail. Electrical characterization results of oxide structures were given in the third part. Dimensional comparison of oxide growth results for determination of most candidate material to be used in further applications was presented in fourth part. Finally, in the last part, lateral metal-oxide-metal junction formation was discussed.

4.1. Structural Characterization Results

In structural characterization part, we presented the x-ray diffraction, scanning electron microscopy and atomic force microscopy results of thin films (Ta, Hf and Zr).

4.1.1. X-Ray Diffraction (XRD) Characterization

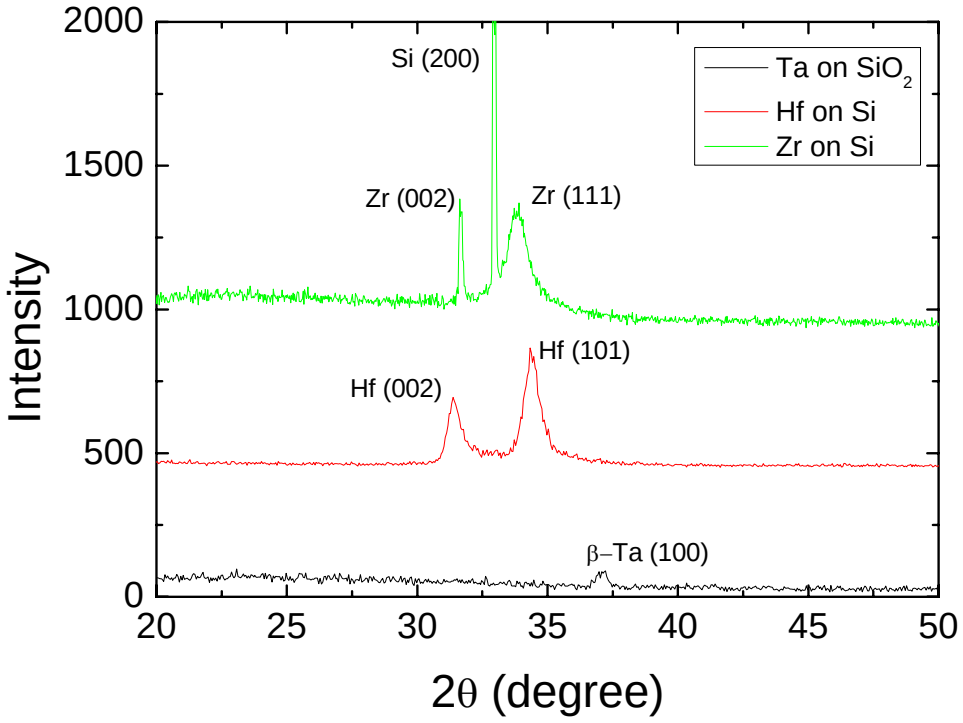

Figure 4.1 XRD patterns of Ta, Hf and Zr thin films.

XRD characterization is one of the common techniques which are used to determine the crystal structure of the thin films. In order to investigate the crystalline quality of our films, XRD characterization was performed. The XRD characterization was performed for the three films fabricated on different substrates. Figure 4.1 shows the XRD patterns of Hf and Zr films grown on Si substrates, and Ta film grown on SiO_2 substrate. According to results, there are two different Zr peaks indicating (002) and (111) orientations. Another peak appears on same pattern belongs to Si (200). There are also two peaks on the pattern for Hf. These peaks show the crystallization in the direction of (002) and (101). For Ta a weak peak appears on the spectra for β-Ta (111) orientation.

4.1.2. Scanning Electron Microscopy (SEM) Characterization

SEM is a powerful tool which can characterize the surface morphology of materials in submicron and micrometer scale with a high resolution. In this work, we have characterized the cross-section of our thin films (Ta, Hf and Zr) in the 500nm resolution. SEM cross-sectional image of Ta on silicon oxide substrate is illustrated in Figure 4.2. Uniform tantalum film layer and continuous deposition can easily be seen from the micrograph. Thickness of the tantalum layer was found as ~20nm for 17 minutes deposition from this micrograph.

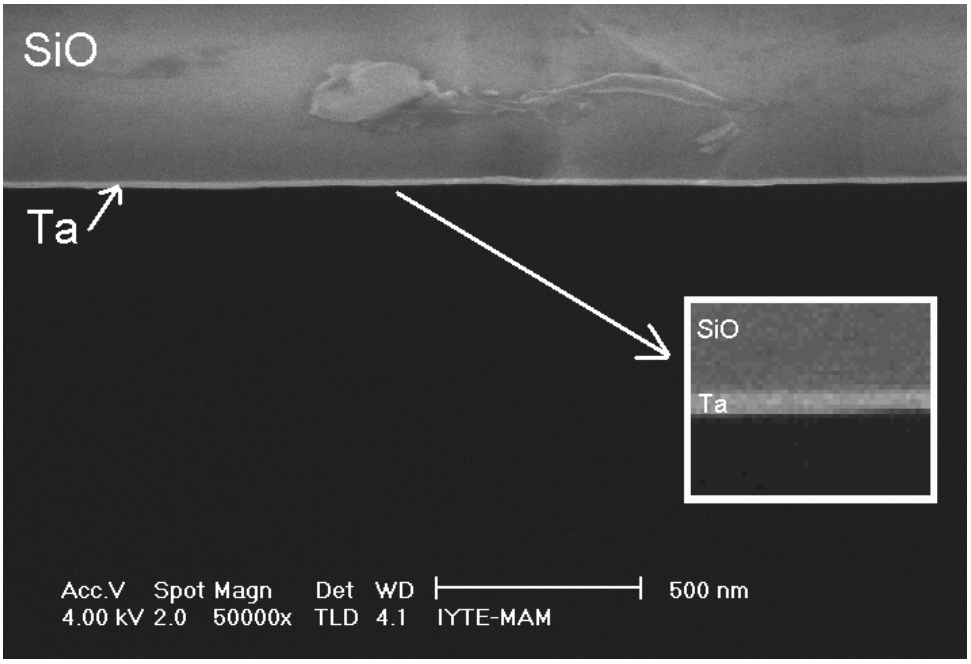

Figure 4.2. Cross-sectional SEM image of Ta thin film.

Figure 4.3 shows cross-section of Hf thin film layer on silicon substrate. There is a uniform and homogeneous film. Thickness of hafnium layer was found to be ~65nm from figure for 25 minutes growth.

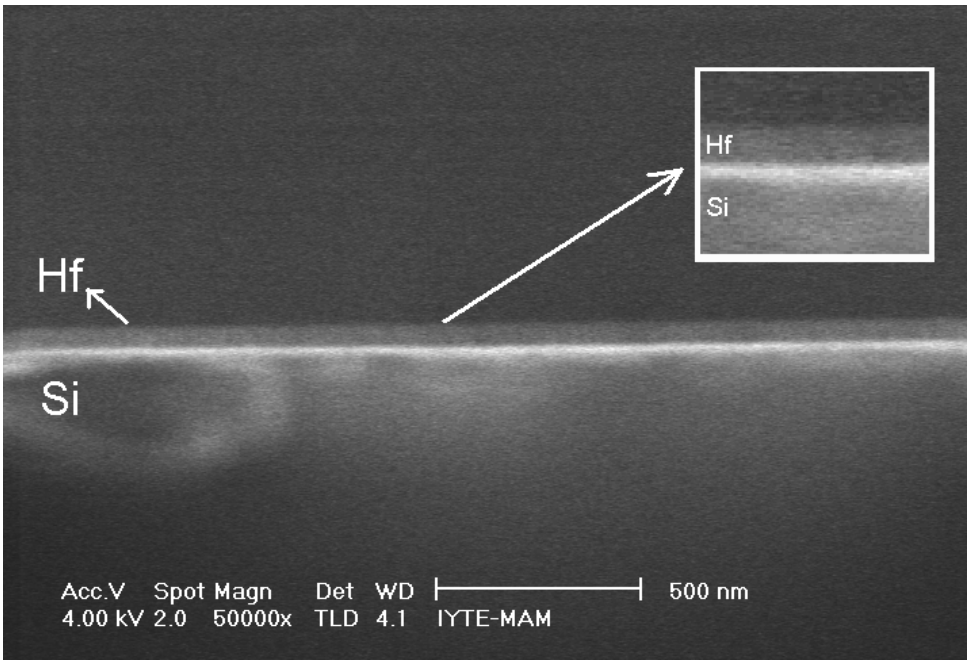

Figure 4.3. Cross-sectional SEM image of Hf thin film.

Figure 4.4 shows the SEM cross-section image of thick Zr thin film layer on silicon substrate. Continuous deposition and uniform zirconium layer can be seen from micrograph. Thickness of the zirconium layer was found ~120nm for 25 minutes deposition from micrograph.

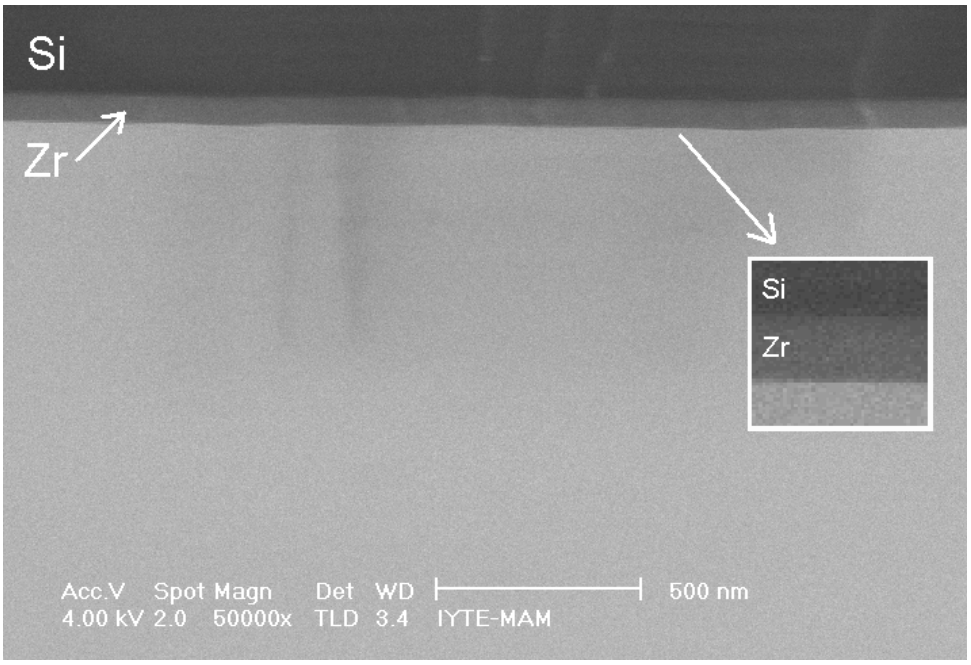

Figure 4.4. Cross-sectional SEM image of Zr thin film.

4.1.3. Atomic Force Microscopy Results for Thin Films

For the investigation of surface morphology of deposited films, two and three dimensional AFM images were recorded. All AFM images for roughness analysis were taken for 5x5μm^2 areas because all oxidation experiments were performed on 5x5μm^2 areas. As mentioned before, roughness is a very important parameter for our samples. To distinguish the created oxide protrusions from surface morphology after AFM imaging process, thin films should have very smooth surface.

Figure 4.5 shows 2D and 3D AFM images of tantalum thin film. As can be seen from picture, Ta has a very smooth surface. For this picture surface roughness (rms) was found as 0,141nm.

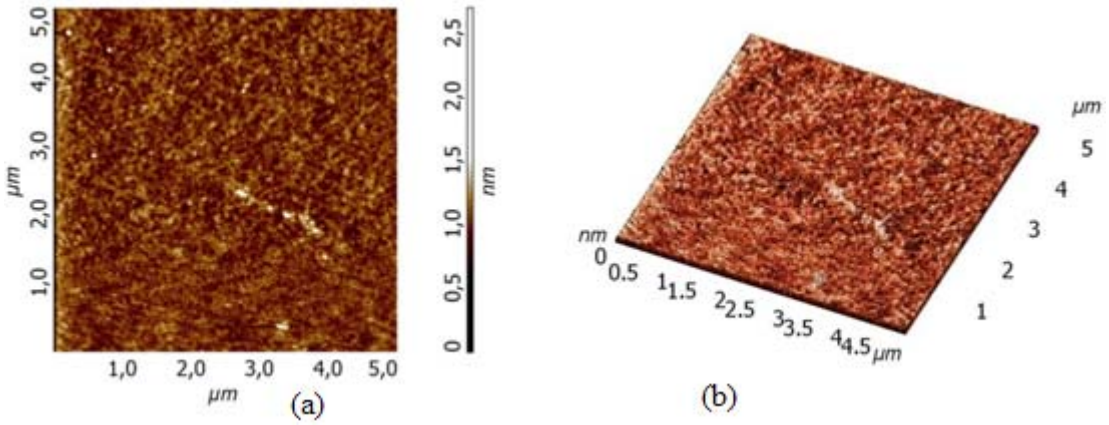

Figure 4.5. (a) 2D and (b) 3D AFM images of tantalum thin film.

Figure 4.6 shows 2D and 3D AFM images of hafnium thin film. As can be seen from picture, Hf has also a very smooth surface. For this picture surface roughness (rms) was found as 0,145nm.

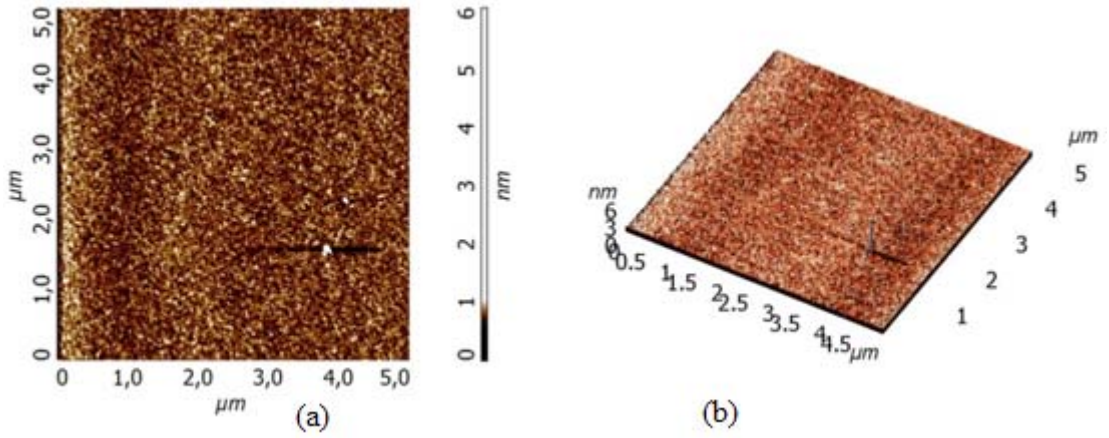

Figure 4.6. (a) 2D and (b) 3D AFM images of hafnium thin film.

Figure 4.7 shows 2D and 3D AFM images of zirconium thin film. As can be seen from picture, Zr has a very smooth surface like Ta and Hf have. For this picture surface roughness (rms) was found as 0,166nm.

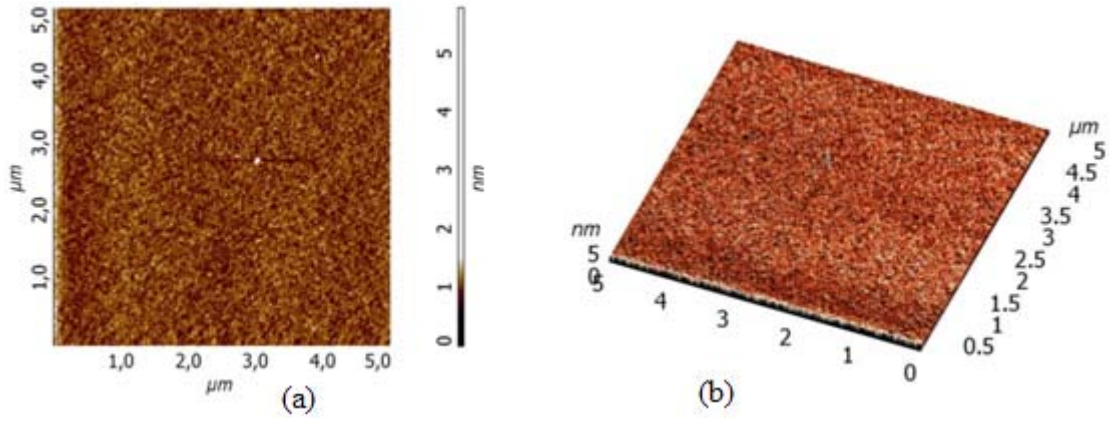

Figure 4.7. (a) 2D and (b) 3D AFM images of zirconium thin film.

Figure 4.8 also shows the surface morphology of SiO_x substrate which was grown thermally. And surface roughness (rms) for thermally oxidized SiO_x film was found as 0,133nm.

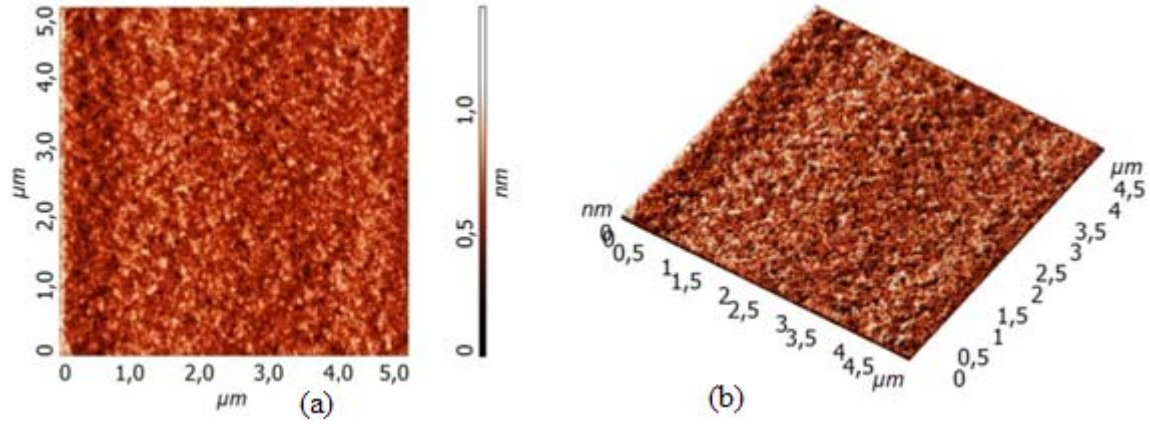

Figure 4.8. (a) 2D and (b) 3D AFM images of SiO_x surface.

The table below summarizes the roughness values for Ta, Hf, Zr and thermally oxidized SiO_x surfaces.

Table 4.1. Roughness values of tantalum, hafnium and zirconium.

	Tantalum	**Hafnium**	**Zirconium**	**SiO_x**
Roughness (rms)	0,141nm	0,145nm	0,166nm	0,133nm

4.2. Dimensional Characterization Results of Oxide Structures

In order to understand the oxidation process, we created TaO_x, HfO_x and ZrO_x lines with DLC coated AFM tip for different applied voltages between sample surface and tip. We have also looked at effect of the voltage on the oxide line-width. Relative humidity and oxidation time have been also studied as other influential parameters on local oxidation process. First the oxidation results at different voltages were discussed. After this, effect of relative humidity and oxidation time will be presented with detailed discussion.

4.2.1. The Effect of Bias Voltage on Structures

The 3D results for the created oxides under ambient conditions can be seen from Figures 4.9, 4.10 and 4.11. Each line on the films was created applying different voltages ranging between 1V and 10V. It can be noted that the oxide patterns for each samples have uniform features and display a clear dependence on the applied bias voltage.

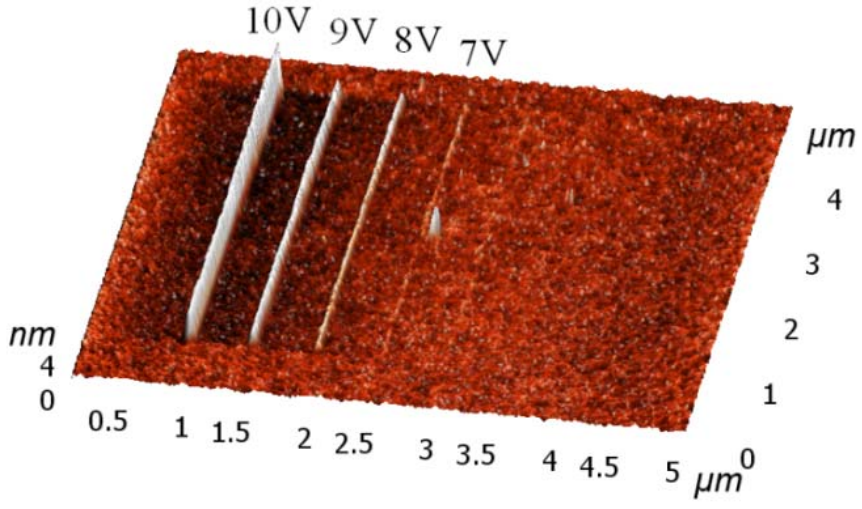

Figure 4.9. 3D AFM image of oxide lines created at ambient conditions on Ta thin film.

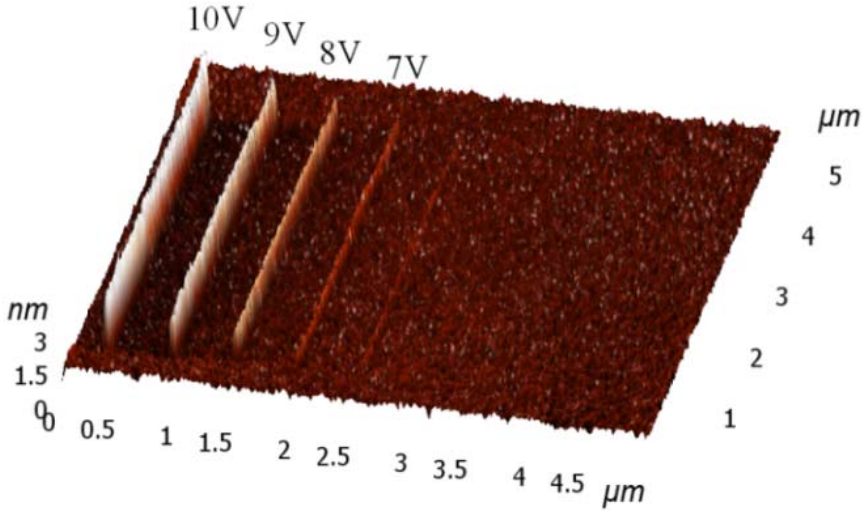

Figure 4.10. 3D AFM image of oxide lines created at ambient conditions on Hf thin film.

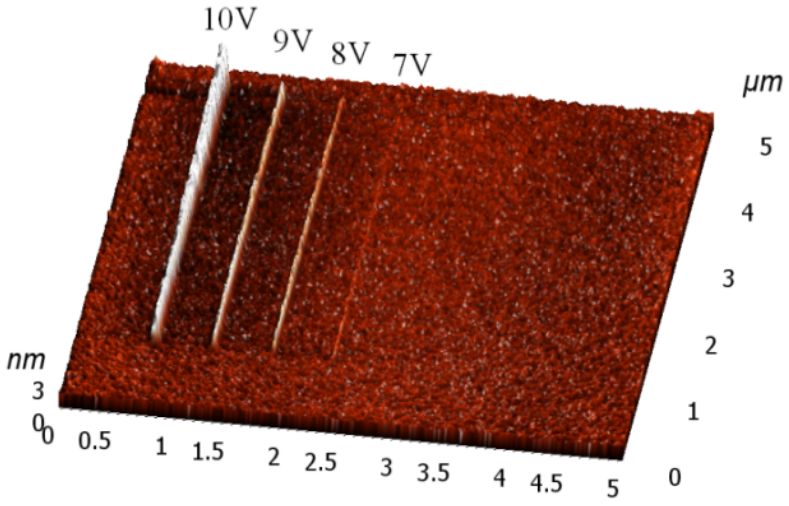

Figure 4.11. 3D AFM image of oxide lines created at ambient conditions on Zr thin film.

Figure 4.12, 4.14 and 4.16 shows the plots of oxide height versus applied voltage for oxides produced at different values of relative humidity and at the 210ms voltage duration on Ta, Hf and Zr, respectively. It is clearly seen from Figure 4.12, 4.14 and 4.16 that there is a linear increase for oxide height with respect to applied bias voltage. Similar linear relationship has already been reported for Si and some other metals by various groups (Ma, et al. 2001, Fang, et al. 2004, Farkas, et al. 2004). The electric field between the conductive AFM tip and metal surface is directly related to the applied voltage and dielectric constant of the protruding oxide. The electric field causes OH^- ions to easily diffuse through the oxide to the metal/metal oxide interface. The increase in the amount of the oxide layer also causes the oxide protrusion width to increase (Figure 4.13, 4.15 and 4.17).

The voltage dependence indicates that the electric field under the tip apex plays an important role in the local oxidation process. Higher bias voltages produce more ions and kinetic energy of these ions is higher than that of ions produced under a lower electric field. The penetration depth of ions into the oxide layer depends on their energy. This means that more ions reach the oxide/metal interface under higher bias voltage. In this way, the oxidized region in the film increases with increasing bias voltage and thus a higher and wider protrusion from the surface is observed.

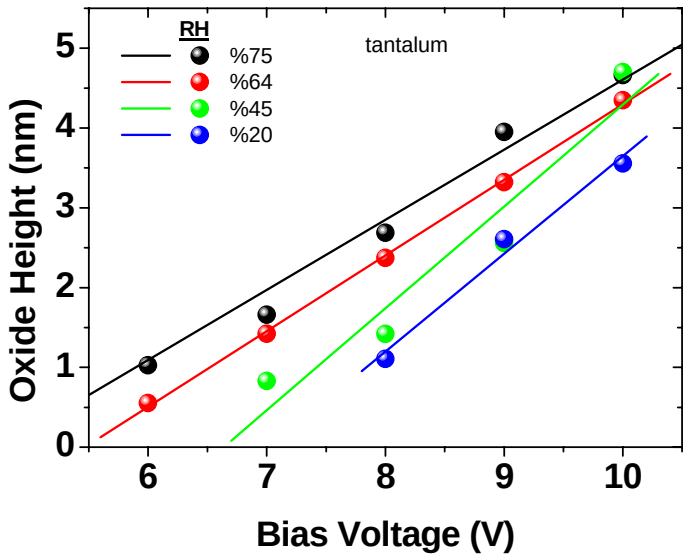

Figure 4.12. Plots of oxide height vs. applied voltage for oxide lines produced on tantalum at different values of relative humidity and at the 210ms voltage duration.

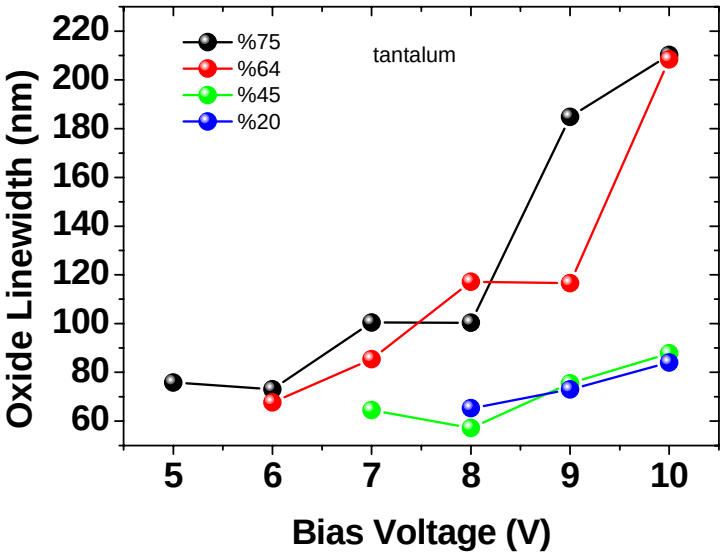

Figure 4.13. Plots of oxide line-width vs. applied voltage for oxide lines produced on tantalum at different values of relative humidity and at the 210ms voltage duration.

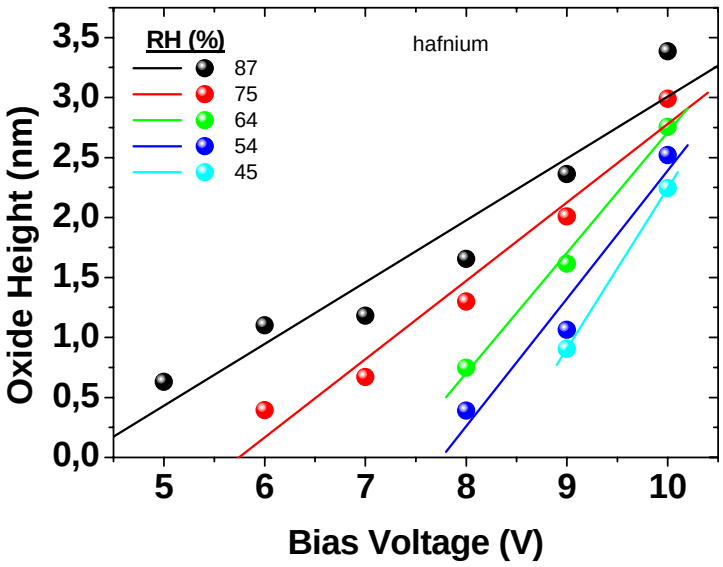

Figure 4.14. Plots of oxide height vs. applied voltage for oxide lines produced on hafnium at different values of humidity and at the 210ms voltage duration.

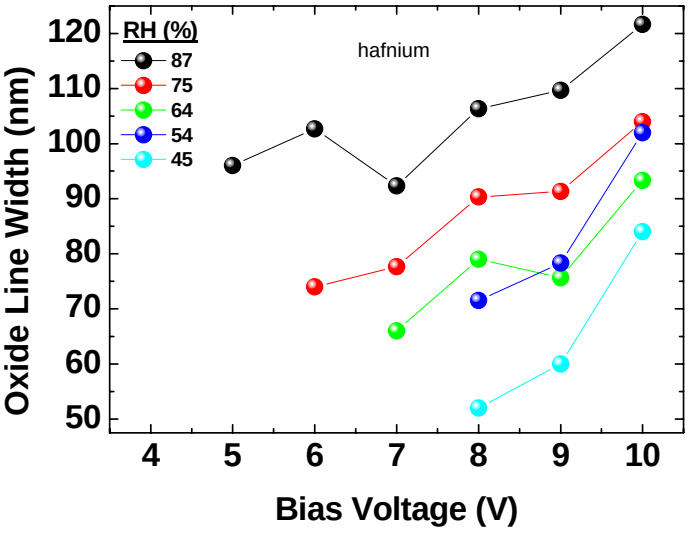

Figure 4.15. Plots of oxide line-width vs. applied voltage for oxide lines produced on hafnium at different values of relative humidity and at the 210ms voltage duration.

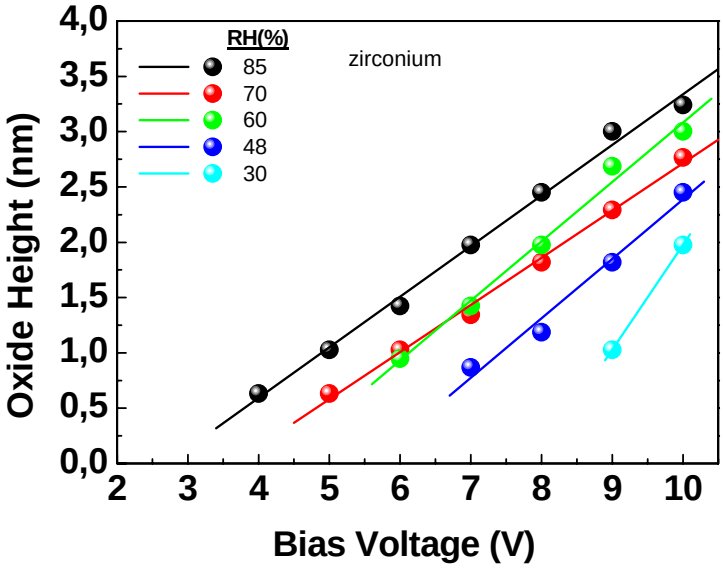

Figure 4.16. Plots of oxide height vs. applied voltage for oxide lines produced on zirconium at different values of relative humidity and at the 210ms voltage duration.

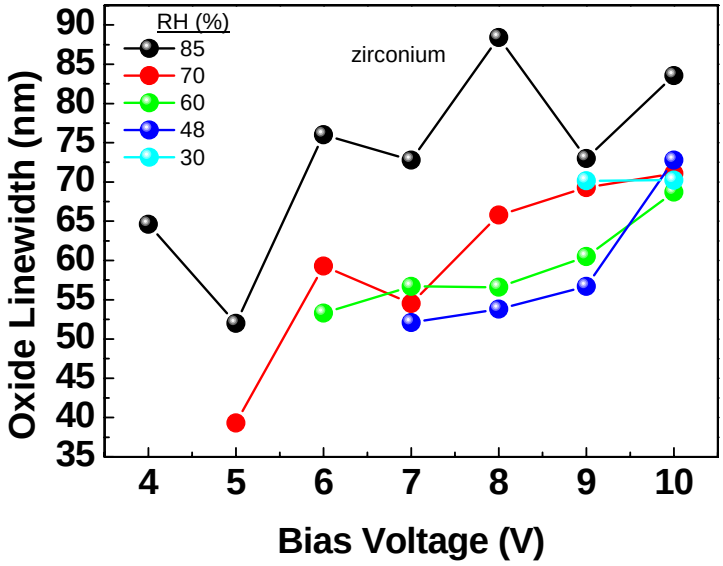

Figure 4.17. Plots of oxide line-width vs. applied voltage for oxide lines produced on zirconium at different values of relative humidity and at the 210ms voltage duration.

Oxide composition of created structures cannot be estimated from existing data. However, some workers suggested oxide forms for Ta. X-ray photoelectron spectroscopy (XPS) results confirmed Ta_2O_5 formation on Ta surface via STM induced oxidation in an electrochemical cell including NaOH solution (Thundat, et al. 1990). Kim et. al also showed that tantalum oxide dots created via AFM induced oxidation method has similar electrical properties with Ta_2O_5 (Kim, et al. 2003). For the determination of oxide composition of our oxide structures further experiments; such as, transmission electron microscopy, RBS, EDS or XPS with high resolution are needed.

4.2.2. The Effect of Relative Humidity on Structures

Relative humidity is another effective parameter as the source of water layer on the metallic thin film. To understand the influence of the relative humidity on oxide height and width, SPL experiments were performed at various values of humidity between 20%-85%. Increasing humidity accelerates the oxide growth. Both height and line-width of the resulting oxide lines depend on the amount of relative humidity due to the existing water film (see Figure 4.18, 4.19 and 4.20). Extrapolating the data from Figures 4.12, 4.14 and 4.16, it can be concluded that the oxidation process starts when the sample bias voltage values are at a certain value. The Figure 4.21, 4.22, 4.23 show the plots of the threshold voltages at various values of relative humidity for tantalum, hafnium and zirconium, respectively.

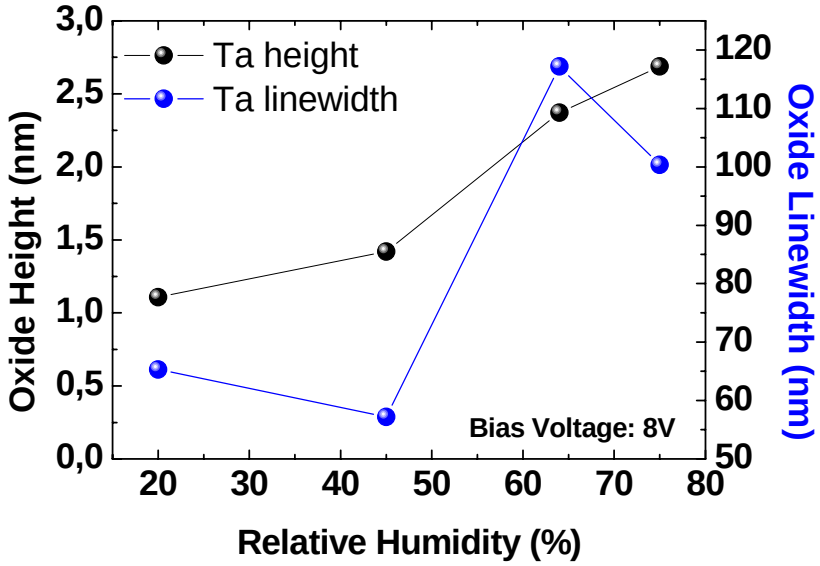

Figure 4.18. Oxide height and line-width versus relative humidity for tantalum.

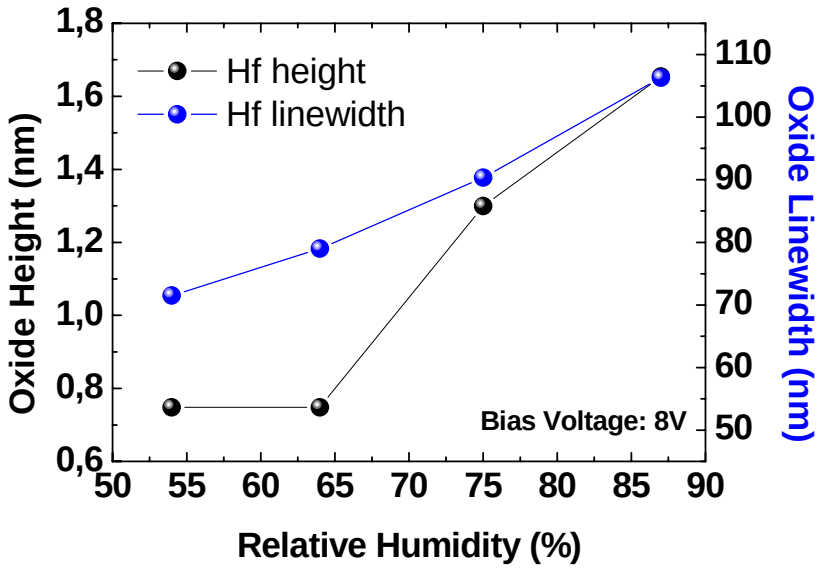

Figure 4.19. Oxide height and line-width versus relative humidity for hafnium.

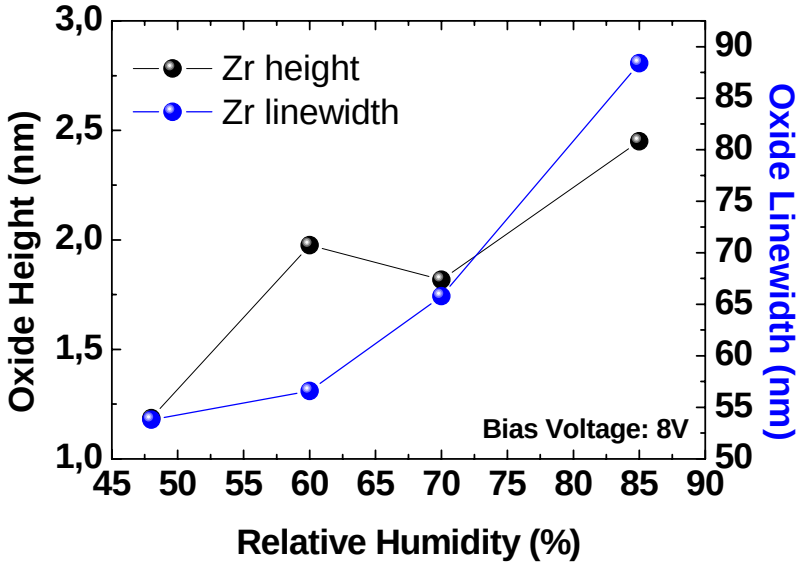

Figure 4.20. Oxide height and line-width versus relative humidity for zirconium.

It is clearly seen that the threshold voltage for oxide formation decreases with increasing humidity. The threshold voltage, oxide height and protrusion width dependence on oxide structures can be explained by taking account the number of water molecules between tip and sample surface. At low relative humidity there are not enough water molecules to provide the oxyanions for oxidation reaction to proceed. Therefore, the threshold voltage starting the oxidation reaction will decrease with increasing relative humidity. During the oxidation process, the AFM feedback system was also activated to keep the distance between tip and surface constant; therefore, when the oxide layer starts to protrude, the AFM tip moves upward in order the keep the distance constant. This makes the water bridge narrower, decreasing the number of ions, and the bridge will also be destroyed in shorter time at low relative humidity. However, in case of higher relative humidity, the number of created ions in the water bridge will increase and the water bridge will also exist for a longer time. Increases in relative humidity also results in a large contact area between the tip and water, resulting in formation of a large bridge. Because the movement of ions is restricted by the boundary of water (see Figure 2.8), ions can be spread across the surface to increase the protrusion width of oxide as a function of increasing relative humidity as shown in Figure 4.18, 4.19 and 4.20.

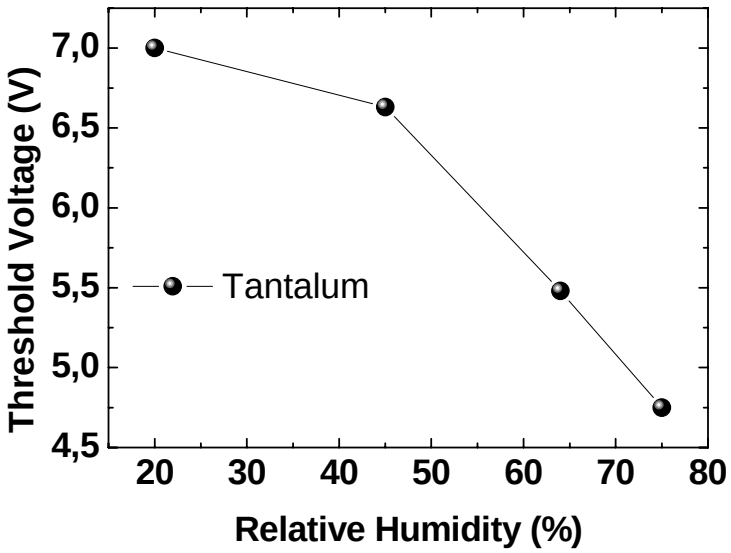

Figure 4.21. Plot of the relative humidity vs. threshold voltages for tantalum.

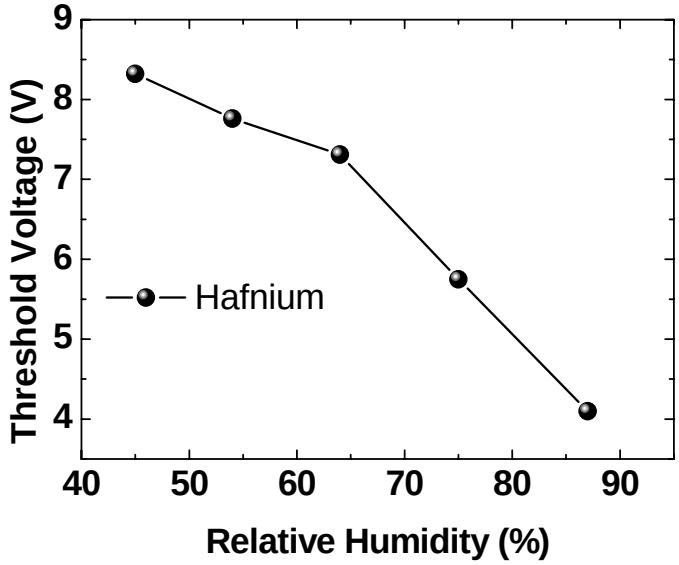

Figure 4.22. Plot of the relative humidity vs. threshold voltages for hafnium.

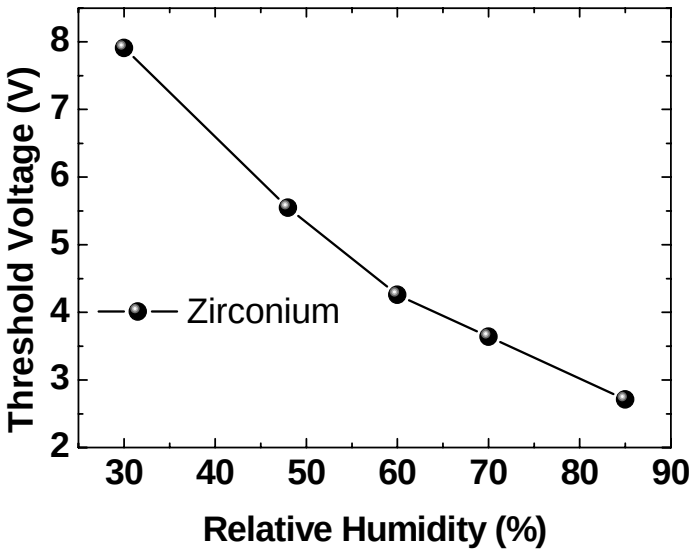

Figure 4.23. Plot of the relative humidity vs. threshold voltages for zirconium.

4.2.3. The Effect of Oxidation Time on Structures

Figure 4.24, 4.25 and 4.26 show 3D AFM images of the oxide lines fabricated on Ta, Hf and Zr surfaces under the same applied voltage to investigate the role of voltage time during the oxidation process. It shows that the uniform oxide features are created under ambient conditions. These 3D pictures reveal that there is a variation in oxide height as a function of bias voltage duration between 2ms and 210ms.

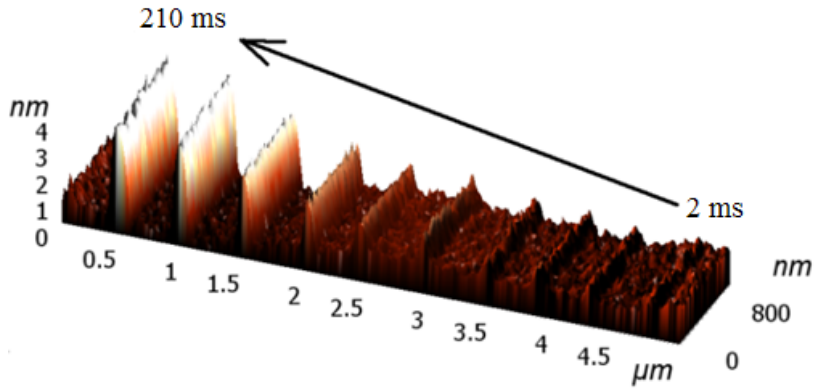

Figure 4.24. 3D AFM image of oxide lines created on tantalum surface with different oxidation times ranging from 2ms to 210ms.

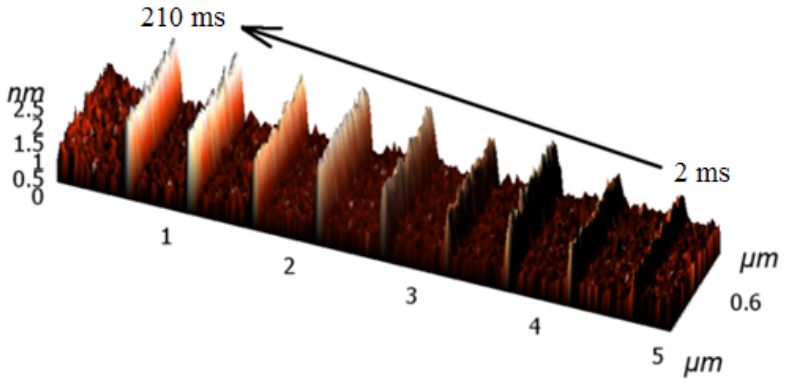

Figure 4.25. 3D AFM image of oxide lines created on hafnium surface with different oxidation times ranging from 2ms to 210ms.

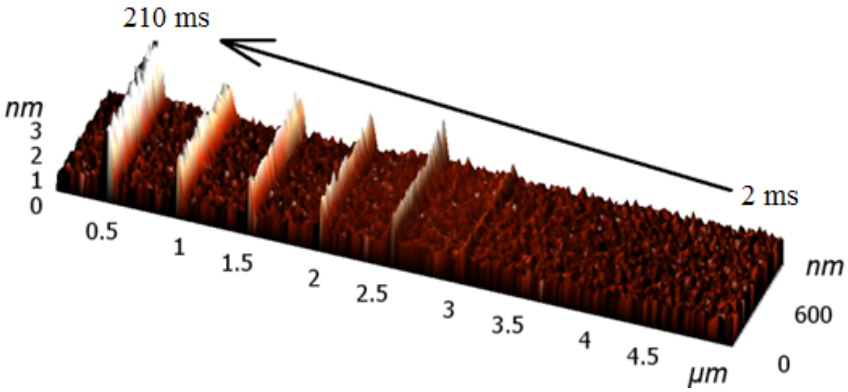

Figure 4.26. 3D AFM image of oxide lines created on zirconium surface with different oxidation times ranging from 2ms to 210ms.

Several phenomenological models, such as the empirical power law (Teuschler, et al. 1995, Dagata, et al. 2000), the logarithmic function of applied voltage duration (Avouris, et al. 1997), and the inverse exponential growth function (Ma, et al. 2001, Lu, et al. 2007) have been reported to predict the oxide height as a function of time and bias voltage using the potential distribution on the oxide layer. Our study shows that SPL grown TaO_x, HfO_x and ZrO_x experimental results were best fitted to the inverse exponential growth (IEG) model, which defines the oxide height with the following equations;

$$\frac{dh}{dt} = \left(\frac{h_0}{\tau}\right) e^{-\frac{t}{\tau}} \tag{4.1}$$

$$h = h_m - h_0 e^{-t/\tau} \tag{4.2}$$

where "h" and "t" represent the oxide height and pulse duration for the applied voltage, respectively. The "h_m" and "h_0" are the initial constants while "τ" is the time constant from the curve fit. Figure 4.27, 4.28 and 4.29 show the plots drawn for TaO_x, HfO_x and ZrO_x formation under voltage of 10V and ambient conditions.

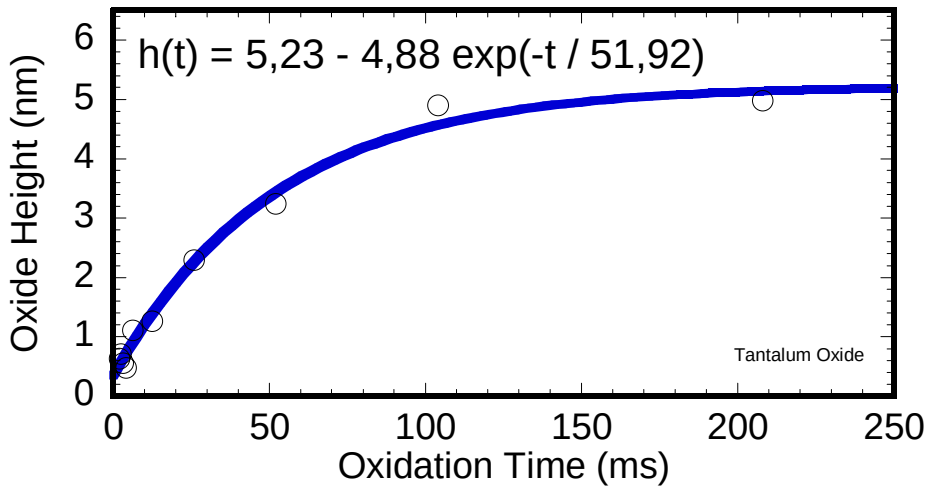

Figure 4.27. Variation of oxide height with oxidation time for tantalum.

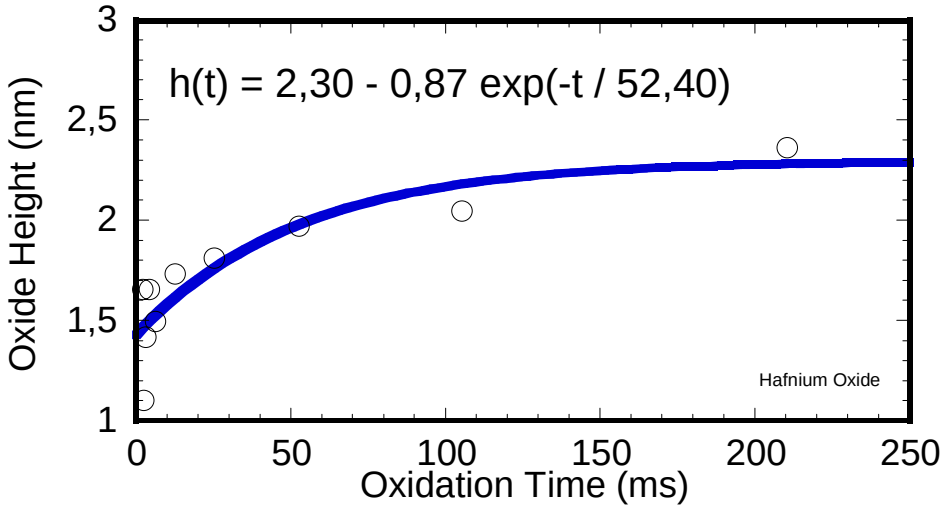

Figure 4.28. Variation of oxide height with oxidation time for hafnium.

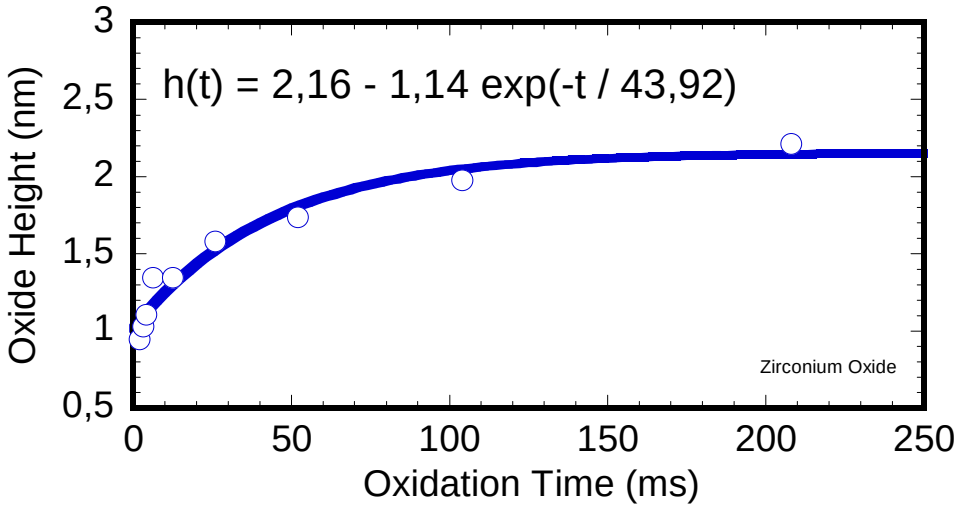

Figure 4.29. Variation of oxide height with oxidation time for zirconium.

For our samples, the best fit parameters calculated from IEG function is summarized in Table 4.2.

Table 4.2. Fit parameters calculated from IEG function for Ta, Hf and Zr.

	h_m (nm)	h_0 (nm)	τ (ms)
Tantalum Oxide	5,23	4,88	51,92
Hafnium Oxide	2,30	0,87	52,40
Zirconium Oxide	2,16	1,14	43,92

The oxidation process is faster at the beginning (at time constant "τ" for each sample), because there is only water layer on the surface as a dielectric barrier. The oxidation rate reaches a plateau around h_m (which is 5,23-2,3-2,16nm for TaO_x, HfO_x and ZrO_x, respectively) due to Metal-Oxide underneath the tip. Since the molecular

volume of the Metal-Oxide layer is larger than that of Metal itself (Table 4.3), the expansion of oxide volume causes stress along the growth direction in a limited local space at the Metal/MetalOxide interface, thus pushing the metal oxide layer upward to form a protrusion. Since the higher oxide protrusion lowers the electric field between the tip and surface, resulting in a decrease in oxide growth rate due to an accumulation of dielectric material and ionic space charges trapped near the substrate/oxide interface (Teuschler, et al. 1995, Dagata, et al. 2000).

Table 4.3. Density values of Ta, Hf and Zr and their oxide forms.

	Density ($g.cm^{-3}$)	**$\rho_M/\rho_{MO}=V_{MO}/V_M$**
Ta	16,69	2,035
Ta_2O_5	8,200	
Zr	6,520	1.147
ZrO_2	5,680	
Hf	12,00	1.239
HfO_2	9,680	

4.3. Electrical Characterization Results of Oxide Structures

To investigate the electrical characteristics of oxide structures, I-V characteristics, spreading resistance measurements (SRM) and electric force microscopy (EFM) methods were performed.

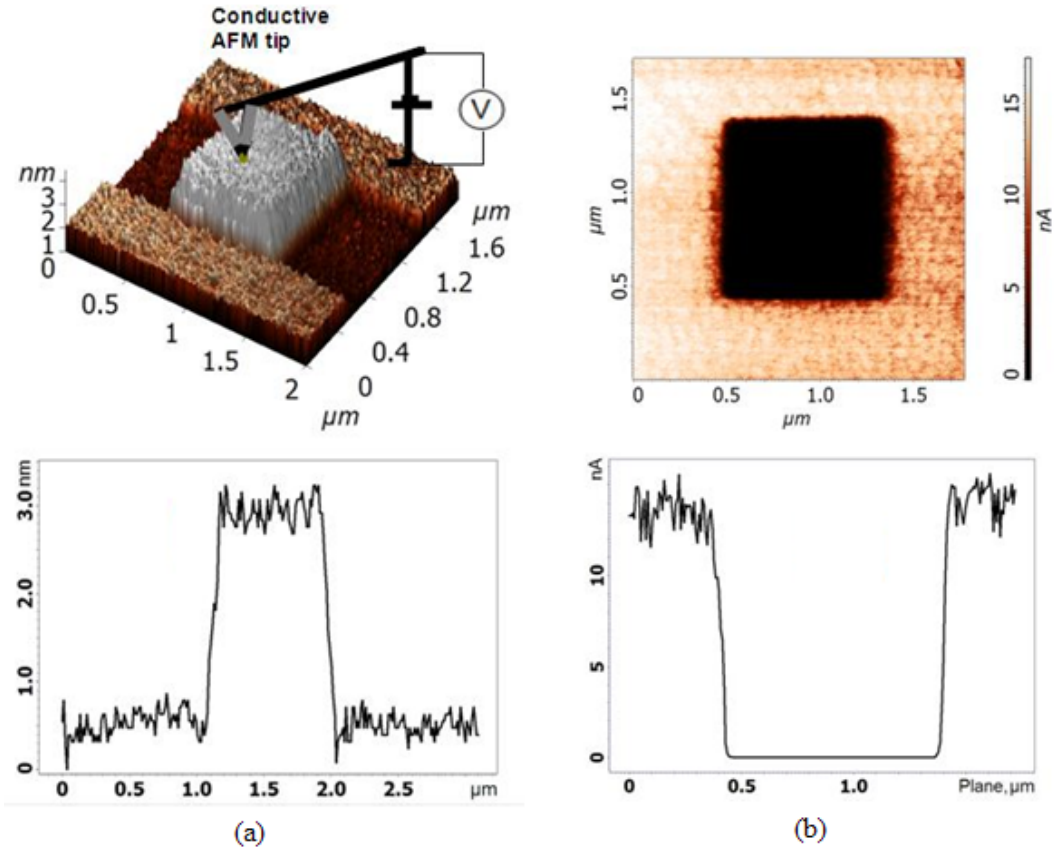

Figure 4.30. (a) The 3D surface topography and (b) the spreading surface resistance image (SRI) of the TaOx layer on this Ta film (Source: Okur, et al. 2008).

For electrical characterization of tip induced TaO_x structure, a $1x1\mu m^2$ TaO_x layer with oxide height of 2.3nm was formed on the Ta film to measure the electrical properties of TaO_x. The 3D surface topography and the spreading surface resistance image (SRI) of the TaO_x layer on this Ta film are shown in Figure 4.30.a and Figure 4.30.b respectively. Two terminal electrical measurements were done in contact mode allowing the AFM tip to touch the oxide layer or Ta surface. The distance between the conductive tip and counter electrode was kept at 5mm. Around 15nA current difference as the contrast of SR image between Ta and TaO_x surface is seen in Figure 4.30.b. Darker contrast shows higher resistive areas on the picture. This means that the TaO_x dielectric material should have more resistance compare to Ta surface.

To measure and compare the resistance of the TaO_x layer and Ta film (inlet), I-V curves have been taken with same DLC coated conductive AFM tip as shown in Figure 4.31. Resistances obtained from I-V curves were $3x10^{12}\Omega$ and $5x10^{5}\Omega$ for the bare TaO_x

layer and the Ta film for linear regions, respectively. The corresponding resistivity was calculated from $\rho=RA/l$, where R is the resistance, A is the cross-sectional area of the tip apex (75nm) and l (2.3nm) is the height of the oxide protrusion. The resistivity of TaO_x layer was measured as $5.76x10^8$ohm-cm. This resistivity of the TaO_x layer is low compared to the resistivity ($4.8x10^{13}$ohm-cm) of a 10nm thick Ta_2O_5 film obtained by dry O_3 annealing at 450^0C as measured by the Moon's group (Moon, et al. 1999). This may be due to possible leakage (tunneling) currents caused from defects and charge traps through the 2.3nm thin tantalum oxide. More detailed studies such as EDS, XPS and capacitance measurements are needed to characterize structural and electronic properties of oxides produced with tip induced SPL technique.

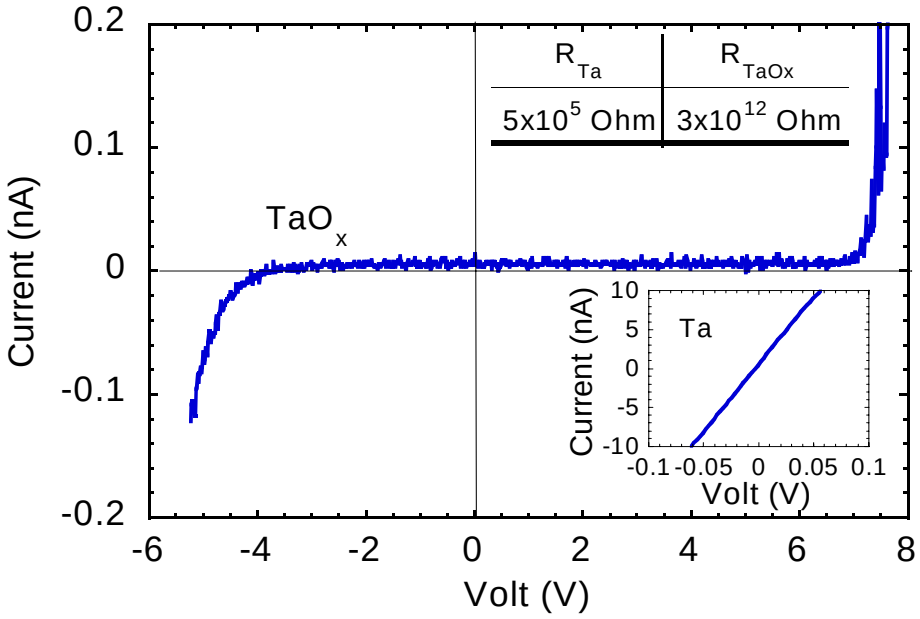

Figure 4.31. I-V curves of TaO_x and Ta (inlet) taken with same DLC coated conductive AFM tip (Source: Okur et al. 2008).

To investigate the electrical characteristics of HfO_x structures, an oxide pattern having a surface area of 1.42μm x 1.26μm and height of 3.3nm was formed on Hf thin film which had been deposited on thermally oxidized SiO_x layer.

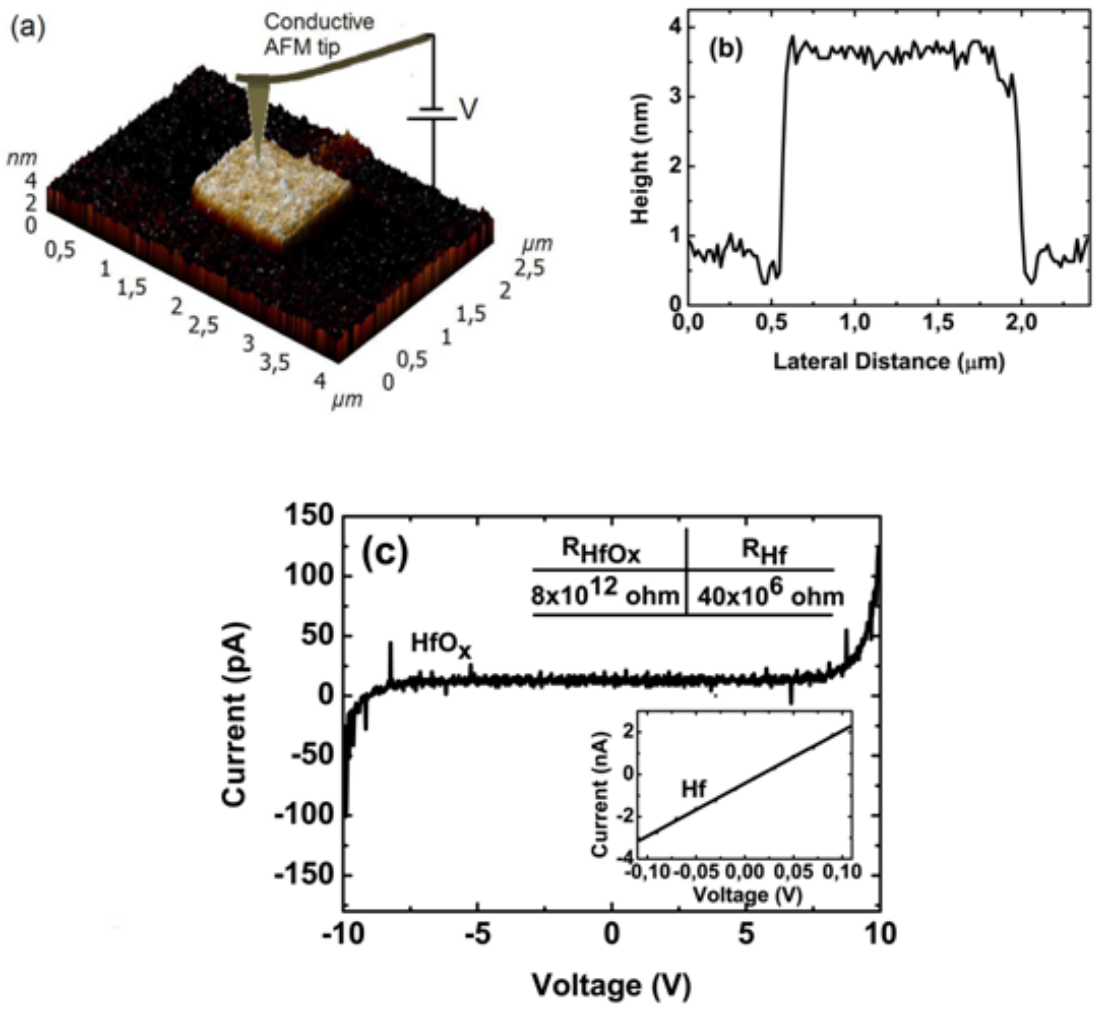

Figure 4.32. (a) The 3D surface topography, (b) height profile and (c) I-V curve of HfO_x and Hf (inlet) taken with same DLC coated conductive AFM tip (Source: Buyukkose, et al. 2009).

The 3D surface topography and height profile of this pattern can be seen in Figures 4.32.a and 4.32.b. To obtain the current voltage characteristics of protrusion of HfO_x and Hf film, the DLC coated conductive AFM tip was allowed to touch the HfO_x or Hf surface in contact mode as shown in Figure 4.32.a and two terminal electrical measurements were performed. The distance between the conductive tip and counter electrode was kept at 5 mm. From the I-V curves for the HfO_x and Hf film, resistances of $8x10^{12}$ohm and $40x10^{6}$ohm were obtained, respectively, with in their linear regions (Figure 4.32.c). Corresponding resistivity of HfO_x was found as $4.284x10^{9}$ohm-cm

which is in agreement with the value reported for sputtered HfO_2 films in literature (Huber 1971).

Figure 4.33.a and 4.33.b show the 2D AFM topography and EFM images of a sample with area of 1.412μm x 1.275μm and with height of 3.162nm. To obtain an EFM image, we used the second pass technique in semi-contact (tapping) mode. In this technique, the surface topography is determined during the first pass in semi-contact operation and than during the second pass, the tip is lifted above the initial position at a constant height (10nm for our study) by applying a DC bias voltage (3V for our study). Following the trajectory of the tip obtained during first pass, we obtained the electric field gradient in the z-direction on the surface. In Figure 4.33.b, darker regions correspond to more electrically resistive regions while brighter regions correspond to more conductive regions. Figures 4.33.a and 4.33.b prove that an electrochemical surface modification has been achieved by oxidizing locally defined regions on the Hf surface.

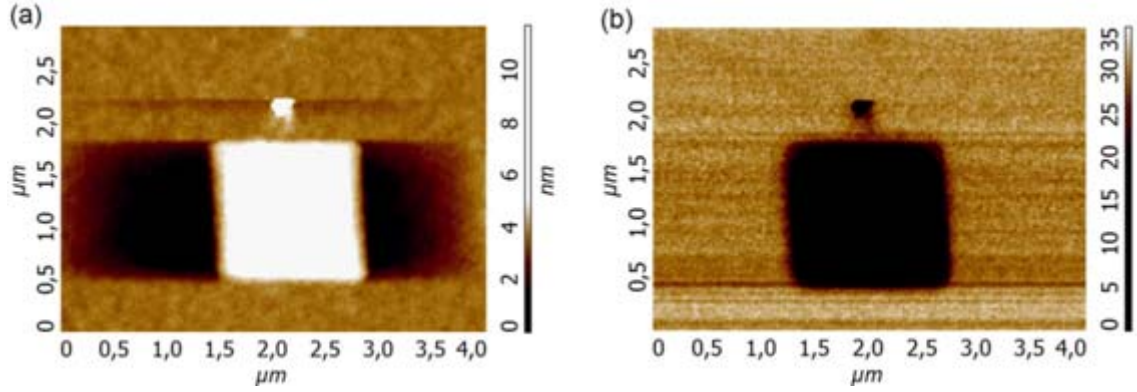

Figure 4.33. 2D AFM topography and EFM images of HfO_x structure with area of 1.412 μm x 1.275 μm and with height of 3.162nm (Source: Buyukkose, et al. 2009).

Topography of the oxide protrusions, their corresponding 2D spreading surface resistance (SR) image (in contact mode), and 1D SR profile are shown in Figures 4.34.a, 4.34.b and 4.34.c, respectively.

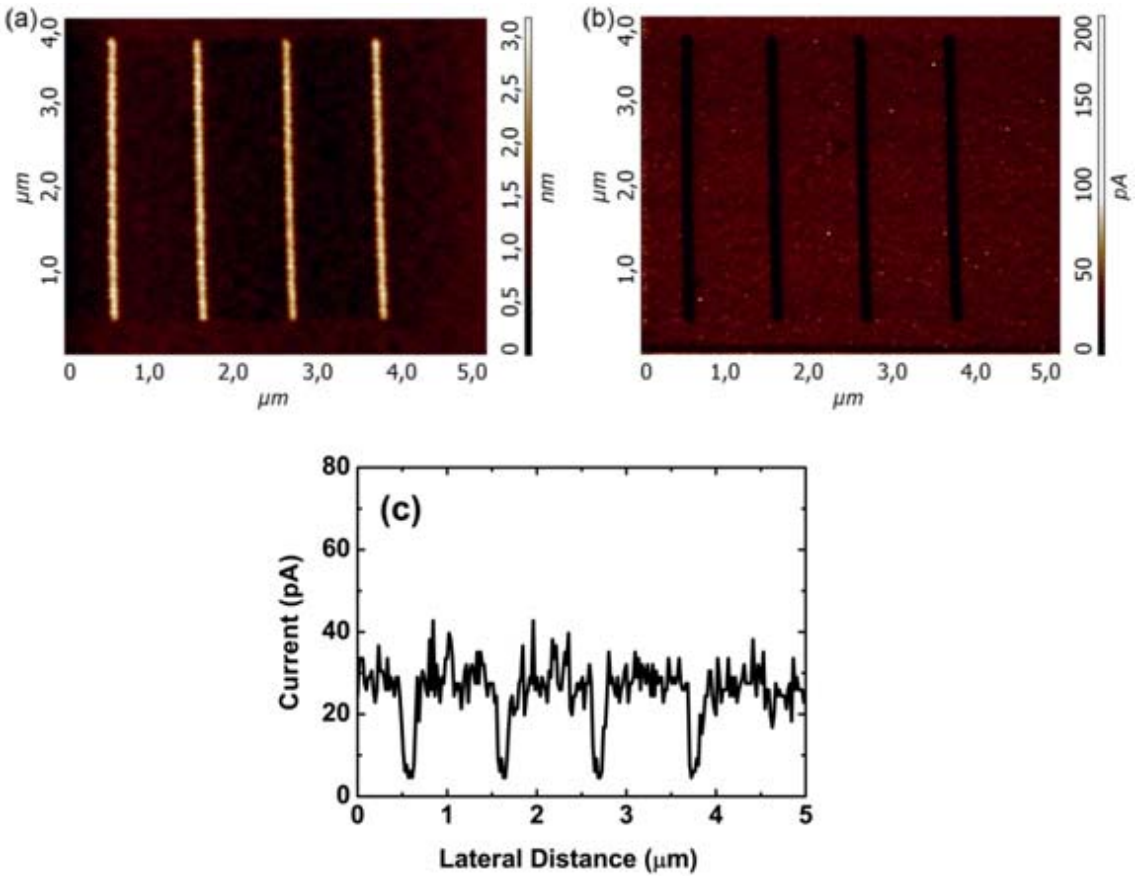

Figure 4.34. (a) Topography of the HfO_x protrusions, (b) their corresponding 2D spreading surface resistance (SR) image (in contact mode), and (c)1D SR profile (Source: Buyukkose, et al. 2009).

In spreading resistance method, a bias voltage is applied to the conductive AFM tip (3V for our study) and a current passes through the surface during scan, yielding information about the resistance of surface. For Figure 4.34.b, areas of darker contrast represent areas of higher resistance on the surface. This means that the HfO_x surface should much more resistive than the Hf surface. A difference of 25pA was found to exist between the surface of the Hf film and protruded HfO_x surface (see Figure 4.34.c). In addition to the EFM image (Figure 4.33.b), the SR image of the surface also confirms that the surface of Hf was successfully oxidized.

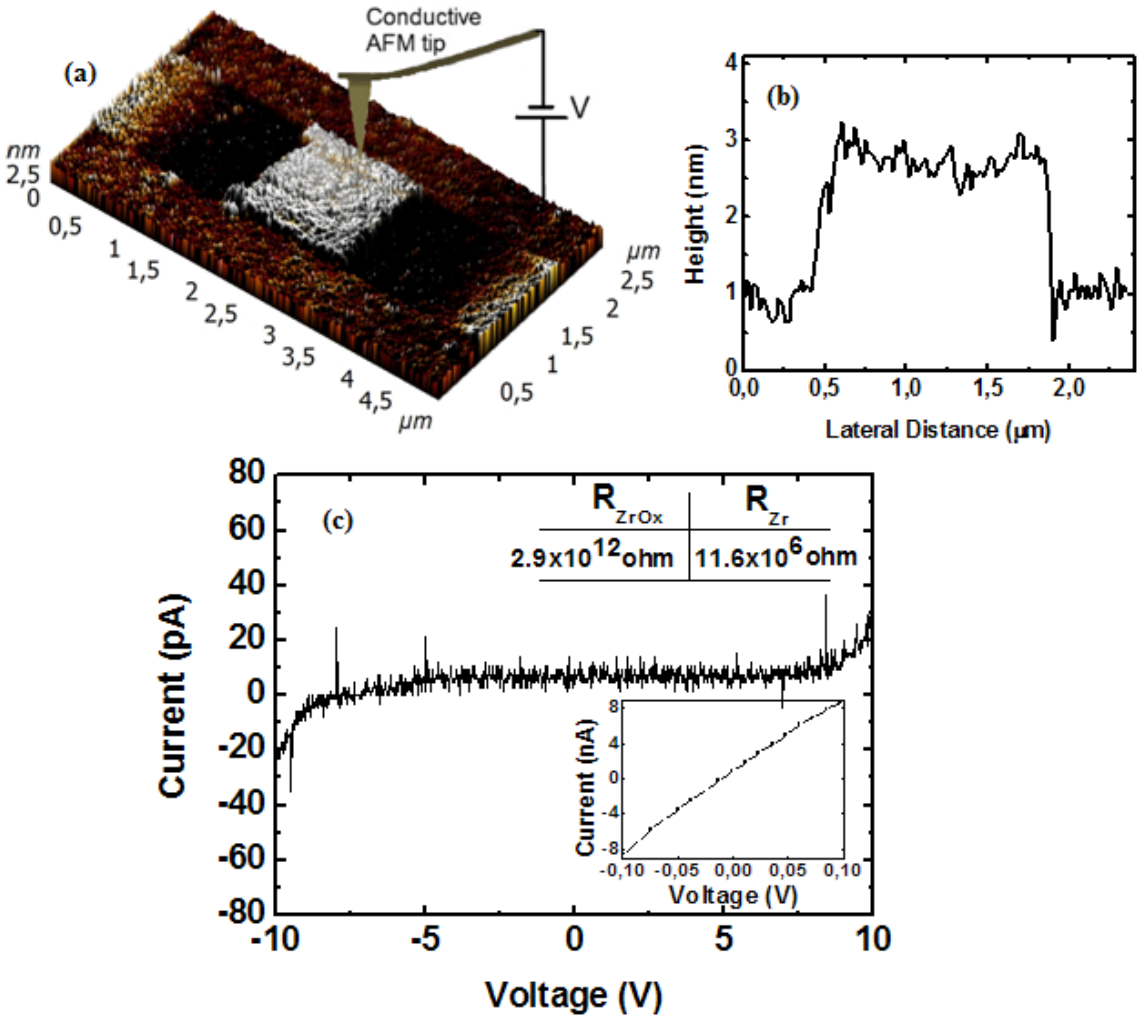

Figure 4.35. (a) The 3D surface topography, (b) height profile and (c) I-V curve of ZrO_x and Zr (inlet) taken with same DLC coated conductive AFM tip.

For electrical characterization of ZrO_x structures, an oxide pattern having a surface area of 1.53μm x 1.39μm and height of 2.2nm was formed on Zr thin film which had been deposited on thermally oxidized SiO_x layer. The 3D surface topography and height profile of this pattern can be seen in Figures 4.35.a and 4.35.b. The current voltage characteristic was achieved with same method employed for TaO_x and HfO_x. From the I-V curves for the ZrO_x and Zr films, resistances of $2{,}93x10^{12}$ ohm and $11.6x10^6$ ohm were obtained, respectively, with in their linear regions (Figure 4.35.c). Corresponding resistivity of ZrO_x was found as $5.9x10^8$ohm-cm. This resistivity of the ZrO_x layer is low compared to the resistivity ($6.25x10^{15}$ohm-cm) of a 475nm thick ZrO_2 film obtained via CVD technique by the Cassir (Cassir, et al. 2002). This may be due to

possible leakage (tunneling) currents caused from defects and charge traps through the 2.2nm thin zirconium oxide.

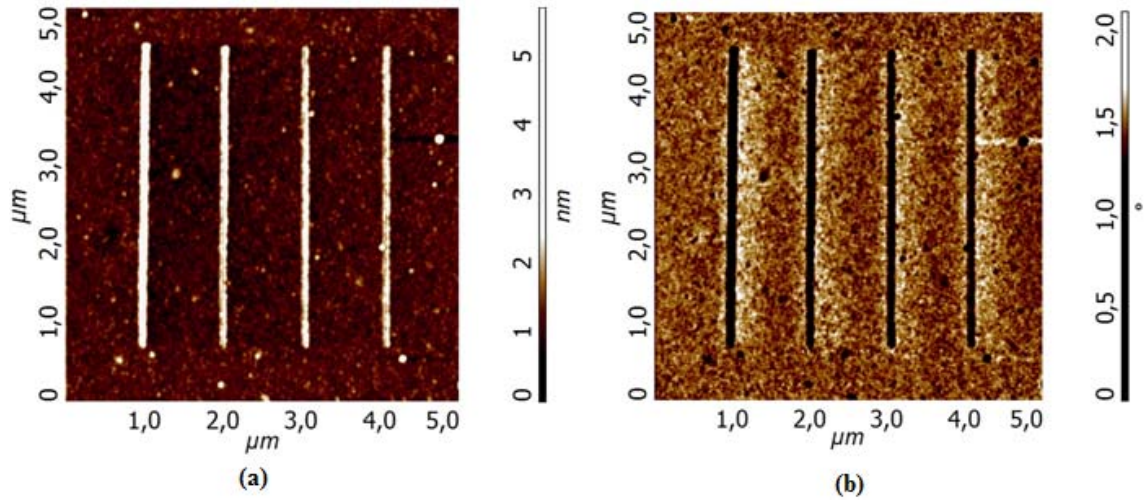

Figure 4.36. 2D AFM topography and EFM images of ZrO_x line structures.

2D AFM topography and EFM images of ZrO_x lines can be seen in Figure 4.36.a and 4.36.b. To prove that an electrochemical surface modification has been achieved, EFM image of the modified surface was obtained using second pass technique with a DC bias voltage of 3V and at a constant height of 10nm. In Figure 4.33.b, darker regions correspond to more electrically resistive regions while brighter regions correspond to more conductive regions. Figures 4.33.a and 4.33.b indicates that electrochemical surface modification has been achieved for the Zr surface.

4.4. Comparison of Oxidation Results for Ta, Hf and Zr

In order to compare the results for Ta, Hf and Zr; graphs of oxide height, line-width and aspect ratio versus bias voltage were drawn on same axis. All data used for comparison were obtained at ambient conditions. As can be seen from the Figure 4.37,

maximum oxide height was obtained for Ta at each bias voltage level. This result may be attributed to the significant difference between molecular volume of tantalum and tantalum oxide in comparison with hafnium and zirconium (see Table 4.3). In contrast to Ta, minimum oxide heights were found for Hf at each bias voltage level.

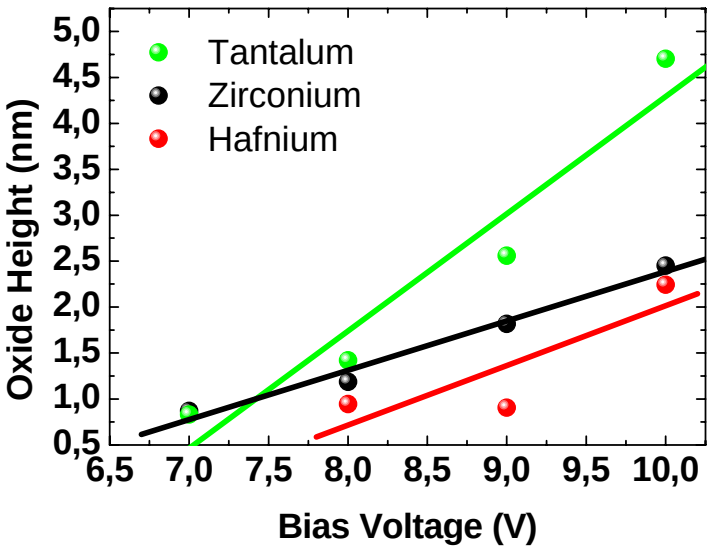

Figure 4.37. Oxide height versus applied bias voltage for TaO_x, HfO_x and ZrO_x at ambient conditions (T= ~24^{0}C, Rh= ~45%).

Figure 4.38 shows the line-width of oxide structures for Ta, Hf and Zr for different voltages. It is obvious that narrow structures are desirable for further resolution. Therefore, width of oxide lines is an important signal to decide whether the material that is used in our study is convenient for this oxidation method. Figure 4.38 indicates that HfO_x has maximum line-width for all applied voltages while Zr has minimum line-width. However, in order to determine the most convenient material for SPM oxidation method among the materials under the test we should take into accounts both height and line-width. In the most application of SPM oxidation method, it is required to keep height maximum while line-width minimum.

To make our results more clear we showed the graphs of aspect ratio of oxide lines for each material at different bias voltages in Figure 4.39. Aspect ratio means oxide height/ line-width (see Figure 4.40) and higher aspect ratio is desirable.

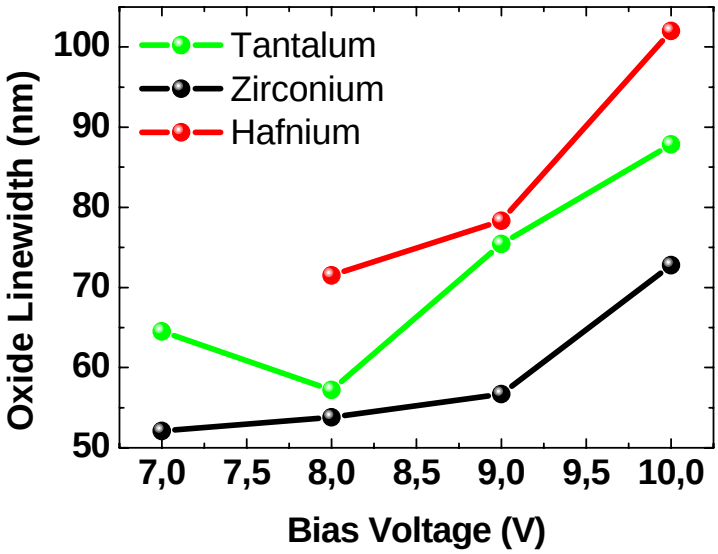

Figure 4.38. Oxide line-width versus applied bias voltage for TaO_x, HfO_x and ZrO_x at ambient conditions (T= ~24^{0}C, Rh= ~45%).

It is obvious from Figure 4.39 that tantalum seems the most convenient material for applications of SPM oxidation method among the tested materials.

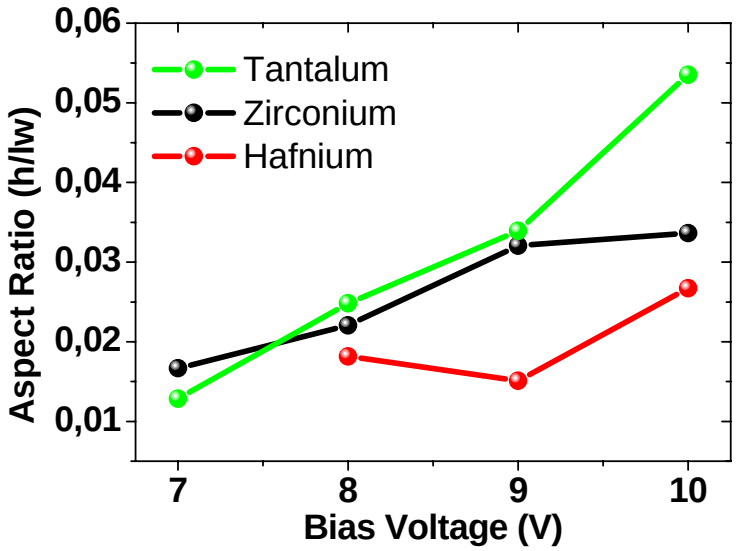

Figure 4.39. Aspect ratio of oxide lines for each material at different bias voltages at ambient conditions (T= ~24^{0}C, Rh= ~45%).

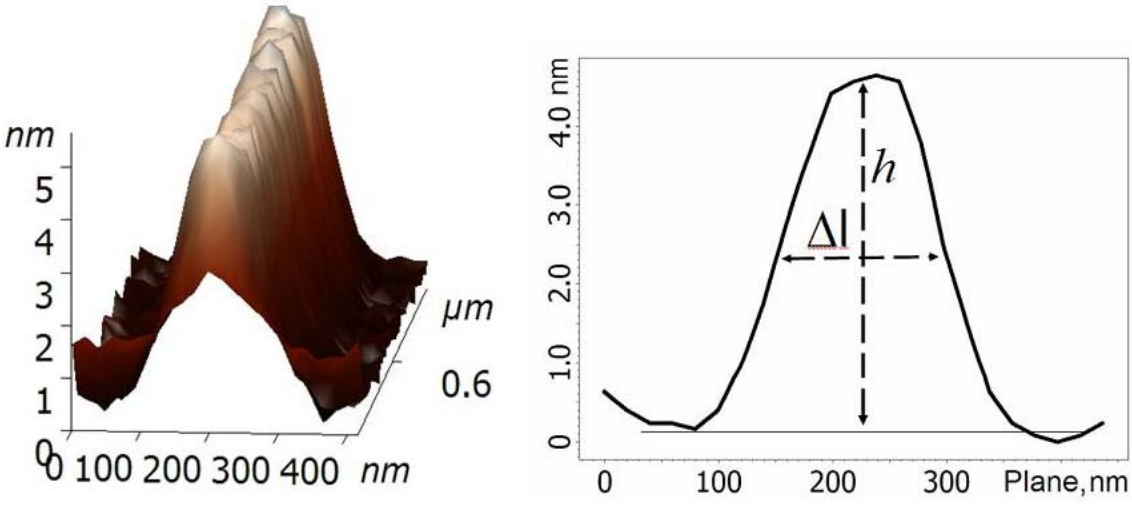

Figure 4.40. The oxide height and the full width at half maximum (FWHM) of the oxide line protrusions (Source: Okur, et al. 2008).

4.5. Results of Ta/TaO$_x$/Ta Structures

In this part, we used AFM oxidation method to produce Ta/TaOx/Ta electrical barrier. To create this structure, firstly ~8-9nm Ta is sputtered onto ~360nm thick thermally grown SiOx layer on a p-type Si substrate. The ~6μm wide wires were formed by optical lithography as mentioned chapter 3 (see Figure 4.39). All modifications and measurements were performed at ambient conditions. Figures 4.41.a and 4.41.b show 3D surface topography and height profile of tantalum stripe, respectively.

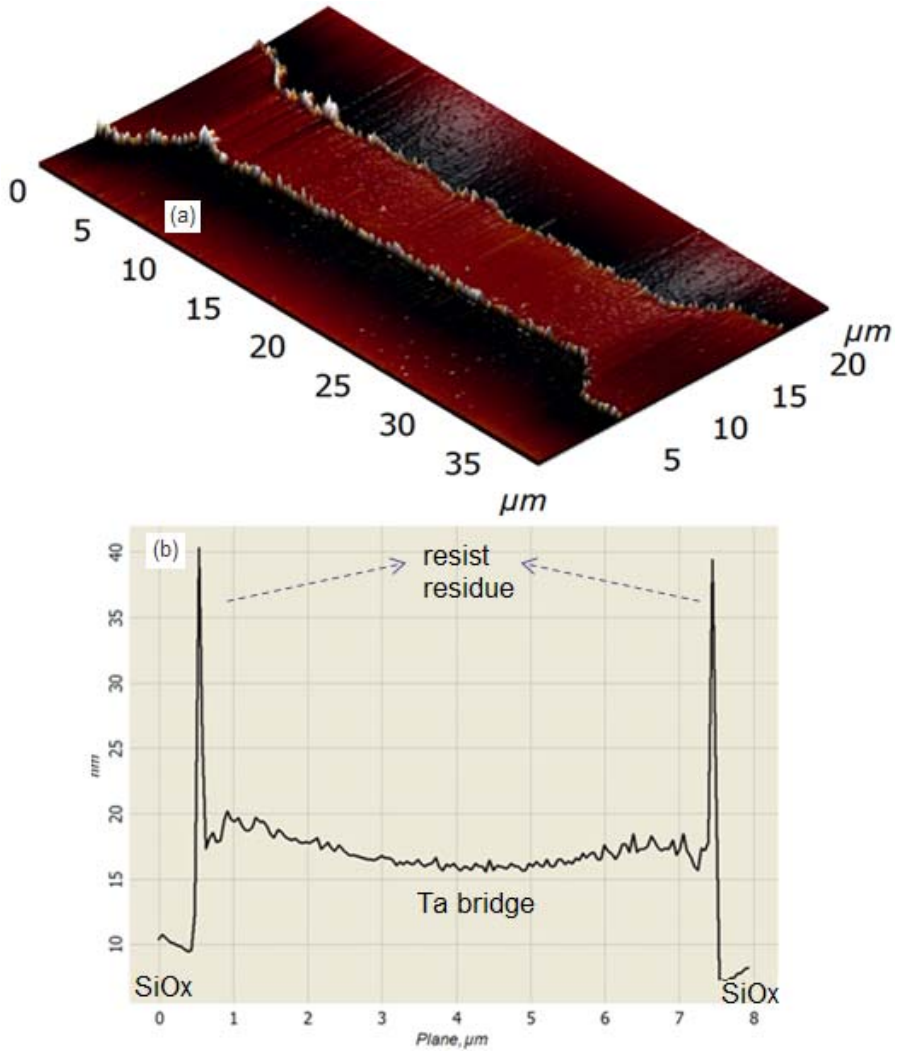

Figure 4.41. (a) 3D surface topography and (b) height profile of tantalum stripe.

During the lift-off process we have encountered a problem with resist. In figure 4.39, higher and narrow stripes can be seen edge of the tantalum stripe. In the literature, same problem reported by Vullers (Vullers 2000) (see Figure 4.42). According to this work, scanning auger spectroscopy measurements indicated that these stripes contain a large amount carbon suggesting that the stripes are residues of the resist layer. To overcome this problem they first removed the residues locally by applying a larger force during contact mode imaging, before performing the oxidation of Ti films. We didn't employ any treatment to remove these residues because they don't affect oxidation unless they placed on the Ta film. However, it seems that this problem should be solved for further applications including more processes.

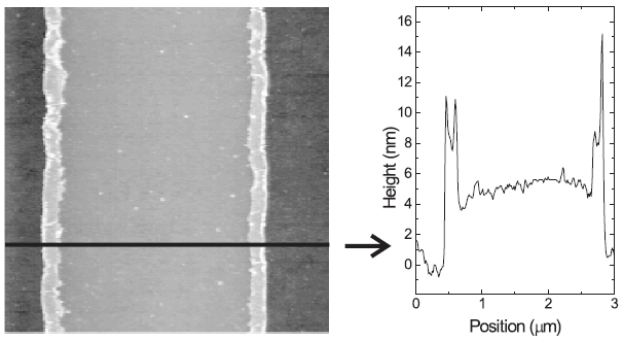

Figure 4.42. An AFM picture of a Ti line. On both sides of the line resist residue is visible. A line scan on the right shows the height of this residue (Source: Vullers 2000).

Barrier was formed by repeatedly scanning across the metallic strip. As mentioned experimental procedure, resistance was monitored during scan with four point measurement by using Keithley 2420 meter-source and LabView^{TM} software. Current was kept constant at 1μA, and voltage was read as order of mV.

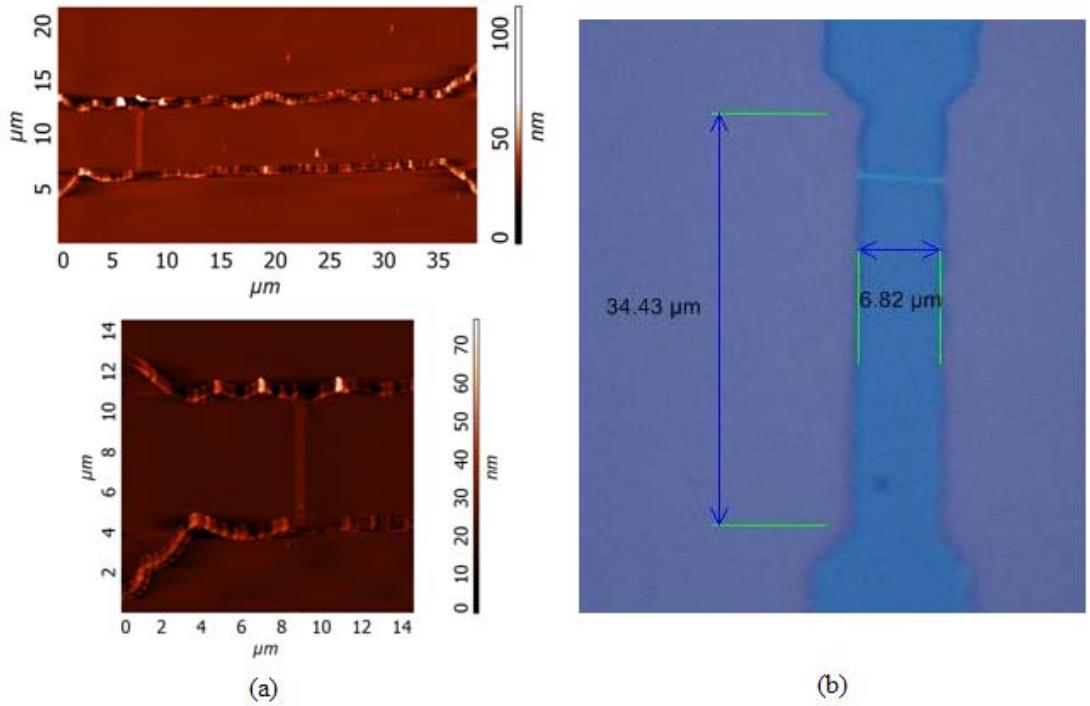

Figure 4.43. (a) 2D AFM image and (b) optical image of lithographically defined Ta line and TaO_x barrier.

Figure 4.43 shows 2D AFM images and optical image of lithographically defined Ta line and TaO_x barrier while Figure 4.44 shows 2D and 3D AFM images and height profile of TaO_x barrier created on Ta stripe.

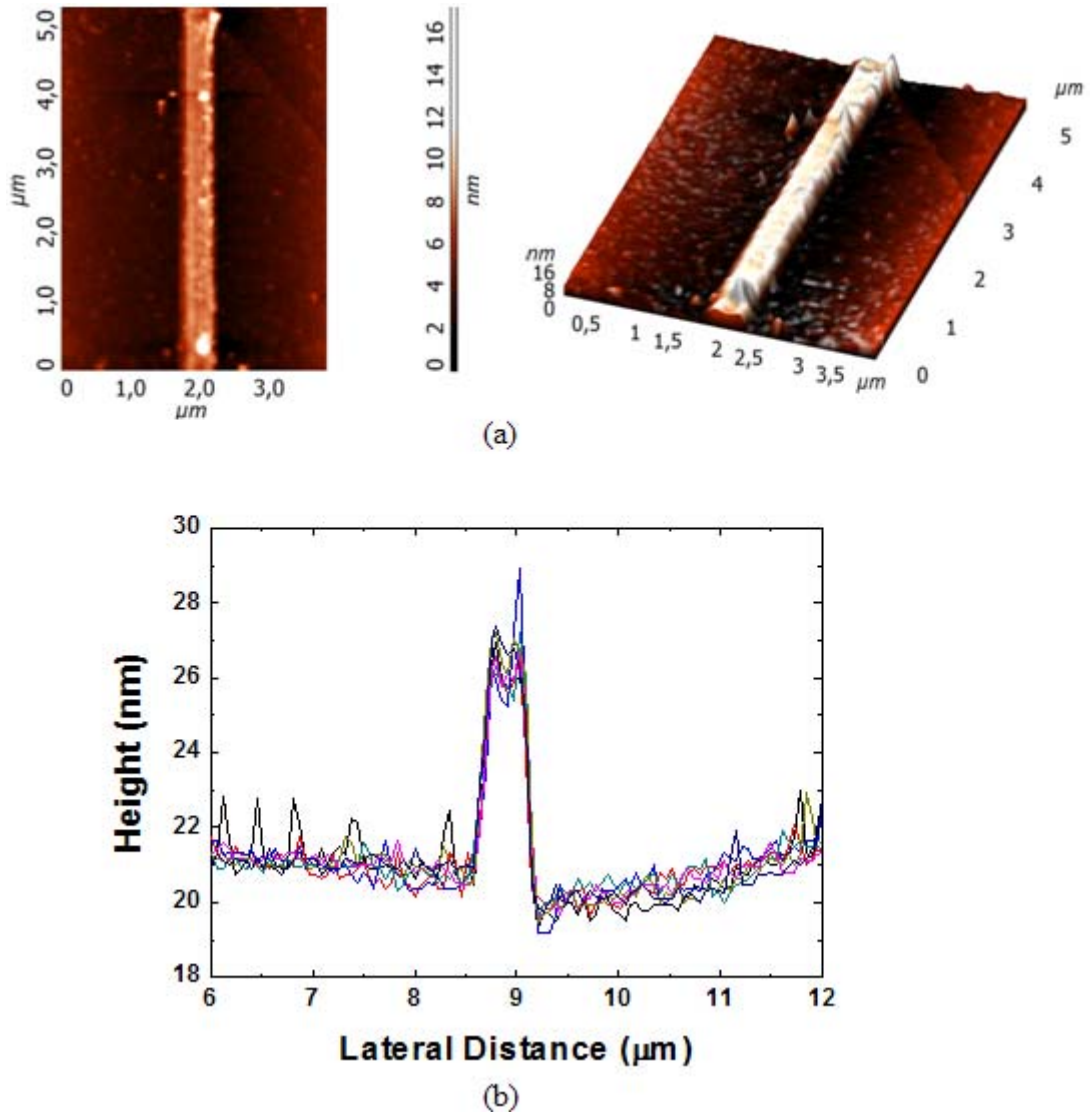

Figure 4.44. (a) 2D and 3D AFM images, and (b) height profile of TaO_x barrier created on Ta stripe.

Figure 4.45 shows the variation in resistance during the running scan. Effect of each scan can be seen from plot. The value of resistance starts from ~34kΩ and increases gradually with each scan to the ~370kΩ. When the increase of resistance with scan was stop, we run out the oxidation process because this means that further oxidation did not occur. In other words, the oxide reached to the maximum deepness.

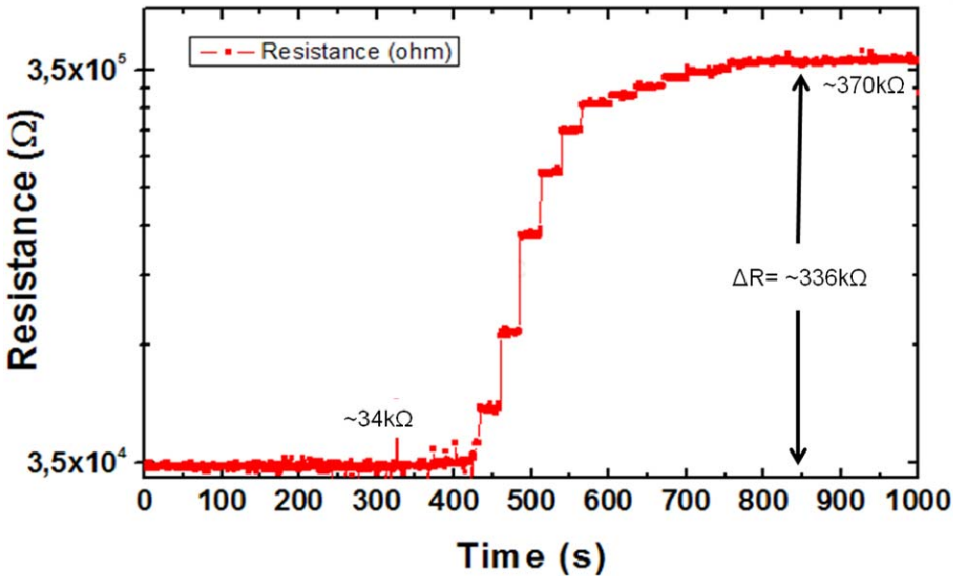

Figure 4.45. Variation in resistance of Ta stripe during the running scan.

After the oxidation, height of oxide line measured as 7,5nm. (see Figure 4.44). According to experimental result performed by Keyser oxide penetration dept is higher than the protrusion height (Keyser 2002). In this work, GaAs/AlGaAs-heterostructure was oxidized with AFM-based nanolithography (see Fig 4.46). This means that for our work TaO_x was created through the all film in z direction because the height of tantalum stripes is 8,5nm and protrusion height is 7,5nm.

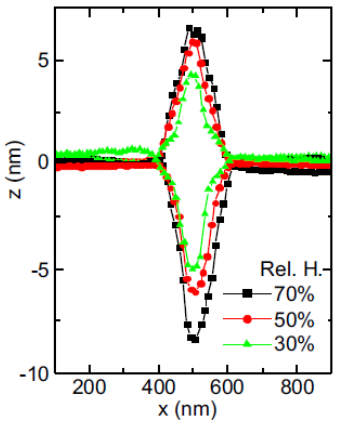

Figure 4.46. Cross section of the height/depth of an oxide line as a function of the position on the sample before/after a HCl etch (Source: Keyser 2002).

The current-voltage (I-V) characteristic of the device was investigated in order to test the barrier formation (Figure 4.47). Before the oxidation, 8,5nm thick metallic stripe showed linear I-V characteristic. After the oxidation, a change in resistance ΔR= ~336kΩ was observed (Figure 4.45) and I-V characteristic become non-linear indicating barrier formation.

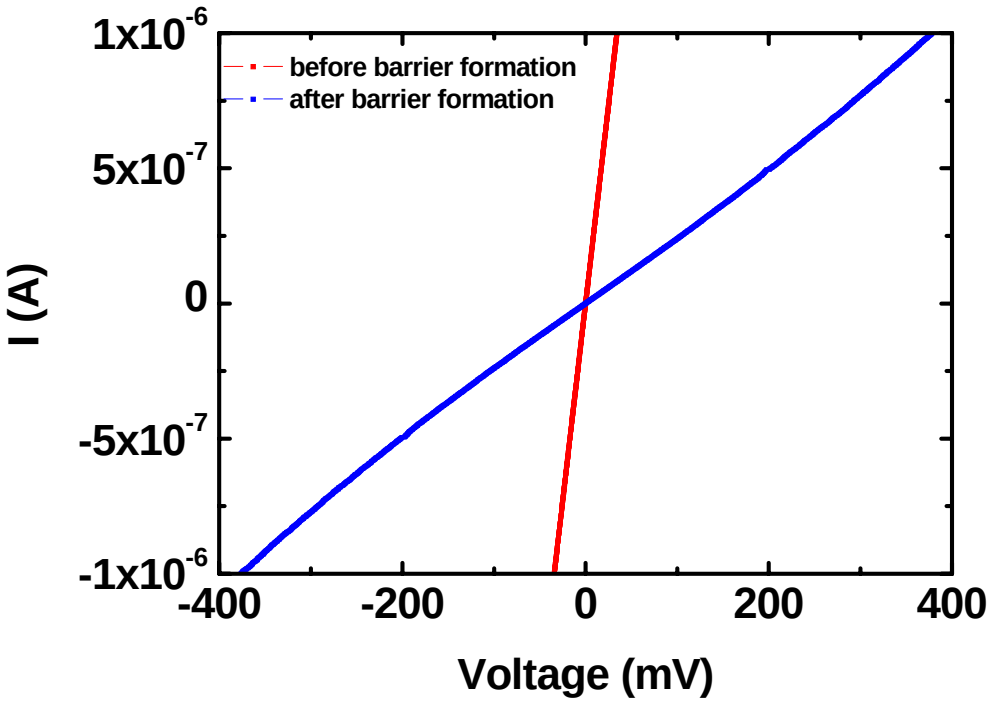

Figure 4.47. The current-voltage (I-V) characteristic of the Ta stripe before and after the barrier formation.

CHAPTER 5

CONCLUSION

This thesis focused on the possibility to pattern Ta, Hf and Zr films with sub-micrometer resolution using AFM induced local oxidation technique and investigate the oxidation kinetics of created oxides. In Chapter 1, the existing optical lithography has been briefly discussed. Alternative lithographic techniques, such as, e-beam lithography, x-ray lithography, ion beam lithography and lithography with scanning probe microscopy (SPM) have been also mentioned. Several SPM based lithographic techniques were presented. One of the most promising techniques is the local oxidation. It has a lot of advantages such as high resolution, alignment accuracy, high reliability, absence of radiation damage and low cost. However, it has also a disadvantage of low throughput. This may be increased by using an array of cantilevers.

Chapter 2 starts with the explanation of the basic principle of atomic force microscopy. The theory of the metal oxidation was also given in this chapter. Finally, oxidation of metallic thin films via an AFM tip was explained. This part started with the similarity between conventional electrolytic system and AFM oxidation system. Effective parameters in AFM oxidation process were explained with their roles in this process.

Chapter 3 consist of three subtitles; sample preparation, characterization and fabrication of Ta electrodes and $Ta/TaO_x/Ta$ structures. In the sample preparation part, the fabrication instruments were introduced and operation parameters for our work were given. Especially, the AFM was taken up more space because of its role in this work. In characterization part, technical properties of the conductive AFM tip was given with its SEM images obtained in Material Research Center (MAM) at İYTE. Electrical characterization methods in AFM operation, which are I-V, EFM, SRM, were explained in details. Optical lithography method for fabrication of Ta electrodes was explained with all steps and details. Mask shapes and instruments employed in lithography were

also presented. In the part of junction formation of $Ta/TaO_x/Ta$ via AFM, schematic of experiment setup was introduced. Finally, modified sample holder, source-meter instrument, entailment of simultaneous resistivity measurement during the experiment and user interface of software took part in this chapter.

In chapter 4 the results of experiments were given with detailed discussion. Firstly, structural characterization results obtained with x-ray diffraction analysis, scanning electron microscopy and atomic force microscopy were presented. Results showed that samples (tantalum, hafnium and zirconium) with thicknesses of 20nm, 65nm and 120nm has the roughness of 0,141nm (for Ta), 0,145nm (for Hf) and 0.166nm (for Zr). The roughness value of thermally oxidized SiO_x was also found as 0,133nm.

In order to understand the oxidation process and investigate the effect of applied bias voltage, oxidation time and relative humidity on created oxide features, experiments were performed under the controllable environment.

At the beginning, role of the bias voltage applied between conductive AFM tip and metallic surface was discussed. Oxide lines created applying different voltages ranging between 1V and 10V showed uniform features and a distinct dependence on the applied voltage. By keeping the oxidation time constant (210ms) for different values of relative humidity, a linear increase for oxide height with respect to applied voltage was observed as indicated in the literature by different workers. Width of oxide lines also increased with increasing bias voltage. These results were attributed to that higher bias voltages produce more ions and kinetic energy of these ions is higher than that of ions produced under a lower electric field. This means that more ions reach the oxide/metal interface under higher bias voltage. In this way, the oxidized region in the film increases with increasing bias voltage; therefore, a higher and wider protrusion from the surface is observed.

To understand the influence of the relative humidity on oxide height and width, oxidation experiments were performed at different values of relative humidity between 20%-85%. It is found that both height and line-width of the resulting oxides depend on the amount of relative humidity and oxidation has different threshold voltages at different values of relative humidity. These results were attributed to the number of water molecules between tip and sample surface at different values of relative humidity.

As a third parameter, oxidation time was studied. Other effective parameters were kept constant at a certain values and oxidation time was changed from 2ms to 210ms. It was found that the oxidation process is faster at the beginning, and then the oxide height reaches a maximum around a certain value (which is 5,23-2,30-2,16nm for TaO_x, HfO_x and ZrO_x, respectively). This results attributed to the accumulation of dielectric material under the tip and ionic space charges trapped near the substrate/oxide interface.

I-V measurements, spreading resistance measurements (SRM) and electric force microscopy (EFM) methods were performed for oxide structures. For electrical characterization of tip induced oxide structures, rectangle oxide layers were formed on the metallic films. Two terminal electrical measurements were done in contact mode allowing the AFM tip to touch the oxide layer or metal surface. I-V curves were taken with same DLC coated conductive AFM tip. Resistances obtained from I-V curves were found as ~3,0x$10^{12}\Omega$, ~8,0x$10^{12}\Omega$ and ~2,9x$10^{12}\Omega$ for TaO_x, HfO_x and ZrO_x, respectively. These results were compared with literature. Spreading resistance measurement gave the current difference as the contrast of SR image indicating the resistance difference between metal and metal-oxide surfaces. Electric force microscopy also gave qualitative results proved that an electrochemical surface modification had been achieved by oxidizing locally defined regions on the metallic surfaces.

In the part of comparison of oxidation results for Ta, Hf and Zr, we compared the height, line-width and aspect ratio of metal-oxide lines. According to this comparison, it seems that tantalum is the most convenient material for the most applications of SPM oxidation method among the tested materials because of oxide form with higher aspect ratio.

In the part of results of Ta/TaO_x/Ta structures, AFM oxidation method was used to produce Ta/TaO_x/Ta electrical barrier. The ~6μm wide and ~8-9nm height Ta stripe was formed by optical lithography. TaO_x barrier with ~7,5nm height was formed by repeatedly scanning across the Ta strip and simultaneously measuring the resistance of the stripe. The resistance of the Ta stripe started with ~34kΩ and increased to ~370kΩ at the end of the process. In addition to the resistance measurement, I-V characteristics of the Ta/TaO_x/Ta structure were investigated in order to test the barrier formation. Before the oxidation, metallic stripe showed a linear I-V characteristic while after the oxidation, I-V characteristic become non-linear indicating the barrier formation.

To summarize, we have been able to pattern Ta, Hf and Zr films at the nanometer scale using AFM oxidation method. Investigating the effective parameters we showed the roles of applied bias voltage, oxidation time and relative humidity on oxidation mechanism. It was shown that Ta is the most promising material to obtain higher aspect ratio metal oxide structures among the tested materials in this study, and it was tried to fabricate Metal/Oxide/Metal junction with AFM oxidation.

Scanning probe lithography seems a promising technique to create nano and submicron structures with its advantages mentioned at the beginning of the thesis. However, there is still a disadvantage of this technique; low throughput. In other words, this technique is not convenient for mass production with recent usage. This problem may be solved by using array of tips with multiply sensors.

Although main aim of this study is to investigate the oxidation kinetics of these three materials, some more investigations can be carried out as a future work. For example, oxide lines with higher aspect ratio can be produced by using narrower tips. Using different voltage shapes with different frequencies instead of continuous pulses can be also studied to improve the oxide properties and resolution. Furthermore, applying constant current between tip and surface can be gave more desirable results on created oxide.

REFERENCES

Abadal, G., A. Boisen, Z. J. Davis, O. Hansen, and F. Grey. 1999. Combined Laser and Atomic Force Microscope Lithography on Aluminium: Mask Fabrication for Nanoelectromechanical Systems. *Applied Physics Letters* 74: 3206-3208.

Avouris, Ph., T. Hertel and R. Martel. 1997. Atomic force microscope tip-induced local oxidation of silicon: kinetics, mechanism, and nanofabrication. *Applied Physics Letters* 71: 285-287.

Avouris, Ph., R. Martel, T. Hertel, R. Sandstrom. 1998. AFM-tip-induced and current-induced local oxidation of silicon and metals. *Applied Physics A* 66: 659-667.

Avramescu, A., A. Ueta, K. Uesugi, and I. Suemune. 2000. Atomic Force Microscope Based Patterning of Carbonaceous Masks for Selective Area Growth on Semiconductor Surfaces. *Journal of Applied Physics* 88: 3158-3165.

Barash, J. S. 1998. *Van der Waals forces*, Moscow: Nauka.

Birger, I. A., Shorr B. F., Iosilevich G. B., eds. 1979. *Calculation on strength of details of machines*. Moscow: Machinostroenie.

Binnig, G. and H. Rohrer. 1982. Scanning tunneling microscopy. *Helvetica Physica Acta* 55: 726-735.

Binnig, G., Quate C. F., and Gerber Ch. 1986. Atomic force microscope. *Physics Review Letters* 56: 930-933.

Buyukkose, S., S. Okur and G. Aygun. 2009. Local oxidation nanolithography on Hf thin films using atomic force microscopy (AFM). *Journal of Physics D: Applied Physics* 42: 105302-105309.

Bouchiat, V., M. Faucher, C. Thirion., W. Wernsdorfer., T. Fournier, and B. Pannetier. 2001. Josephson junctions and superconducting quantum interference devices made by local oxidation of niobium ultrathin films. *Applied Physics Letters* 79: 123.

Cabrera, N. and N. F. Mott. 1949. Theory of the oxidation of metals. *Reports on Progress in Physics* 12: 163.

Calleja, M. and R. Garcia. 2000. Nanooxidation of Silicon Surfaces by Noncontact Atomic-Force Microscopy: Size Dependence on Voltage and Pulse Duration. *Applied Physics Letters* 76: 3427-3429.

Cassir, M., F. Goubin, C. Bernay, P. Vernoux, D. Lincot. 2002. Synthesis of ZrO_2 thin films by atomic layer deposition: growth kinetics, structural and electrical properties. *Applied Surface Science* 193: 120-128.

Cooper, E. B., S. R. Manalis, H. Fang, H. Dai, K. Matsumoto, S. C. Minne, T. Hunt, and C. F. Quate. 1999. Terabit -per-Square-Inch Data Storage with the Atomic Force Microscope. *Applied Physics Letters* 75: 3566-3568.

Chien, F. S. -S., J. -W. Chang, S. -W. Lin, Y. -C. Chou, T. T. Chen, S. Gwo, T. -S. Chao , and W. -F. Hsieh. 2000. Nanometer-Scale Conversion of Si_3N_4 to SiO_x. *Applied Physics Letters* 76: 360-362.

Campbell, P. M. and E. S. Snow. 1998. Proximal Probe-Based Fabrication of Nanometer Scale Devices. *Materials Science and Engineering B* 51: 173-177.

Campbell, P. M., E. S. Snow, and P. J. McMarr. 1995. Fabrication of Nanometer-Scale Side Gated Silicon Field-Effect Transistors with an Atomic Force Microscope. *Applied Physics Letters* 66: 1388-1390.

Chen, W. and H. Ahmed. 1993. Fabrication of sub-10nm structures by lift-off and by etching after electronbeam exposure of poly(methylmethacrylate) resist on solid substrates *The Journal of Vacuum Science and Technology B: Microelectronics and Nanometer Structures* 11: 2519-2523.

Cumming, D. R. S., S. Thoms, S.P. Beaumont, J. M. R. Weavwer. 1996. Fabrication of 3 nm wires using 100 keV electron beam lithography and poly(methyl methacrylate) resist. *Applied Physics Letters* 68: 322

Dagata, J. A., F. Perez-Murano, G. Abadal, K. Morimoto, T. Inoue, J. Itoh and H. Yokoyama. 2000. Predictive model for scanned probe oxidation kinetics. *Applied Physics Letters* 76: 2710.

Dagata, J. A., J. Schneir, H. H. Haray, C. J. Evans, M. T. Postek, and J. Bennett. 1990. Modification of hydrogen-passivated silicon by a scanning tunneling microscope operating in air. *Applied Physics Letters* 56: 2001.

Dagata, J. A., W. Tseng, J. Bennett, J. Schneir, and H. H. Harary. 1991. Nanolithography on III-V Semiconductor Surfaces using a Scanning Tunneling Microscope Operating in Air. *Journal of Applied Physics* 70: 3661-3665.

Dai, H., N. Franklin, and J. Han. 1998. Exploiting the Properties of Carbon Nanotubes for Nanolithography. *Applied Physics Letters* 73: 1508-1510.

Fang, T. –H., T. H. Wang, K. –T. Wu. 2008. Local oxidation of titanium films by non-contact atomic force microscopy. *Microelectronic Engineering* 85: 1616-1623.

Fang, T. –H. and W. –J. Chang. 2004. Nanolithography and nanoindentation of tantalum oxide nanowires and nanodots using scanning probe microscopy. *Physica B* 352: 190-199.

Farkas, N., J. C. Tokash, G. Zhang, E. A. Evans, R. D. Ramsier and J. A. Dagata. 2004. Local oxidation of metal and metal nitride films. *The Journal of Vacuum Science and Technology A* 22: 1879-1884

Fontaine, P. A., E. Dubois, and D. Stiévenard. 1998. Characterization of Scanning Tunneling Microscopy and Atomic Force Microscopy-Based Techniques for Nanolithography on Hydrogen-Passivated Silicon. *Journal of Applied Physics* 84: 1776-1781.

Garcia, R., M. Calleja, and H. Rohrer. 1999. Patterning of Silicon Surfaces with Noncontact Atomic Force Microscopy: Field –Induced Formation of Nanometer-Size Water Bridges. *Journal of Applied Physics* 86: 1898-1903.

Gotoh, Y., K. Matsumoto, T. Maeda, E. B. Cooper, S. R. Manalis, H. Fang, S. C. Minne, T. Hunt, H. Dai, J. S. Harris, and C. F. Quate. 2000. Experimental and Theoretical Results of Room-Temperature Single-Electron Transistor Formed by the Atomic Force Microscope Nano-Oxidation Process. *The Journal of Vacuum Science and Technology A* 18: 1321-1325.

Held, R., T. Heinzel, P. Studerus, K. Ensslin, and M. Holland. 1997. Semiconductor Quantum Point Contact Fabricated by Lithography with an Atomic Force Microscope. *Applied Physics Letters* 71: 2689-2691.

Huh, C., S. -J. Park. 2000. Atomic force microscope tip-induced anodization of titanium film for nanofabrication of oxide patterns. *The Journal of Vacuum Science and Technology B* 18: 55-59.

Hu, S., A. Hamidi, S. Altmayer, T. Koster, B. Spangenberg, and H. Kurz. 1998. Fabrication of silicon and metal nanowires and dots using mechanical atomic force lithography. *The Journal of Vacuum Science and Technology B* 16: 2822-2824.

Huber, F. 1971. Properties of hafnium dioxide thin-film capacitors. *IEEE Transactions on Parts, Hybrids, and Packaging* 7: 141-147.

Hu, X., T. Guo, X. Fu, X. Hu. 2003. Nanoscale oxide structures induced by dynamic electric field on Si with AFM. *Applied Surface Science* 217: 34-38.

Hsu, H. -F., C. -W. Lee. 2008. Effects of humidity on nano-oxidation of silicon nitride thin film. *Ultramicroscopy* 108: 1076-1080.

Ishibashi, M., S. Heike, H. Kajiyama, Y. Wada, and T. Hashizume. 1998. Characteristics of scanning-probe lithography with a current-controlled exposure system. *Applied Physics Letters* 72: 1581.

Keyser, U. F. 2002. Nanolithography with an atomic force microscope: quantum point contacts, quantum dots, and quantum rings. *PhD diss.*, Hannover University.

Kramer, N., H. Birk, J. Jorritsma, and C. Schönenberger. 1995. Fabrication of Metallic Nanowires with a Scanning Tunneling Microscope. *Applied Physics Letters* 66: 1325-1327.

Kim, Y. –h., J. Zhao, and K. Uosaki. 2003. Formation and electric property measurement of nanosized patterns of tantalum oxide by current sensing atomic force microscope. *Journal of Applied Physics* 94: 7733-7738.

Kittel, C. 1976. *Introduction to Solid State Physics*. California: Wiley.

Legrand, B. and D. Stiévenard 1999. Nanooxidation of Silicon with an Atomic Force Microscope: A Pulsed Voltage Technique. *Applied Physics Letters* 74: 4049-4051.

Lemeshko, S., S. Gavrilov, V. Shevyakov, V. Roschin and R. Solomatenko. 2001. Investigation of tip induced ultrathin Ti film oxidation kinetics. *Nanotechnology* 12: 273-276.

Lee, S. and H. Lee. 2006. Nanostructures Fabrication on Ta Thin Film Using Atomic Force Microscope Lithography. *Molecular Crystals and Liquid Crystals* 445: 115-118.

Levinson, H. J. 2005. *Principles of Lithography.* Bellingham, WA: SPIE

Lee, Y., R. A. Gough, K. N. Leung, J. Vujic, M. D. Williams, N. Zahir, W. Fallman, M. Tockler, and W. Bruenger. 1998. Plasma source for ion and electron beam lithography. *The Journal of Vacuum Science and Technology B* 16: 3367-3369.

Lu, Y. S., H. I. Wu, S. Y. Wu and Y. R. Ma. 2007. Tip-induced large-area oxide bumps and composition stoichiometry test via atomic force microscopy. *Surface Science* 601: 3788-791.

Lo, R. -L., W.-C. Lee and J. Kwo. 2006. Atomic Force Microscopy Nanolithography on Hafnium Oxide Thin Film Grown on Si(100). *Japanese Journal of Physics* 45: 2067-2069.

Ma, Y. R., C. Yu, Y. D. Yao, Y. Liou and S. F. Lee. 2001. Tip-induced local anodic oxidation on the native SiO_2 layer of Si (111) using an atomic force microscope. *Physical Review B* 64: 195324.

Majumdar, A., P. I. Oden, J. P. Carrejo, L. A. Nagahara, J. J. Graham, and J. Alexander. 1992. Nanometer-scale lithography using the atomic force microscope. *Applied Physics Letters* 61: 2293.

Manchanda, L., M. D. Morris, M. L. Green, R. W. van Dover, F. Klemens, T. W.Sorsch, P. J. Silverman, G. Wilk, B. Busch and S.Aravamudhan. 2001. Multi-component high-K gate dielectrics for the silicon industry. *Microelectronic Engineering* 59: 351-359.

Matsumoto, K., M. Ishii, and K. Segawa. 1996. Application of Scanning Tunneling Microscopy Nanofabrication Process to Single Electron Transistor. *The Journal of Vacuum Science and Technology B* 14: 1331-1335.

Matsumoto, K. 1998. Application of scanning tunneling/atomic force microscope nanooxidation process to room temperature operated single electron transistor and other devices. *Scanning Microscopy* 12: 61-69.

McCord, M. A. 1987. Lithography with the scanning tunneling microscope. *PhD diss.*, Standford University.

Minne, S. C., P. Flueckiger, H. T. Soh, and C. F. Quate. 1995. Atomic Force Microscope Lithography Using Amorphous Silicon as a Resist and Advances in Parallel Operation. *The Journal of Vacuum Science and Technology B* 13: 1380-1385.

Minne, S. C., H. T. Soh, P. Flueckiger, and C. F. Quate 1995. Fabrication of 0.1 mm Metal Oxide Semiconductor Field-Effect Transistors with the Atomic Force Microscope. *Applied Physics Letters* 66: 703-705.

Mironov, V. L. 2004. Fundamentals of Scanning Probe Microscopy. Nizhniy Novgorod: NT-MDT.

Moon, B. K., C. Isobe, and J. Aoyama. 1999. Insulating properties of tantalum pentoxide capacitor films obtained by annealing in dry ozone. *Journal of Applied Physics* 85: 1731.

Nishimura, S., Y. Takemura and J. Shirakashi. 2007. SPM local oxidation nanolithography with active control of cantilever dynamics. *Journal of Physics: Conference Series* 61: 1066-1070.

Okada, Y., S. Amano, M. Kawabe, J. S and Harris. 1998. Basic Mechanisms of an Atomic Force Microscope Tip -Induced Nano-oxidation process of GaAs. *Journal of Applied Physics* 83: 7998-8001.

Okur, S., S. Büyükköse, and S. Tari 2008. Scanning Probe Oxidation Lithography on Ta Thin Films. *Journal of Nanoscience and Nanotechnology* 8: 5640–5645.

Park, S. W., H. T. Soh, C. F. Quate, and S. Park–I. 1995. Nanometer scale lithography at high scanning speeds with the atomic force microscope using spin on glass. *Applied Physics Letters* 67: 2415.

Pena, D. J., M. P. Raphael, J. M. Byers 2003. "Dip-Pen" Nanolithography in Registry with Photolithography for Biosensor Development. *Langmuir* 19: 9028-9032.

Pérez-Murano, F., K. Birkelund, K. Morimoto, and J.A. Dagata. 1999. Voltage Modulation Scanned Probe Oxidation. *Applied Physics Letters*75: 199-201.

Pilling, N. B. and R. E. Bedworth 1923. The Oxidation of Metals at high Temperature. *Journal Institute of Metals* 29: 529.

Piner R. D., J. Zhu, F. Xu, S. Hong, C. A. Mirkin. 1999. Dip-Pen Nanolithography. *Science* 283: 661-663.

Sayan S., E. Garfunkel and S. Suzer. 2002. Soft x-ray photoemission studies of the HfO2/SiO2/Si system. *Applied Physics Letters* 80: 2135.

Schwartz, P. V. 2002. Molecular Transport from an Atomic Force Microscope Tip: A Comparative Study of Dip-Pen Nanolithography. *Langmuir* 18: 4041-4046.

Shindo, H., M. Ohashi, K. Baba, and A Seo. 1996. AFM Observation of Monatomic Step Movements on NaCl(001) with the Help of Adsorbed Water. *Surface Science* 357- 358: 111-114.

Silverman, J. P. 1998. Challenges and progress in x-ray lithography. *The Journal of Vacuum Science and Technology B* 16: 3137-3141.

Snow, E. S. and P. M. Campbell. 1995. AFM Fabrication of Sub-10-Nanometer Metal Oxide Devices with in Situ Control of Electrical Properties. *Science* 270: 1639-1641.

Snow, E. S., D. Park, and P. M. Campbell. 1996. Single-Atom Point Contact Devices Fabricated with an Atomic Force Microscope. *Applied Physics Letters* 69: 269-71.

Song, H. J., M. J. Rack, K. Abugharbieh, S. Y. Lee, V. Khan, D. K. Ferry, and D. R. Allee. 1994. 25 nm Chromium Oxide Lines by Scanning Tunneling Lithography in Air. *The Journal of Vacuum Science and Technology B* 12: 3720-3724.

Sugimura, H., T. Uchida, N. Kitamura, and H. Masuhara 1994. Scanning Tunneling Microscope Tip -Induced Anodization of Titanium: Characterization of the Modified Surface and Application to the Metal Resist Process for Nanolithography. *The Journal of Vacuum Science and Technology B* 12: 2884-2888.

Suh, Y. 2003. Fabrication and evaluation of devices containing high K gate dielectrics and metal gate electrodes for the 70 and 50 nm technology nodes of ITRS. *PhD diss.*, North Caroline State University.

Tamman, G. 1920. Uber Anlauffarben von Metallen. *Zeitschrift für Anorganische Chemie* 111: 78-89.

Tello, M. and R. Garcia. 2001. Nano-Oxidation of Silicon Surfaces: Comparison of Noncontact and Contact Atomic –Force Microscopy Methods. *Applied Physics Letters* 79: 424-426.

Teuschler, T., K. Mahr, S. Miyazaki, M. Hundhausen and L. Ley. 1995. Nanometer-scale field induced oxidation of Si (111): H by a conducting-probe scanning force microscope: doping dependence and kinetics. *Applied Physics Letters* 67: 3144.

Thundat, T., L. A. Nagahara, P. I. Oden, S. M. Lindsay, M. A. George, W. S. Glaunsinger. 1990. Modification of tantalum surfaces by scanning tunneling microscopy in an electrochemical cell. *The Journal of Vacuum Science and Technology A* 8: 3537-3541.

Tseng, A. A., A. Notargiacomo and T. P. Chen. 2005. Nanofabrication by scanning probe microscope lithography: a review. *The Journal of Vacuum Science and Technology B* 23: 877-894.

Unal, K., B.-O. Aronsson, Y. Mugnier and P. Descouts. 2002. Nano oxidation of titanium films with large atomically flat surfaces by means of voltage-modulated scanning probe microscopy. *Surface and Interface Analysis.* 34: 490–493.

University of Illinois at Urbana-Champaign-ECE 2009. http://fabweb.ece.uiuc.edu/gt/gt/gt4.aspx (accessed May 21, 2009).

Van Loenen, E. J., D. Dijkkamp, A. J. Hoeven, J. M. Lenssinck, and J. Dieleman. 1989. Direct writing in Si with a scanning tunneling microscope. *Applied Physics Letters* 55: 1312.

Vettiger, P., G. Cross, M. Despont, U. Drechsler, U. Durig, B. Gotsmann, W. Haberle, M. A. Lantz, H. E. Rothuizen, R. Stutz and G. K. Binnig. 2002. The "millipede"-nanotechnology entering data storage. *IEEE Transactions on Nanotechnology* 1: 39-55.

Vullers, R. J. M., M. Ahlskog, M. Cannaerts, and C. Van Haesendonck. 1999. Field induced local oxidation of Ti and Ti/Au structures by an atomic force microscope with diamond coated tips. *The Journal of Vacuum Science and Technology B* 17: 2417-2422.

Wagner, C. 1933. Theory of the Oxidation Process. *Zeitschrift für Physikalische Chemie B* 21: 25

Wilder, K., C. F. Quate, D. Adderton, R. Bernstein, and V. Elings. 1998. Noncontact nanolithography using the atomic force microscope. *Applied Physics Letters* 73: 2527.